HIGH-RESOLUTION CHARACTERIZATION OF FILOPODIAL INTERACTIONS GUIDING NEUROMUSCULAR CIRCUIT DEVELOPMENT IN DROSOPHILA

by

MELISSA ANA INAL

(Under the Direction of Daichi Kamiyama)

ABSTRACT

For functional brain development, neural circuits must be organized precisely. Any aberrations throughout the development of connectivity of the neural circuit can lead to neurodevelopmental defects. Therefore, understanding the early mechanisms underlying the organization of a functioning neural circuit is essential. Precision of synaptogenesis depends on target recognition and synaptic assembly mediated by cellular contacts between the partner cells. For studying how early recognition events contribute to functional neural circuit development, we use the embryonic *Drosophila* neuromuscular junction (NMJ) as a model system. The NMJ in *Drosophila* is a simple, stereotypically organized neural circuit made up of 36 motor neurons and 30 muscles. During NMJ synaptogenesis, both the presynaptic motor neurons and the postsynaptic muscles extend long and thin actin-containing membrane processes, called filopodia, that contribute to contact-based communication. While roles of filopodia on the presynaptic terminal are widely studied and relatively well understood, the functions of post-synaptic filopodia have been less studied. In this dissertation, first we report a retrograde lipophilic dye labeling method to labeling neurons using single or multi-color dyes allowing high resolution access to fine cellular processes like neurites, dendrites as well as filopodia. Second, we report a super-resolution microscopy method, stochastic optical reconstruction microscopy (STORM), to study molecular and morphological organization of *in vivo* and *in vitro* neurons. Third, we report on a set of orthogonal binary expression systems (Gal4/UAS and LexA/LexAop) that allow the study of single NMJs using live imaging and discuss other applications of these lines for studying muscle development and specification of targeting. Through live imaging studies, we uncover that membrane morphologies between muscles are different and discuss their implications in synaptic specificity. Fourth, we explore the characteristics and roles of muscle-derived filopodia in synaptic targeting, axon guidance, and synaptogenesis. Altogether, this thesis provides improved resolution to study cellular structures like filopodia at synapses and provides insights into contributions of filopodia activity to neural circuit development in living animals.

INDEX WORDS: filopodia, neuromuscular junction, axon guidance, synaptic targeting, dye labeling, super-resolution microscopy, STORM, Gal4/UAS, LexA/LexAop

HIGH-RESOLUTION CHARACTERIZATION OF FILOPODIAL INTERACTIONS GUIDING NEUROMUSCULAR CIRCUIT DEVELOPMENT IN DROSOPHILA

by

MELISSA ANA INAL

B.S., The University of Georgia, 2018

A Dissertation Submitted to the Graduate Faculty of The University of Georgia in Partial Fulfillment of the Requirements for the Degree

DOCTOR OF PHILOSOPHY

ATHENS, GEORGIA

2025

HIGH-RESOLUTION CHARACTERIZATION OF FILOPODIAL INTERACTIONS GUIDING NEUROMUSCULAR CIRCUIT DEVELOPMENT IN DROSOPHILA

by

MELISSA ANA INAL

Major Professor:	Daichi Kamiyama
Committee:	Peter A. Kner Karl Lechtreck Rachel Roberts-Galbraith

Electronic Version Approved:

Ron Walcott
Vice Provost for Graduate Education and Dean of the Graduate School
The University of Georgia
August 2025

DEDICATION

To my family.

ACKNOWLEDGEMENTS

I am grateful to my advisor, Daichi Kamiyama, for giving me the opportunity to become a scientist. Thank you for challenging me at every step of the scientific process, allowing me to challenge myself in turn—to consider biological events from different perspectives. I will miss our fun brainstorming sessions, where we drew from all parts of life—thinking about honeycombs and snowflakes. I am incredibly grateful to my committee members: Karl, Peter, and Rachel. Thank you for holding me to a high standard and pushing me to become a better scientist.

I would like to thank Rie and Miyuki for their enthusiasm and help in maintaining my flies and performing secondary immunostaining when I had to be in two places at once—you made it possible. I also want to thank Ryo, Kathy, and Riddhi. Our daily interactions in the lab—from brainstorming ideas to sharing our cultures—were some of the most enriching experiences I have had. Our delicious meals and hotpot parties let me rediscover the foods and friendships that made Athens feel like home. I am grateful to all of you for bringing color to my life here.

I am grateful to my dad, Ali, and my brother, Michael, for always supporting me and offering a hand whenever they could—whether grading exams or writing code to automate my image quantifications. Thank you to my grandmother for encouraging me to dissect and study brains—this is for you. I am grateful to my partner, Ryo, for his unwavering support every step of the way and always being there to lend an ear. To all of you—thank you for believing in me, lifting me up in countless ways, and helping me reach the finish line of this long and arduous journey.

TABLE OF CONTENTS

Page

LIST OF TABLES

LIST OF FIGURES

CHAPTER 1

INTRODUCTION AND LITERATURE REVIEW

1.1 THE IMPORTANCE OF NEURODEVELOPMENTAL STUDY

Understanding how the brain develops is one of the most fundamental goals of neuroscience. The human brain takes nearly 25 years to reach full structural and functional maturity (Arain et al., 2013), during which time it undergoes an extraordinary transformation—from a collection of progenitor cells into a complex network comprising roughly 100 billion neurons and an estimated 100 trillion synapses (Azevedo et al., 2009). These neural connections underlie every cognitive, sensory, and motor function, and their formation follows tightly regulated developmental programs that are highly conserved across species.

Even organisms with vastly smaller nervous systems display remarkable complexity. For instance, the mouse brain contains approximately one billion neurons and one trillion connections, while the fruit fly (*Drosophila melanogaster*) has around 140,000 neurons forming approximately 50 million synapses (Dorkenwald et al., 2024; Herculano-Houzel et al., 2006). Regardless of scale, the core principle remains the same: each neuron must establish specific, selective connections with appropriate partners in order to participate in functional neural circuits.

Disruptions to this precise wiring process can result in profound consequences. Aberrant connectivity during early development is a hallmark of many neurodevelopmental disorders (NDDs). For example, hyperconnectivity has been implicated in autism spectrum disorder (ASD) (Supekar et al., 2013), while reduced connectivity has been associated with attention-deficit/hyperactivity disorder (ADHD) and schizophrenia (Liao et al., 2023). These conditions remain difficult to diagnose and treat due to overlapping behavioral symptoms and poorly understood molecular underpinnings (Mullin et al., 2013). Thus, elucidating the mechanisms that guide neural connectivity during development is not only a scientific priority but also a clinical necessity.

A powerful approach to understanding how neural circuits are established is to directly observe the behavior of neurons during development. This practice dates back to Ramón y Cajal, who pioneered sparse neuronal labeling techniques (e.g., Golgi staining) to study developing brains and laid the conceptual groundwork for modern neuroanatomy (Hunter et al., 2025). Technological advances have since enabled high-resolution imaging of entire connectomes in smaller organisms, such as *Drosophila* (Dorkenwald et al., 2024; Winding et al., 2023). These efforts are now expanding to larger systems as well, such as the mouse visual cortex (The MICrONS Consortium et al., 2025).

While complete anatomical maps offer crucial reference points, they do not explain the dynamics of how synaptic connections arise during development. The next major challenge in neuroscience lies in deciphering the cellular and molecular mechanisms that give rise to these patterns of connectivity. Doing so will deepen our understanding of normal brain function and provide critical insight into the pathogenesis of developmental disorders.

1.2 TOOLS FOR STUDYING DROSOPHILA SYNAPTOGENESIS

Deciphering the molecular and cellular mechanisms of synaptogenesis requires precise visualization and manipulation of individual cells within developing circuits. *Drosophila melanogaster* offers a uniquely versatile genetic and optical toolkit for such studies, particularly at the neuromuscular junction (NMJ), where motor neurons form synapses with large, accessible muscle fibers. The simplicity and stereotypy of these connections, along with the depth of available tools, make the *Drosophila* NMJ a premier system for investigating synaptic development at single-cell resolution.

Early studies of neuronal connectivity built upon the work of Ramón y Cajal, who used sparse labeling techniques (such as Golgi staining) to reveal the structure of neurons in developing tissue (Hunter et al., 2025). In *Drosophila*, these foundational approaches have been extended using both direct and genetically encoded labeling strategies. One such direct approach involves the use of fluorescent dyes, like Lucifer Yellow and lipophilic tracers, to selectively label neurons or muscles. For example, Lucifer Yellow is often injected into motor neurons for anterograde labeling (Sink & Whitington, 1991), while retrograde labeling with lipophilic dyes is employed to reveal dendritic structures or postsynaptic architecture. Similarly, muscle fibers can be labeled directly due to their large size and accessible surface area (Johansen et al., 1989; Bate, 1990).

More refined genetic labeling systems have revolutionized cell-type-specific studies. The most widely used system is the Gal4/UAS binary expression system, adapted from yeast. In this approach, the transcriptional activator Gal4 is driven by regulatory elements (e.g., enhancers), whose spatial and temporal activity determines where Gal4 is expressed. When combined with an upstream activation sequence (UAS), Gal4 induces expression of fluorescent reporters or functional effectors in selected cell populations (**Figure 1.1**). While early Gal4 lines generated through P-element enhancer trapping often showed broad or inconsistent expression patterns (Venken, Simpson, et al., 2011), newer driver lines were developed by cloning specific enhancer fragments into standardized plasmids. This has yielded thousands of Gal4 drivers with fine-tuned expression patterns for high-resolution analysis (Pfeiffer et al., 2008).

In addition to Gal4/UAS, orthogonal binary systems—such as LexA/LexAop and QF/QUAS—allow for simultaneous labeling or manipulation of distinct cell types in the same animal. For instance, one might use Gal4/UAS to label muscles and LexA/LexAop to independently label neurons, enabling detailed visualization of synaptic interactions (Venken, Simpson, et al., 2011; see Chapter 4). These systems can also be combined with stochastic labeling methods or enhancer libraries to resolve even individual synapses.

The utility of binary systems extends beyond visualization. They also provide powerful tools for functional manipulation of synaptic development. For example, tetanus toxin light chain (TeTxLC) can be expressed in neurons to block synaptic transmission (Sweeney et al., 1995), while Channelrhodopsin—a light-gated ion channel—can be used to stimulate neuronal activity in a temporally precise manner under Gal4 control (Hwang et al., 2007; Schroll et al., 2006). Other effectors can target cell signaling, growth, or cytoskeletal dynamics, enabling researchers to probe causal relationships between gene function and synaptic outcomes.

Recent innovations in genome engineering have further expanded the capacity to visualize proteins *in vivo* at endogenous levels. The recombinase-mediated cassette exchange (RMCE) strategy has enabled precise insertion of tags into coding regions using the MiMIC and CRIMIC platforms (Venken, Schulze, et al., 2011; Nagarkar-Jaiswal et al., 2015; Li-Kroeger et al., 2018). These insertions allow real-time tracking of protein localization and dynamics within developing circuits. When paired with the split-GFP system, it becomes possible to visualize protein expression at single-cell resolution, even within densely packed tissues (Kamiyama et al., 2021; Inal et al., 2024).

Collectively, the breadth and flexibility of these tools enable researchers to visualize, manipulate, and quantify synaptic development with exceptional precision. Within the context of the NMJ, they provide direct insight into how neurons select their targets, form synaptic contacts, and establish functional connections—paving the way for detailed analyses of the mechanisms governing circuit assembly.

1.3 NEUROMUSCULAR JUNCTION OF DROSOPHILA AS A MODEL TO INVESTIGATE NEURAL CIRCUIT ASSEMBLY

Understanding how synapses form during development requires model systems that offer both accessibility and biological relevance. The *Drosophila* neuromuscular junction (NMJ) has emerged as a widely used platform for studying synaptic development due to its genetic tractability, highly stereotyped architecture, and functional parallels to vertebrate synapses. Importantly, *Drosophila* shares approximately 75% of genes implicated in human disease, making it an effective model for probing the cellular mechanisms underlying neurodevelopmental disorders (Mirzoyan et al., 2019).

The *Drosophila* NMJ provides exceptional temporal and spatial resolution for observing synapse formation *in vivo*. Synaptogenesis begins in late embryogenesis and proceeds over a narrow time window, from approximately 13 to 17 hours after egg laying (AEL), during which motor neurons establish synaptic contacts with their target muscles (Crisp et al., 2008). This tight developmental timeframe allows researchers to track individual steps of synapse formation at sub-hourly resolution—an advantage rarely possible in vertebrate models.

Another key strength of the *Drosophila* NMJ is its optical accessibility. Embryos can be imaged either intact or following dissection, with each method offering distinct benefits. Live, intact embryos allow for dynamic imaging of cellular behaviors in real time, especially when paired with genetically encoded fluorescent reporters. Alternatively, dissection removes internal structures such as yolk and gut, enhancing optical clarity and permitting high-resolution imaging of NMJs located deep within the body wall musculature (Hardin, 2006). Upon filleting, the entire muscle field is revealed, enabling detailed analysis of muscle morphology, innervation patterns, and synaptic dynamics.

The anatomical simplicity of the NMJ further facilitates analysis. Unlike vertebrate muscles—which initially receive input from multiple motor neurons and then undergo synaptic pruning—*Drosophila* muscles are innervated only by the neurons that will ultimately persist into larval stages (Suzuki et al., 2000). This direct pattern of innervation reduces ambiguity and makes it easier to interpret developmental outcomes at single-cell resolution.

From a technical standpoint, the large size and defined positions of embryonic muscles enable targeted manipulations and direct dye labeling. For example, researchers can perform electrophysiological recordings or apply fluorescent markers to specific muscles with high precision (Johansen et al., 1989; Ritzenthaler et al., 2000). Moreover, paired with the binary expression systems described in Section 1.2, these techniques offer fine control over the visualization and manipulation of both pre- and postsynaptic elements.

Together, these features make the *Drosophila* NMJ an ideal system for investigating how neurons identify synaptic partners, establish initial contacts, and assemble functional synapses. The combination of genetic tools, temporal resolution, and anatomical clarity enables mechanistic insight into each stage of circuit formation.

1.4 DEVELOPMENT OF MUSCLES: MYOBLAST TO CONTRACTILE MUSCLE

The neuromuscular junction (NMJ) in *Drosophila* serves as a powerful model for studying the cellular and molecular events underlying synaptogenesis. Compared to the complexity of the central nervous system, the embryonic musculature is composed of a relatively small and stereotyped set of 30 muscle fibers per hemisegment, each innervated by one to three motor neurons (Arzan Zarin & Labrador, 2019; Johansen et al., 1989). These muscles are large, reproducible, and spatially well-defined, enabling precise investigations of how motor axons identify and synapse with their targets.

Muscles in *Drosophila* are arranged in segmentally repeating patterns, with abdominal segments A2–A7 displaying highly stereotypic and reproducible patterns (Bate, 1993). Each muscle fiber occupies a stereotyped position on the inner body wall and is characterized by both its spatial domain—dorsal (D), lateral (L), or ventral (V)—and its orientation of insertion. Longitudinal (L) muscles span the anterior-posterior axis; transverse (T) muscles span the dorsoventral axis; and oblique (O) or acute (A) muscles insert at diagonal angles. This naming convention corresponds to muscle geometry, while an alternative system numbers the muscles from 1 to 30 for consistent reference across studies (Bate, 1993; Dobi et al., 2015; Crossley, 1978).

This architectural precision originates from the organization and behavior of two distinct classes of myoblasts: founder cells (FCs) and fusion-competent myoblasts (FCMs). FCs determine the identity, position, and morphology of each muscle fiber. Each FC undergoes successive rounds of fusion with FCMs, which contribute additional cytoplasm and nuclei (Bate, 1993; Dobi et al., 2015). This cell-fusion process underlies the transformation from individual progenitors into mature, multinucleated muscle fibers.

Muscle development proceeds in two major phases. During the early phase—beginning at stage 12 (approximately 7:30 h AEL)—each FC initiates limited fusion events to establish small, spatially localized precursors. These precursors serve as a scaffold for the body wall musculature (Bate 1990). In the later phase, which extends through stage 15 (~13:00 h AEL), these precursors undergo extensive fusion with additional FCMs to generate fully elongated muscle fibers. To date, around 20 transcription factors have been identified as identity genes, each conferring specific characteristics on the resulting muscle (Dobi et al., 2015). Thus, the precise patterning of the musculature is a direct consequence of FC positional identity and fusion behavior.

Following fusion, the fibers transition from morphologically complete to functionally active. Around stage 16 (13:45–14:00 h AEL), the contractile machinery of the muscles begins to assemble, initiating endogenous contractions (Broadie & Bate, 1993b). This functional maturation coincides with the arrival of motor axons at the muscle surface. Although muscle development occurs independently of innervation, the spatial refinement of neuromuscular connections relies on these timely interactions (Broadie & Bate, 1993b; Prokop et al., 1996).

Muscle formation also exhibits a spatial gradient. Dorsal muscles generally complete fusion earlier than ventral ones, suggesting that myogenic progression is temporally patterned across the body wall (Beckett & Baylies, 2007). During this window, adjacent fibers can become transiently coupled—both electrically and physically—though these connections are rapidly lost upon motor neuron contact (Broadie & Bate, 1993b).

The precision and timing of muscle development are essential for ensuring successful neuromuscular targeting. The identity, position, and contractile readiness of each muscle fiber contribute to the ability of incoming axons to recognize and synapse with their appropriate partners.

1.5 AXONAL OUTGROWTH

The formation of neuromuscular circuits begins with a critical event: the extension of motor neuron axons from the central nervous system (CNS) to their specific target muscles. In *Drosophila* embryos, this process initiates at approximately 9:30–10:00 h AEL, corresponding to embryonic stage 13 (Johansen et al., 1989; Keshishian et al., 1996). Given the complexity and precision required in forming functional connections, axons rely on tightly regulated developmental programs to navigate the body plan and identify appropriate targets.

To accomplish this, axons utilize a two-step navigation strategy: selective fasciculation, where axons bundle together during early extension, and selective defasciculation, where they separate at key choice points to reach specific muscles. These processes are modulated by attractive and repulsive molecular cues in the environment (Jeong, 2021), enabling reproducible pathfinding across segments (**Figure 1.2**).

As motor axons exit the CNS, they organize into distinct bundles. The intersegmental nerve (ISN) exits anteriorly, forming the primary pioneering bundle. It is joined by other nerves such as ISNb and ISNd, which follow similar trajectories. Additional nerves—SNa and SNc—exit more posteriorly, and the transverse nerve (TN) leaves the CNS through a dorsal exit site (Chiba, 1999). Once in the periphery, axons undergo selective defasciculation to form branches that project toward defined muscle domains. For example, ISNb makes an internal (dorsal) turn at muscle 28 and then diverges to innervate ventral muscles. SNa reaches the lateral edge of muscle 12, where it bifurcates to target either lateral muscles (22–24) or muscles 5 and 8 (**Figure 1.2**; Chiba, 1999).

The timing of these events is also highly regulated. The ISN pioneers axonal outgrowth at around 9:00–9:15 h AEL, navigating through unfused myoblasts and responding to cues from surrounding tissues such as trachea and adult muscle precursor cells (AMPs) (Johansen et al., 1989; Keshishian et al., 1996; Lavergne et al., 2020). ISNb and ISNd follow shortly after, around 9:30–9:45 h AEL, targeting ventral muscles. SNa emerges by approximately 11 h AEL to reach lateral domains, while SNc is the last to arrive at external ventral muscles (Broadie & Bate, 1993a; Chiba, 1999). This ordered temporal sequence ensures that pathfinding and target recognition proceed in a coordinated manner.

Peripheral guidance is not determined by axons alone. Muscle founder cells (FCs) play an instructive role by providing spatially restricted signals that promote accurate pathfinding. In a seminal study, Landgraf et al. (1999) used the Gal4/UAS system to express activated Notch in the mesoderm, thereby blocking muscle fusion and increasing FC number. This manipulation disrupted axonal defasciculation: axons extended into the periphery but failed to form distinct branches. For instance, ISNb remained fasciculated with ISN and bypassed its ventral targets. Remarkably, the presence of even a single FC was sufficient to redirect ISNb toward the correct muscle, indicating that FCs provide both necessary and sufficient guidance cues.

In addition to FCs, adult muscle precursor cells (AMPs) contribute to axonal navigation by acting as spatial regulators at branch points. Lavergne et al. (2020) found that lateral AMPs (L-AMPs) played a critical role in SNa sub-branching. When L-AMPs were ablated, the posterior branch of SNa failed to defasciculate from the dorsally projecting MN22-24 branch, leading to mistargeting. These findings support the notion that AMPs function as spatial checkpoints, facilitating local branching decisions and refining axonal trajectories.

Once axons reach their general target domains, they enter a surveillance phase. During this stage, axon terminals extend filopodia to explore the environment and sample nearby muscles until appropriate synaptic partners are recognized. This process marks the transition from navigation to target selection, which is addressed in the next section.

1.6 AXONAL TARGETING AND INITIAL CONTACT WITH THE MUSCLE

Once an axon arrives in its target domain, its growth cone transitions from long-range pathfinding to a process of local surveillance to select its final partner. This search is mediated by the growth cone’s filopodia—fine, actin-rich protrusions that actively explore the local environment by processing attractive and repulsive guidance cues (Ruhoff et al., 2025). These dynamic structures can extend up to 20 µm, allowing a single growth cone to sample multiple potential muscle targets simultaneously (Halpern et al., 1991; Johansen et al., 1989). The stereotyped exploratory behavior of the ISNb growth cone serves as a classic example of this process; after exploring the surfaces of muscles 7, 6, and 13, a new growth cone emerges to contact muscle 12, forming a stable connection at a precise, reproducible site on its anterolateral edge (Johansen et al., 1989; Yoshihara et al., 1997). These targeting events follow a reproducible but segregated temporal sequence, where ventral contacts on muscles 7/6 develop approximately 30 minutes prior to dorsal contacts made by the ISN on muscles 1 and 9 (Johansen et al., 1989; Yoshihara et al., 1997).

Historically, this process was viewed as a one-sided affair in which the neuron actively surveyed the environment for a passive muscle. While genetic experiments challenged this simple view by showing that muscle-derived cues are critical for inducing innervation and guiding the axon terminal to the proper subcellular location, these studies still framed the muscle as a passive provider of cues, waiting to be found (Chang & Keshishian, 1996; Prokop et al., 1996). The paradigm shifted fundamentally with the discovery of dynamic, postsynaptic filopodia on the muscle surface, which revealed that muscles are, in fact, active participants in establishing contact (Bate, 1990; Ritzenthaler et al., 2000; Suzuki et al., 2000). This finding of active muscle participation has since been shown to be a conserved mechanism, with similar structures identified in rodent models (Misgeld et al., 2002; Uhm et al., 2001).

These muscle filopodia, which appear as early as 10:00 h AEL and can reach lengths of up to 40 µm, are thin protrusions with a diameter of ~0.1-0.2 µm (Ritzenthaler et al., 2000). Initially, these myopodia are distributed randomly across the muscle surface. This changes upon contact, as target recognition is achieved through a bidirectional interaction between presynaptic and postsynaptic filopodia. When the correct neuron-muscle pair makes contact, specific cell-surface recognition molecules are assessed at the filopodial tips to ensure a proper match (Kohsaka & Nose, 2009; Ritzenthaler & Chiba, 2003). A successful recognition event triggers a positive feedback loop, leading to the rapid clustering of muscle filopodia at the contact site, which coincides with the future location of the synapse where post-synaptic proteins like Dlg are recruited (Kohsaka et al., 2007). This clustering is critical; if it fails, synapses form smaller or do not form at all (Kohsaka & Nose, 2009; Ritzenthaler & Chiba, 2003). Following this recognition event, the clustered filopodia undergo a morphological transformation (**Figure 1.3A**), first resolving into a sheet-like structure that appears to "zipper" the pre- and postsynaptic membranes together (**Figure 1.3B**), and then disappearing as the axon terminal flattens against the muscle (**Figure 1.3C**). Despite the importance of these interactions, their precise functions remain an area of active investigation, with hypotheses suggesting they may serve to increase contact area, penetrate the extracellular matrix, present recognition molecules, or facilitate direct information exchange (Carrero-Martínez & Chiba, 2009; Nose, 2012; Ritzenthaler & Chiba, 2003).

1.7 OVERVIEW OF DISSERTATION

The formation of precise neuromuscular connections is critical for motor circuit function and is guided by dynamic cellular interactions during development. A key unresolved aspect of this process is the role of filopodia—fine actin-rich protrusions—on both neurons and muscles during synaptic partner recognition and synapse formation. This dissertation investigates the cellular basis of neuromuscular synaptogenesis in *Drosophila melanogaster*, with a particular focus on how filopodia contribute to the spatial and temporal refinement of these circuits.

Chapter 2 introduces a retrograde labeling technique for visualizing individual embryonic motor neurons with high spatial resolution. By applying lipophilic dyes directly to embryonic fillet preparations, we achieve continuous and multicolor labeling of motor neurons. This method enables detailed structural analysis of dendritic morphology and offers a powerful approach for mapping synaptic connectivity in the developing *Drosophila* motor system.

In Chapter 3, we address the need for nanoscale resolution in examining synaptic structures by adapting stochastic optical reconstruction microscopy (STORM) for use in *Drosophila* neurons. We provide a comprehensive guide to sample preparation, antibody labeling, and multicolor imaging both *in vitro* and *in vivo*. The methodological advancements described here open up new possibilities for visualizing subcellular interactions between neurons and muscles, including the nanoscale features of filopodia.

Chapter 4 focuses on the development of new genetic tools to label neuromuscular junctions at varying spatial scales. We identify and validate orthogonal Gal4 and LexA driver lines that allow two-color visualization of synaptic partners. These include Gal4 lines that label muscle subsets or individual fibers, as well as LexA drivers that target motor neurons at different developmental stages. Using these tools, we perform time-lapse imaging of NMJ formation in selected muscles, uncovering dynamic differences in morphology that may contribute to synaptic specificity.

Chapter 5 builds directly on these imaging tools to explore the function of muscle filopodia during synaptogenesis. We identify two hotspots of filopodia activity on muscle 12 that correspond to the contact sites for ISNb and SNa motor neurons. Using structural illumination microscopy, we characterize filopodial dynamics and show that manipulating filopodia through expression of $\mathrm{Cdc42}^{\mathrm{V12}}$, a small GTPase that regulates filopodia activity, disrupts motor axon targeting, guidance, and synapse formation. These findings support a model in which muscle filopodia play active and spatially compartmentalized roles in directing motor neuron behavior and refining neuromuscular connectivity.

Finally, Chapter 6 summarizes the collective findings and discusses broader implications for how early synaptic decisions are regulated at the cellular level. We consider how filopodia-mediated interactions shape circuit specificity and identify remaining questions about the molecular cues that coordinate bidirectional communication between motor neurons and their muscle targets.

Together, the work presented in this dissertation offers new insights into the developmental strategy of synaptogenesis, emphasizing the muscle's active role in shaping neuromuscular circuit assembly and the utility of advanced imaging and genetic tools in revealing these mechanisms.

1.8 FIGURES

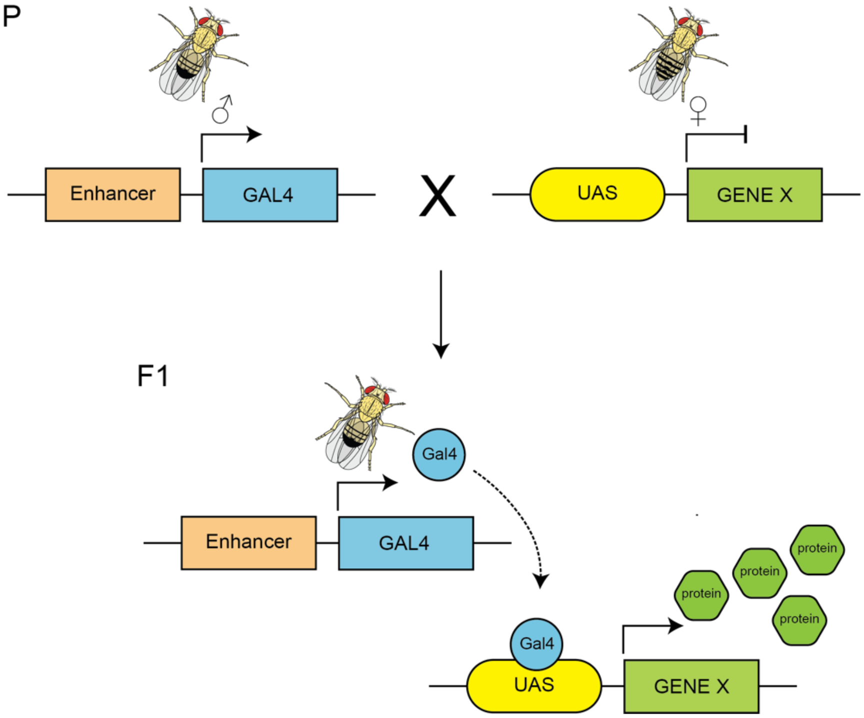

Figure 1.1 Gal4/UAS Binary expression system

Gal4 (blue) is expressed in the parent line (P) independent of UAS-Gene X (the reporter line). However, UAS-Gene X is only activated in the presence of Gal4. Enhancer sequence (orange) dictates which cells and what time Gal4 will be produced. The progeny (F1) of the Gal4-driver UAS-reporter has the necessary components for transgene expression. Gal4 protein (blue circle) upon translation binds to the UAS sequence (yellow) activating transcription of Gene X downstream, leading to expression of protein of choice (green).

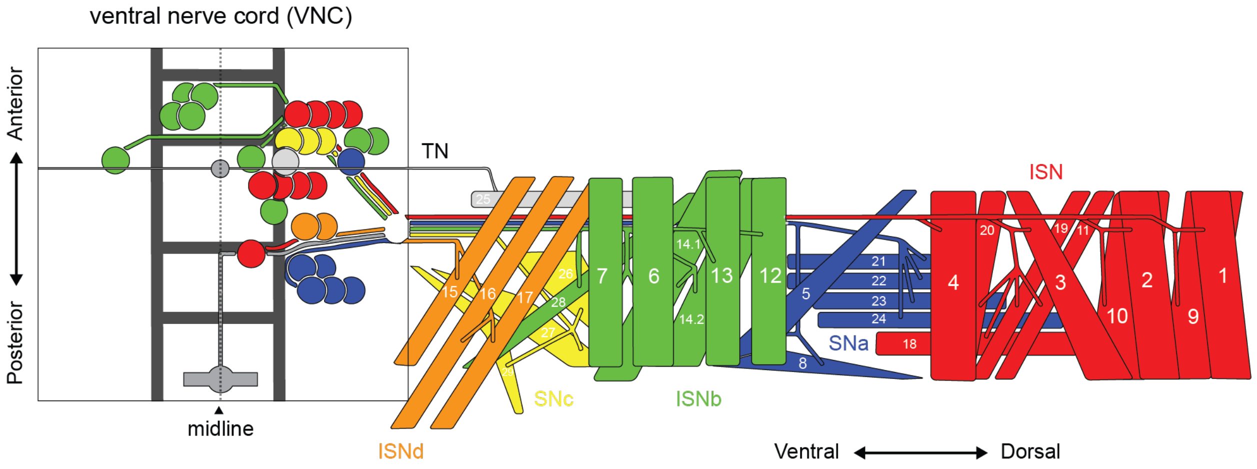

Figure 1.2 Stereotypical organization of the Drosophila embryonic muscle wall (*modified from* Inal et al, 2020).

A2-A7 muscle pattern in embryonic body wall. 30 muscles are innervated by motor neurons that extend from the ventral nerve cord (VNC). The nerves and muscles they innervate are color coded. From ventral to dorsal: ISNd (orange) innervates muscles 15-17. SNc (yellow) innervates muscles 26, 27 and 29. TN (gray) targets muscle 25. ISNb (green) innervates 28, 14.1, 14.2, 7, 6, 13, 12. SNa (blue) innervates muscles 5/8 and 21-24. ISN (red) innervates 4, 18, 20, 19, 11, 3, 2, 10, 1, 9.

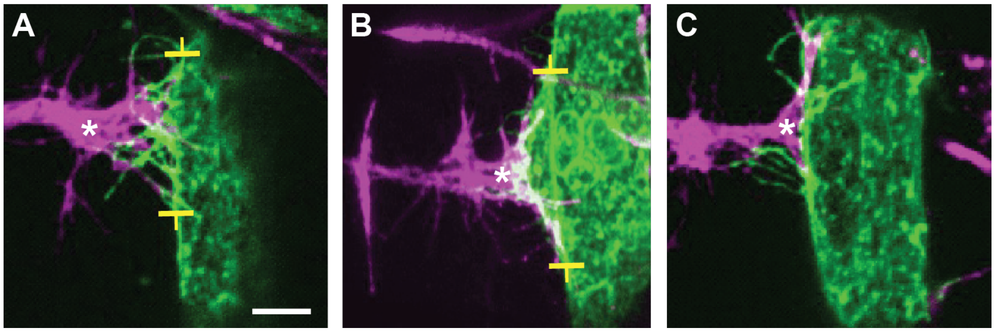

Figure 1.3 Development of *Drosophila* Neuromuscular Junction

The motor neuron (MN12) is labeled with anti-HRP antibody (magenta) and a single muscle (M12) is labeled using *Tey*^{5053A}*-GAL4* driver with UAS-CD4::tdGFP, visualized using anti-GFP (green) **(A)** Filopodia clustering at the NMJ. Muscle filopodia (green) are tightly intermingled with neuron filopodia (magenta). **(B)** The muscle filopodia have left their place to a sheet-like structure. The growth cone (*) is closely associated with the muscle membrane. Overlapping interactions in white. T-bars in (A) and (B) mark the edge of the muscle from which filopodia (A) or sheet-like structure (B) emanate. **(C)** Final phase of morphogenesis resembling the smoother surface of the larval muscle (less protrusions here), while the growth cone is completely against the edge of the muscle. Scalebar: 5 µm.

1.9 REFERENCES

Arain, M., Haque, M., Johal, L., Mathur, P., Nel, W., Rais, A., Sandhu, R., & Sharma, S. (2013). Maturation of the adolescent brain. *Neuropsychiatric Disease and Treatment*, *9*, 449–461. https://doi.org/10.2147/NDT.S39776

Arzan Zarin, A., & Labrador, J.-P. (2019). Motor axon guidance in Drosophila. *Seminars in Cell & Developmental Biology*, *85*, 36–47. https://doi.org/10.1016/j.semcdb.2017.11.013

Azevedo, F. A. C., Carvalho, L. R. B., Grinberg, L. T., Farfel, J. M., Ferretti, R. E. L., Leite, R. E. P., Filho, W. J., Lent, R., & Herculano-Houzel, S. (2009). Equal numbers of neuronal and nonneuronal cells make the human brain an isometrically scaled-up primate brain. *Journal of Comparative Neurology*, *513*(5), 532–541. https://doi.org/10.1002/cne.21974

Bate, M. (1990). The embryonic development of larval muscles in *Drosophila*. *Development*, *110*(3), 791–804. https://doi.org/10.1242/dev.110.3.791

Bate, M. (Ed.). (1993). *The development of Drosophila melanogaster*. Cold Spring Habor Laboratory Press.

Beckett, K., & Baylies, M. K. (2007). 3D analysis of founder cell and fusion competent myoblast arrangements outlines a new model of myoblast fusion. *Developmental Biology*, *309*(1), 113–125. https://doi.org/10.1016/j.ydbio.2007.06.024

Broadie, K., & Bate, M. (1993b). Innervation directs receptor synthesis and localization in Drosophila embryo synaptogenesis. *Nature*, *361*(6410), 350–353. https://doi.org/10.1038/361350a0

Broadie, K. S., & Bate, M. (1993). Development of the embryonic neuromuscular synapse of Drosophila melanogaster. *The Journal of Neuroscience: The Official Journal of the*

Society for Neuroscience, *13*(1), 144–166. https://doi.org/10.1523/JNEUROSCI.13-01-00144.1993

Carrero-Martínez, F. A., & Chiba, A. (2009). Cell Adhesion Molecules at the Drosophila Neuromuscular Junction. In H. Umemori & M. Hortsch (Eds.), *The Sticky Synapse* (pp. 11–37). Springer New York. https://doi.org/10.1007/978-0-387-92708-4_2

Chang, T. N., & Keshishian, H. (1996). Laser Ablation of *Drosophila* Embryonic Motoneurons Causes Ectopic Innervation of Target Muscle Fibers. *The Journal of Neuroscience*, *16*(18), 5715–5726. https://doi.org/10.1523/JNEUROSCI.16-18-05715.1996

Chiba, A. (1999). Early Development of the Drosophila Neuromuscular Junction: A Model for Studying Neuronal Networks in Development. *International Review of Neurobiology*, *43*, 1–24. https://doi.org/10.1016/S0074-7742(08)60538-3

Crisp, S., Evers, J. F., Fiala, A., & Bate, M. (2008). The development of motor coordination in *Drosophila* embryos. *Development*, *135*(22), 3707–3717. https://doi.org/10.1242/dev.026773

Crossley, A. C. (1978). The morphology and development of the Drosophila muscular system. *The Genetics and Biology of Drosophila*, *b*, 499–560.

Currie, D. A., Truman, J. W., & Burden, S. J. (1995). Drosophila glutamate receptor RNA expression in embryonic and larval muscle fibers. *Developmental Dynamics*, *203*(3), 311–316. https://doi.org/10.1002/aja.1002030303

Dobi, K. C., Schulman, V. K., & Baylies, M. K. (2015). Specification of the somatic musculature in *Drosophila*. *WIREs Developmental Biology*, *4*(4), 357–375. https://doi.org/10.1002/wdev.182

Dorkenwald, S., Matsliah, A., Sterling, A. R., Schlegel, P., Yu, S., McKellar, C. E., Lin, A., Costa, M., Eichler, K., Yin, Y., Silversmith, W., Schneider-Mizell, C., Jordan, C. S., Brittain, D., Halageri, A., Kuehner, K., Ogedengbe, O., Morey, R., Gager, J., … Zandawala, M. (2024). Neuronal wiring diagram of an adult brain. *Nature*, *634*(8032), 124–138. https://doi.org/10.1038/s41586-024-07558-y

Ehmann, N., Van De Linde, S., Alon, A., Ljaschenko, D., Keung, X. Z., Holm, T., Rings, A., DiAntonio, A., Hallermann, S., Ashery, U., Heckmann, M., Sauer, M., & Kittel, R. J. (2014). Quantitative super-resolution imaging of Bruchpilot distinguishes active zone states. *Nature Communications*, *5*(1), 4650. https://doi.org/10.1038/ncomms5650

Gramates, L., & Budnik, V. (1999). Assembly and Maturation of the Drosophila Larval Neuromuscular Junction. *International Review of Neurobiology*, *43*, 93–117. https://doi.org/10.1016/S0074-7742(08)60542-5

Guan, B., Hartmann, B., Kho, Y.-H., Gorczyca, M., & Budnik, V. (1996). The Drosophila tumor suppressor gene, dlg, is involved in structural plasticity at a glutamatergic synapse. *Current Biology : CB*, *6*(6), 695–706. https://doi.org/10.1016/s0960-9822(09)00451-5

Hardin, J. (2006). Confocal and Multi-Photon Imaging of Living Embryos. In J. B. Pawley (Ed.), *Handbook Of Biological Confocal Microscopy* (pp. 746–768). Springer US. https://doi.org/10.1007/978-0-387-45524-2_43

Herculano-Houzel, S., Mota, B., & Lent, R. (2006). Cellular scaling rules for rodent brains. *Proceedings of the National Academy of Sciences*, *103*(32), 12138–12143. https://doi.org/10.1073/pnas.0604911103

Hoang, B., & Chiba, A. (2001). Single-Cell Analysis of Drosophila Larval Neuromuscular Synapses. *Developmental Biology*, *229*(1), 55–70. https://doi.org/10.1006/dbio.2000.9983

Hunter, D., DeFelipe, J., Mehta, A. R., & Conway, B. R. (2025). Art, Intuition, and Identity in Ramón y Cajal. *The Neuroscientist*, *31*(2), 125–140. https://doi.org/10.1177/10738584241234049

Hwang, R. Y., Zhong, L., Xu, Y., Johnson, T., Zhang, F., Deisseroth, K., & Tracey, W. D. (2007). Nociceptive Neurons Protect Drosophila Larvae from Parasitoid Wasps. *Current Biology*, *17*(24), 2105–2116. https://doi.org/10.1016/j.cub.2007.11.029

Inal, M. A., Banzai, K., Kamiyama, R., & Kamiyama, D. (2024). Cell-type-specific labeling of endogenous proteins using the split GFP system in Drosophila. In *Methods in Cell Biology* (p. S0091679X2400195X). Elsevier. https://doi.org/10.1016/bs.mcb.2024.08.012

Jeong, S. (2021). Molecular Mechanisms Underlying Motor Axon Guidance in Drosophila. *Molecules and Cells*, *44*(8), 549–556. https://doi.org/10.14348/molcells.2021.0129

Johansen, J., Halpern, M., & Keshishian, H. (1989). Axonal guidance and the development of muscle fiber-specific innervation in Drosophila embryos. *The Journal of Neuroscience*, *9*(12), 4318–4332. https://doi.org/10.1523/JNEUROSCI.09-12-04318.1989

Kamiyama, R., Banzai, K., Liu, P., Marar, A., Tamura, R., Jiang, F., Fitch, M. A., Xie, J., & Kamiyama, D. (2021). Cell-type–specific, multicolor labeling of endogenous proteins with split fluorescent protein tags in *Drosophila*. *Proceedings of the National Academy of Sciences*, *118*(23), e2024690118. https://doi.org/10.1073/pnas.2024690118

Kelliher, M. T., Yue, Y., Ng, A., Kamiyama, D., Huang, B., Verhey, K. J., & Wildonger, J. (2018). Autoinhibition of kinesin-1 is essential to the dendrite-specific localization of Golgi outposts. *Journal of Cell Biology*, *217*(7), 2531–2547. https://doi.org/10.1083/jcb.201708096

Keshishian, H., Broadie, K., Chiba, A., & Bate, M. (1996). The Drosophila Neuromuscular Junction: A Model System for Studying Synaptic Development and Function. *Annual Review of Neuroscience*, *19*(Volume 19, 1996), 545–575. https://doi.org/10.1146/annurev.ne.19.030196.002553

Landgraf, M., Baylies, M., & Bate, M. (1999). Muscle founder cells regulate defasciculation and targeting of motor axons in the Drosophila embryo. *Current Biology*, *9*(11), 589–592. https://doi.org/10.1016/S0960-9822(99)80262-0

Landgraf, M., Bossing, T., Technau, G. M., & Bate, M. (1997). The Origin, Location, and Projections of the Embryonic Abdominal Motorneurons of *Drosophila*. *The Journal of Neuroscience*, *17*(24), 9642–9655. https://doi.org/10.1523/JNEUROSCI.17-24-09642.1997

Lavergne, G., Zmojdzian, M., Da Ponte, J. P., Junion, G., & Jagla, K. (2020). *Drosophila* adult muscle precursor cells contribute to motor axon pathfinding and proper innervation of embryonic muscles. *Development*, dev.183004. https://doi.org/10.1242/dev.183004

Liao, W., Cao, L., Leng, L., Wang, S., He, X., Dong, Y., Yang, R., & Bai, G. (2023). Lack of functional brain connectivity was associated with poor inhibition in children with attention-deficit/hyperactivity disorder using near-infrared spectroscopy. *Frontiers in Psychiatry*, *14*, 1221242. https://doi.org/10.3389/fpsyt.2023.1221242

Li-Kroeger, D., Kanca, O., Lee, P.-T., Cowan, S., Lee, M. T., Jaiswal, M., Salazar, J. L., He, Y., Zuo, Z., & Bellen, H. J. (2018). An expanded toolkit for gene tagging based on MiMIC and scarless CRISPR tagging in Drosophila. *eLife*, *7*, e38709. https://doi.org/10.7554/eLife.38709

McGorty, R., Kamiyama, D., & Huang, B. (2013). Active microscope stabilization in three dimensions using image correlation. *Optical Nanoscopy*, *2*(1), 3. https://doi.org/10.1186/2192-2853-2-3

Mirzoyan, Z., Sollazzo, M., Allocca, M., Valenza, A. M., Grifoni, D., & Bellosta, P. (2019). Drosophila melanogaster: A Model Organism to Study Cancer. *Frontiers in Genetics*, *10*, 51. https://doi.org/10.3389/fgene.2019.00051

Mullin, A. P., Gokhale, A., Moreno-De-Luca, A., Sanyal, S., Waddington, J. L., & Faundez, V. (2013). Neurodevelopmental disorders: Mechanisms and boundary definitions from genomes, interactomes and proteomes. *Translational Psychiatry*, *3*(12), e329. https://doi.org/10.1038/tp.2013.108

Nagarkar-Jaiswal, S., Lee, P.-T., Campbell, M. E., Chen, K., Anguiano-Zarate, S., Cantu Gutierrez, M., Busby, T., Lin, W.-W., He, Y., Schulze, K. L., Booth, B. W., Evans-Holm, M., Venken, K. J., Levis, R. W., Spradling, A. C., Hoskins, R. A., & Bellen, H. J. (2015). A library of MiMICs allows tagging of genes and reversible, spatial and temporal knockdown of proteins in Drosophila. *eLife*, *4*, e05338. https://doi.org/10.7554/eLife.05338

Petersen, S. A., Fetter, R. D., Noordermeer, J. N., Goodman, C. S., & DiAntonio, A. (1997). Genetic Analysis of Glutamate Receptors in Drosophila Reveals a Retrograde Signal Regulating Presynaptic Transmitter Release. *Neuron*, *19*(6), 1237–1248. https://doi.org/10.1016/S0896-6273(00)80415-8

Pfeiffer, B. D., Jenett, A., Hammonds, A. S., Ngo, T.-T. B., Misra, S., Murphy, C., Scully, A., Carlson, J. W., Wan, K. H., Laverty, T. R., Mungall, C., Svirskas, R., Kadonaga, J. T., Doe, C. Q., Eisen, M. B., Celniker, S. E., & Rubin, G. M. (2008). Tools for neuroanatomy and neurogenetics in *Drosophila*. *Proceedings of the National Academy of Sciences*, *105*(28), 9715–9720. https://doi.org/10.1073/pnas.0803697105

Prokop, A., Landgraf, M., Rushton, E., Broadie, K., & Bate, M. (1996). Presynaptic Development at the Drosophila Neuromuscular Junction: Assembly and Localization of Presynaptic Active Zones. *Neuron*, *17*(4), 617–626. https://doi.org/10.1016/S0896-6273(00)80195-6

Ritzenthaler, S., & Chiba, A. (2003). Myopodia (postsynaptic filopodia) participate in synaptic target recognition. *Journal of Neurobiology*, *55*(1), 31–40. https://doi.org/10.1002/neu.10180

Ruhoff, V. T., Leijnse, N., Doostmohammadi, A., & Bendix, P. M. (2025). Filopodia: Integrating cellular functions with theoretical models. *Trends in Cell Biology*, *35*(2), 129–140. https://doi.org/10.1016/j.tcb.2024.05.005

Saitoe, M., Tanaka, S., Takata, K., & Kidokoro, Y. (1997). Neural Activity Affects Distribution of Glutamate Receptors during Neuromuscular Junction Formation inDrosophilaEmbryos. *Developmental Biology*, *184*(1), 48–60. https://doi.org/10.1006/dbio.1996.8480

Schroll, C., Riemensperger, T., Bucher, D., Ehmer, J., Völler, T., Erbguth, K., Gerber, B., Hendel, T., Nagel, G., Buchner, E., & Fiala, A. (2006). Light-Induced Activation of Distinct Modulatory Neurons Triggers Appetitive or Aversive Learning in Drosophila Larvae. *Current Biology*, *16*(17), 1741–1747. https://doi.org/10.1016/j.cub.2006.07.023

Sink, H., & Whitington, P. M. (1991). Location and connectivity of abdominal motoneurons in the embryo and larva of *Drosophila melanogaster*. *Journal of Neurobiology*, *22*(3), 298–311. https://doi.org/10.1002/neu.480220309

Supekar, K., Uddin, L. Q., Khouzam, A., Phillips, J., Gaillard, W. D., Kenworthy, L. E., Yerys, B. E., Vaidya, C. J., & Menon, V. (2013). Brain hyperconnectivity in children with autism and its links to social deficits. *Cell Reports*, *5*(3), 738–747. https://doi.org/10.1016/j.celrep.2013.10.001

Suzuki, E., Rose, D., & Chiba, A. (2000). The ultrastructural interactions of identified pre- and postsynaptic cells during synaptic target recognition inDrosophila embryos. *Journal of Neurobiology*, *42*(4), 448–459. https://doi.org/10.1002/(SICI)1097-4695(200003)42:4<448::AID-NEU6>3.0.CO;2-H

Sweeney, S. T., Broadie, K., Keane, J., Niemann, H., & O'Kane, C. J. (1995). Targeted expression of tetanus toxin light chain in Drosophila specifically eliminates synaptic transmission and causes behavioral defects. *Neuron*, *14*(2), 341–351. https://doi.org/10.1016/0896-6273(95)90290-2

The MICrONS Consortium, Bae, J. A., Baptiste, M., Baptiste, M. R., Bishop, C. A., Bodor, A. L., Brittain, D., Brooks, V., Buchanan, J., Bumbarger, D. J., Castro, M. A., Celii, B., Cobos, E., Collman, F., Da Costa, N. M., Danskin, B., Dorkenwald, S., Elabbady, L., Fahey, P. G., … Zhang, C. (2025). Functional connectomics spanning multiple areas of mouse visual cortex. *Nature*, *640*(8058), 435–447. https://doi.org/10.1038/s41586-025-08790-w

Ueoka, I., Kawashima, H., Konishi, A., Aoki, M., Tanaka, R., Yoshida, H., Maeda, T., Ozaki, M., & Yamaguchi, M. (2018). Novel Drosophila model for psychiatric disorders including autism spectrum disorder by targeting of ATP-binding cassette protein A. *Experimental Neurology*, *300*, 51–59. https://doi.org/10.1016/j.expneurol.2017.10.027

Venken, K. J. T., Schulze, K. L., Haelterman, N. A., Pan, H., He, Y., Evans-Holm, M., Carlson, J. W., Levis, R. W., Spradling, A. C., Hoskins, R. A., & Bellen, H. J. (2011). MiMIC: A highly versatile transposon insertion resource for engineering Drosophila melanogaster genes. *Nature Methods*, *8*(9), 737–743. https://doi.org/10.1038/nmeth.1662

Venken, K. J. T., Simpson, J. H., & Bellen, H. J. (2011). Genetic Manipulation of Genes and Cells in the Nervous System of the Fruit Fly. *Neuron*, *72*(2), 202–230. https://doi.org/10.1016/j.neuron.2011.09.021

Winding, M., Pedigo, B. D., Barnes, C. L., Patsolic, H. G., Park, Y., Kazimiers, T., Fushiki, A., Andrade, I. V., Khandelwal, A., Valdes-Aleman, J., Li, F., Randel, N., Barsotti, E., Correia, A., Fetter, R. D., Hartenstein, V., Priebe, C. E., Vogelstein, J. T., Cardona, A., & Zlatic, M. (2023). The connectome of an insect brain. *Science*, *379*(6636), eadd9330. https://doi.org/10.1126/science.add9330

Yoshihara, M., Rheuben, M. B., & Kidokoro, Y. (1997). Transition from Growth Cone to Functional Motor Nerve Terminal in *Drosophila* Embryos. *The Journal of Neuroscience*, *17*(21), 8408–8426. https://doi.org/10.1523/JNEUROSCI.17-21-08408.1997

CHAPTER 2

RETROGRADE TRACING OF *DROSOPHILA* EMBRYONIC MOTOR NEURONS USING LIPOPHILIC FLUORESCENT DYES[1]

---

[1] Inal, M. A., Banzai, K., & Kamiyama, D. (2020). Retrograde Tracing of Drosophila Embryonic Motor Neurons Using Lipophilic Fluorescent Dyes. Journal of Visualized Experiments, 155, 60716. https://doi.org/10.3791/60716. Reprinted here with permission of publisher.

2.1 ABSTRACT

We describe a technique for retrograde labeling of motor neurons in Drosophila. We use an oil-dissolved lipophilic dye and deliver a small droplet to an embryonic fillet preparation by a microinjector. Each motor neuron whose membrane is contacted by the droplet can then be rapidly labeled. Individual motor neurons are continuously labeled, enabling fine structural details to be clearly visualized. Given that lipophilic dyes come in various colors, the technique also provides a means to get adjacent neurons labeled in multicolor. This tracing technique is therefore useful for studying neuronal morphogenesis and synaptic connectivity in the motor neuron system of *Drosophila*.

2.2 INTRODUCTION

The embryonic motor neuron system of *Drosophila* offers a powerful experimental model to analyze the mechanisms underlying the development of the central nervous system (CNS) (Arzan Zarin & Labrador, 2019; Kim et al., 2009; Nose, 2012). The motor neuron system is amenable to biochemical, genetic, imaging, and electrophysiological techniques. Using the techniques, genetic manipulations and functional analyses can be carried out at the level of single motor neurons (Broadie et al., 2009; Featherstone et al., 2009; Manning et al., 2012; Nose, 2012).

During early development of the nervous system, neuroblasts divide and generate a large number of glia and neurons. The spatiotemporal relationship between the delamination and the gene expression profile of neuroblasts has been previously investigated in detail (Doe, 2017; Homem & Knoblich, 2012; Urbach & Technau, 2004). In the case of the motor neuron system, the formation of embryonic neuromuscular junction (NMJ) has been extensively studied using the aCC (anterior corner cell), RP2 (raw prawn 2), and RP5 motor neurons (Carrero-Martínez & Chiba, 2009; Nose, 2012). For instance, when the RP5 motor neuron forms a nascent synaptic junction, the pre-synaptic and post-synaptic filopodia are intermingled (Kohsaka et al., 2007; Kohsaka & Nose, 2009; Ritzenthaler et al., 2000). Such direct cellular communication is vital to initiate the NMJ formation. Contrary to what we know about the peripheral nerve branches, our knowledge of how motor dendrites initiate synaptic connectivity within the CNS is still primitive.

In this report, we present a technique that allows retrograde labeling of motor neurons in embryos by means of micropipette-mediated delivery of lipophilic dyes. This technique enables us to trace the 38 motor neurons innervating each of the 30 body wall muscles in a hemi-segment at 15 h after egg laying (AEL) (Landgraf et al., 1997). By using this technique, our group has thoroughly investigated numerous gain-of-function/loss-of-function alleles (Furrer et al., 2007; Kamiyama et al., 2015; Kamiyama & Chiba, 2009). We have recently unraveled the molecular mechanisms that drive initiation of motor dendrite connectivity and demonstrated that a *Dscam1-Dock-Pak* interaction defines the site of dendrite outgrowth in the aCC motor neuron (Kamiyama et al., 2015). In general, this technique is adaptable for the phenotypic analysis of any embryonic motor neurons in wild type or mutant strains, enhancing our ability to provide new insights into the functional design of the *Drosophila* nervous system.

PROTOCOL

2.3 EQUIPMENT AND SUPPLIES

1. Materials for collecting embryos and training adults to lay eggs
    a. Prepare the filtration apparatus by severing a 50 mL tube and cutting open a hole in the cap to set a mesh filter with pores of 100 µm (**Table of Materials**) in between the tube and the cap.

       NOTE: Alternatively, cell strainers with pores of 100 µm (**Table of Materials**) can be used for the filtration step of embryo collection.

b. Make agar plates with grape agar premix (**Table of Materials**) according to the listed instructions. Briefly, gently stir 1 packet of the powder mix into 500 mL of room temperature (RT, 23 °C) dH_2O and microwave the dissolved mixture to vigorous boil. After cooling down to 70−75 °C, pour the mixture into Petri dishes (60 mm). After the agar is solidified, store plates at 4 °C.

c. Prepare yeast paste by mixing active dry yeast (**Table of Materials**) and water to a paste consistency, and keep at 4 °C.

d. Use egg-collection cages (for 60 mm Petri dish, **Table of Materials**) that provide sufficient air flow.

2. Preparation of dissection needles and dye injection micropipettes

    a. Prepare dye injection micropipette and dissection needle from the same capillary tubing with an inner diameter of 0.6 mm and an outer diameter of 1.2 mm (**Table of Materials**). Pull the capillary tubing by a micropipette puller at 7% from 170 V maximum output (**Table of Materials**) to create a sharp needle with a taper of ~0.4 cm in length.

    b. For dye injection, adjust the micropipette with a micropipette beveler (**Table of Materials**) by a bubble beveling technique described in instrument's manual.

    c. In short, soak the grinder with a wetting agent (**Table of Materials**) to prevent the water from 'dragging' the needle tip. Place the needle on the micropipette clamp at 25−30° and lower the tip onto two-thirds of the radius out from the center of the beveling surface. Grind the needle while a syringe with tubing pushes air into the needle, to ensure that the micropipette will be clear of glass shavings.

    d. Mark the micropipette with a fine-tip permanent marker to indicate the position of the opening at the tip after beveling as it is challenging to locate the narrow opening of the micropipette that is formed at an angle.

2.4 PREPARATION FOR EMBRYO COLLECTION

1. Ensure that the adult flies (20−40 wild-type *Canton-S* or *white* flies), males and females, are maintained in young (<7 days) and healthy conditions for the ideal egg collection.

   NOTE: To stimulate egg-laying, flies are trained in their egg collection cage a couple of days prior to egg collection on agar plates streaked with yeast paste at least once every day.

2.5 EMBRYO STAGING

1. Allow the flies to lay eggs overnight (or at least 15 h) at RT to collect the embryos at 15 h AEL, i.e., stage 16 (Campos-Ortega & Hartenstein, 1985), to view dendritogenesis of the aCC and RP3 motor neurons. In the morning, collect the plate with the eggs.

   NOTE: The embryos at 15 h AEL will have a distinct 4-chamber gut (Campos-Ortega & Hartenstein, 1985). For imaging different stages follow their specific morphological criteria and aging conditions.
2. To collect the embryos, dechorionate the eggs laid on the plate with 50% bleach for 5 min.
3. Once the chorions have cleared, pour the contents of the plate through the filtration apparatus or cell strainer to isolate the embryos. Using a squeeze bottle of water, dilute the bleach left on the plate and gather as many embryos as possible by decanting the mixture into the filter.
4. Wash the embryos on the filter 3−4x with more water or until the bleach odor dissipates. Remove the filter from the apparatus and wash the embryos onto another clean plate with water. Decant the water from the new plate that the embryos are on.

5. Prepare a glass slide by covering it with two layers of vinyl tape in the center, forming a rectangle. Cut a rectangular pool out of the tape using a razor blade. Place a thin strip of double-sided tape towards the upper end of the pool, this is where the embryos will be placed as shown in **Figure 2.1**.
6. Using fine forceps, individually select 5−10 embryos at 15 h AEL and place them on the double-sided tape with the dorsal side facing up. Add insect Ringer's saline ("*Drosophila* Ringer's Solution," 2007) to the dissection pool to protect the embryos from desiccation (**Figure 2.1**).

2.6 DISSECTION AND STAINING

1. Using a glass needle under a dissecting microscope (**Table of Materials**), cut through the midline of a single embryo at its surface from its posterior to its anterior end. Then drag the embryo out from the vitelline membrane from the tape onto the glass (boxed in **Figure 2.1**). Take care not to damage the interior tissues of the embryo.
2. Flip the epithelial tissues from the center and attach the epidermal edge onto the surface of the glass slide (**Figure 2.1**, inset).
3. Using a tube-connected needle with a tip opening of ~300 µm (prepared by breaking the thin tip of a dissection needle), aspirate or blow air to detach and remove the dorsal longitudinal tracheal trunks as well as any remaining guts.
4. Use 4% paraformaldehyde (PFA) in phosphate-buffered saline (PBS) to fix the embryos for 5 min at RT. Wash the embryos 3x with PBS.

5. Stain the embryos with 1 µL of anti-horseradish peroxidase antibody conjugated with cyanine 3 dye (anti-HRP Cy3) (**Table of Materials**) in 200 µL of PBS for 1 h. Wash the embryos with PBS 3x after staining.

   NOTE: The dye of anti-HRP can be changed based on the lipophilic dyes of choice for injection.

2.7 FILLING OF THE INJECTION MICRO-PIPETTE

1. Heat lipophilic dyes (5 mg/mL of DiO or DiD, **Table of Materials**) to 60 °C in a 1:10 mixture of ethanol:vegetable oil before use.
2. Prepare an oil-dissolved dye slide for the injection micropipette. Place the micropipette into the capillary holder (**Figure 2.2**, #1). Using the micromanipulator (**Table of Materials**), adjust the micropipette to be over the dye slide. Then, adjust the stage to place the micropipette onto the dye (**Figure 2.2**, #2).
3. To fill up the micropipette, use a microinjector (**Table of Materials**) (**Figure 2.2**, #3). Collect the dye in the micropipette by setting the P_i (injection pressure) between 200−500 hPa (hectopascal), the T_i (injection time) between 0.1−0.5 s and P_c (compensation pressure) to 0 hPa for 5 min (**Figure 2.2**, #4).
4. Once the dye has been collected, remove the dye slide and place the sample onto the microscope stage. Next, increase the P_c to a range of 20−60 hPa before lowering the micropipette into the sample to prevent contamination of PBS by capillary action.

2.8 DYE INJECTION INTO NEURONS

1. Locate the embryo in the center using the microscope with 10x objective lens (**Table of Materials**) and align the micropipette with the embryo.

NOTE: The size of the dye droplet can be adjusted by changing the P_i or the size of the opening of the micropipette tip. The droplet should be 10−20 μm, which is approximately the width of 1 muscle.

2. Change the objective lens to a water-immersion 40x lens (**Table of Materials**) and submerge the lens into PBS to see the embryo.
    a. Use fluorescence microscopy to check the neuronal morphology marked by anti-HRP Cy3 and determine the injection site.
    b. During injection, use brightfield microscopy to see the dye droplet. When the embryo is in focus, change the position of the micropipette to make gentle contact with the tip of the axon of interest (e.g., aCC, RP3).
    c. Drop the dye in a right abdominal (A2−A6) hemi-segment at the neuromuscular junction of aCC or RP3 (**Figure 2.3**) with either DiD or DiO, by using the neurons marked by anti-HRP Cy3. Using the hand control (mouse; **Figure 2.2**, 5) release the dye and remove the micropipette after dropping the dye with the micromanipulator and move onto the next injection site.

       NOTE: Unlike other dyes (e.g., Lucifer yellow, calcein) which spread into neighboring cells through gap junctions, lipophilic dyes associate with cell membranes and do not transfer to neighbors. Due to the relatively large size of the dye droplet, however, this technique also results in labeling of the partnering muscles (**Figure 2.3A**).
3. Incubate the sample at RT for 1 h after dye-drop before imaging.

NOTE: The protocol can be paused here before mounting, and the sample can be kept at 4 °C overnight. Lipophilic dyes can also be delivered using iontophoresis, if an intracellular direct-coupled (DC) amplifier is readily available[20].

2.9 IMAGING WITH A CONFOCAL MICROSCOPE

1. Remove the double-sided tape and vinyl tape from the glass slide with the help of forceps.
2. Prepare a cover slip (22 x 22 mm^2 No.1 cover glass) with a small amount of vacuum grease (**Table of Materials**) at the four corners and carefully place on the sample, avoiding air bubbles. Remove any excess PBS using task wipers.
3. Push down the cover slip to adjust the working distance between the objective lens and the sample. Completely seal the edges of the cover slip with nail polish.
4. Image at 10x and 100x magnification using a confocal microscope.
5. Use ImageJ software for processing raw images from the microscope (**Table of Materials**).
   NOTE: Observation must begin within 10 min after mounting for the best images. Otherwise, at RT, the dye will spread to sites adjacent to the injection site creating unwanted background for imaging. To slow down the diffusion of dye, the sample can be stored at 4 °C for a couple of hours.

2.10 REPRESENTATIVE RESULTS

A representative image of the aCC and RP3 motor neurons is shown in **Figure 2.3C** to demonstrate the multicolor labeling of motor neurons at 15 h AEL. Their dendritic morphologies are largely invariant between embryos. The staining pattern obtained with anti-HRP antibody is shown in gray. A small droplet of DiO or DiD was deposited on the NMJ of muscle 1 or 6/7, respectively. **Figure 2.4** demonstrates the capability to quantitatively measure the phenotype of interest. We counted the total number of dendrite tips in a wild type, compared with a mutant (e.g., *dscam1*$^{-/-}$).

2.11 DISCUSSION

The use of dye labeling for studying neuronal morphology has several advantages over genetic cell-labeling techniques. The dye labeling technique can minimize the amount of time needed for labeling and imaging the morphologies of motor neurons. The dye labeling process is quite fast as it takes less than 2 h and enables us to define the outline of neuronal projections. As an alternative, one can visualize the aCC motor neuron by choosing a GAL4 line that expresses the yeast GAL4 transcription factor in aCC and crossing it with a green fluorescent protein (GFP) reporter controlled by the upstream activation sequence (UAS) (Fujioka et al., 2003). A GFP labeling technique as such requires a genetic cross and thus, takes extra few days.

Another advantage of dye labeling is to permit labeling of the plasma membrane at an extremely high density. A sufficient density of lipophilic dyes can be present on every part of the membrane, allowing us to resolve the fine details of a labeled structure. By contrast, the density of GFP molecules is often dependent on the waiting period after the UAS-GAL4 system kicks in. For example, aCC starts to express GFP from 10 h AEL. By 15 h AEL when we observe, the density of GFP molecules is inadequate to cover up the entire membrane. It results in insufficient labeling of fine neuronal projections (D.K., unpublished data).

Although this technique provides several advantages, it is less advantageous when the erroneous projection of motor axons is evident. In the absence of *sidestep*, for example, motor neurons display severe axonal defects such as premature stall, segmental border crossing, and excessive branching (Sink et al., 2001). As a consequence, reaching to a certain axon terminal becomes cumbersome. The efficiency of labeling is also age-dependent, being effective in embryos younger than 20 h AEL. As the extracellular matrix proteins increase with development, the labeling of motor neurons appears to be very intricate.

The technique described here allows us to measure many morphological parameters such as neurite total length and number, and neurite branch pattern and shape (Furrer et al., 2003, 2007; Kamiyama et al., 2015; Kamiyama & Chiba, 2009; Landgraf et al., 2003). Because lipophilic carbocyanine dyes come in many colors (such as DiO, DiA, DiI, DiD, and DiR), multicolor labeling of adjacent motor neurons is also achievable. As shown in **Figure 4**, dendrites from the aCC and RP3 motor neurons extensively overlap. To further our understanding in motor circuit development, the mechanisms of dendrite-dendrite interaction will be investigated.

Here, we detail the versatile technique that provides an avenue to study neuronal connectivity in the motor circuit. Although the demonstration is restricted to the aCC and RP3 motor neurons in 15 h AEL, this technique can be applied to other motor neurons in different stages of embryonic development. If an axon terminal is accessible with an injection micropipette, this technique could also be applied to labeling of any neuron in the larval and adult stages of flies or even in other organisms.

2.12 FIGURES

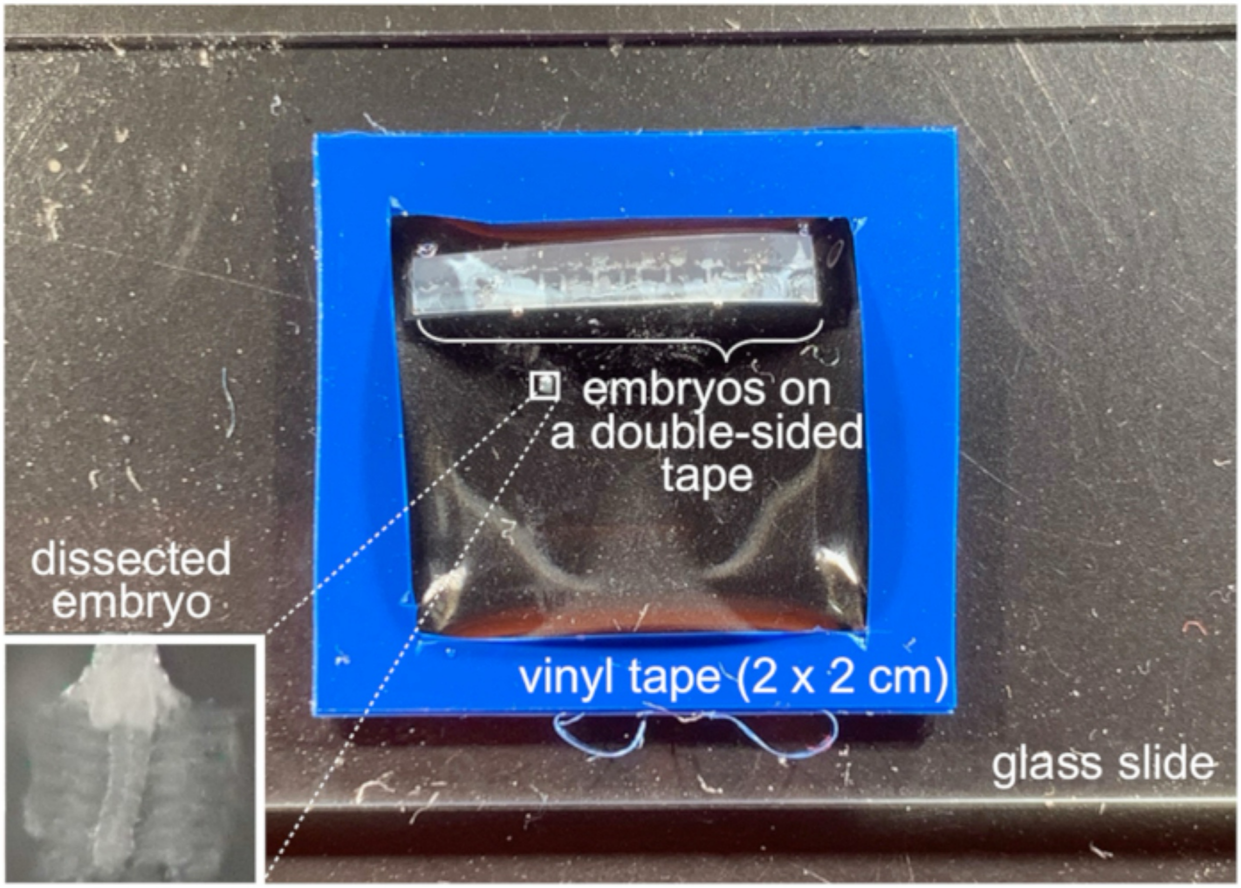

Figure 2.1 Setup of the dissection pool.

The blue chamber seen on the glass slide is created with vinyl tape keeping the buffers inside. The double-sided tape holds onto the embryos that are properly aligned. Also shown in the bottom left corner is an example of a dissected embryo in saline. The anterior end is on the top in this and all subsequent figures.

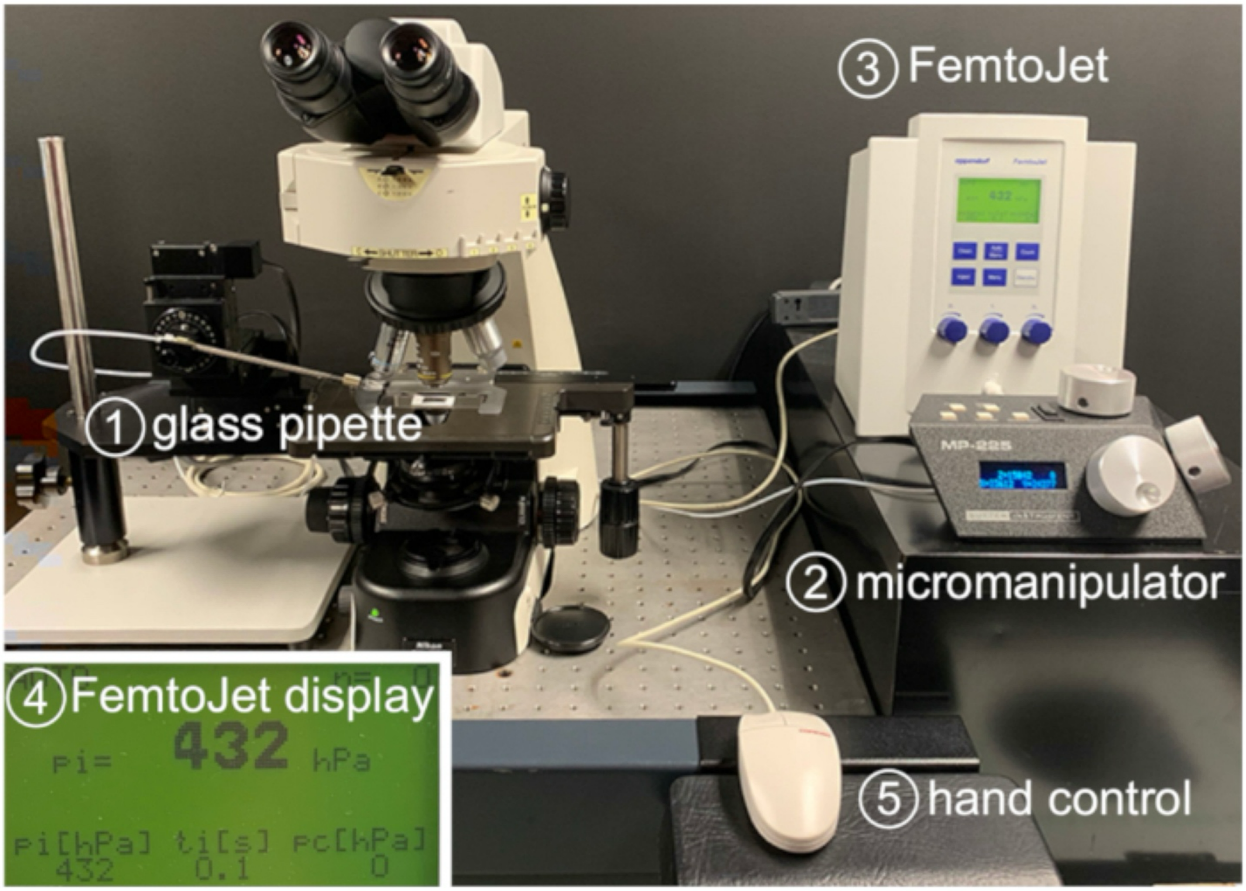

Figure 2.2 Dye injection equipment.

Glass pipette labeling in the figure demonstrates the installation site of the glass pipette (1). The epi-fluorescent microscope is equipped with a LED light source and a series of filter sets. The micromanipulator (2) and the microinjection (3) devices are labeled to the right of the microscope. The inset is a close-up of the display of microinjection device (4) with appropriate values of P_i, T_i, and P_c).

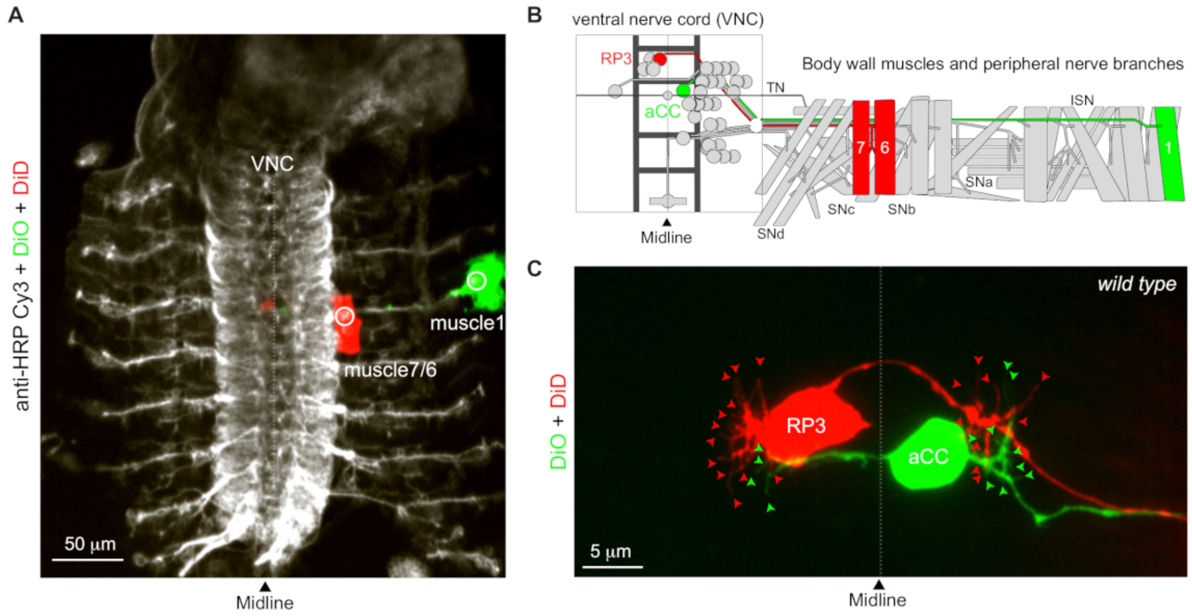

Figure 2.3 Lipophilic dye preparations of retrogradely labeled motor neurons.

(**A**) Retrograde-labeled motor neurons and their target muscles. The aCC motor neuron innervating muscle 1 (DiO: excitation/emission, 484 nm/501 nm); the RP3 motor neuron innervating muscles 6/7 (DiD: excitation/emission, 644 nm/665 nm). Note that muscles 6/7 also receive innervation from another motor neuron (MNISNb/d-Is) in larval stages; however, MNISNb/d-Is does not have an embryonic counterpart (Kim et al., 2009). Circles indicate sites of dye applications. (**B**) A schematic diagram of the body wall muscles and peripheral nerve branches in 15 h AEL. The ventral nerve cord (VNC) consists of segmentally repeated and bilaterally symmetrical neuromere with respect to the ventral midline (dotted line). Body wall muscles of each hemi-segment are innervated by 38 motor neurons. The motor neurons project their axons via six major nerve branches (ISN [intersegmental nerve], SNa [segmental nerve a], SNb, SNc, SNd, and TN [transverse nerve]). (**C**) Dendritic branches from the aCC and RP3 motor neurons show extensive overlap. Both neurons are bipolar neurons, meaning that the neurons establish two different populations of dendrites. Each neuron projects one arbor into the ipsilateral neuropil and another into the contralateral neuropil. Arrowheads point to dendritic tips. Fluorescence images were acquired with a 10x objective or a 100x oil immersion objective.

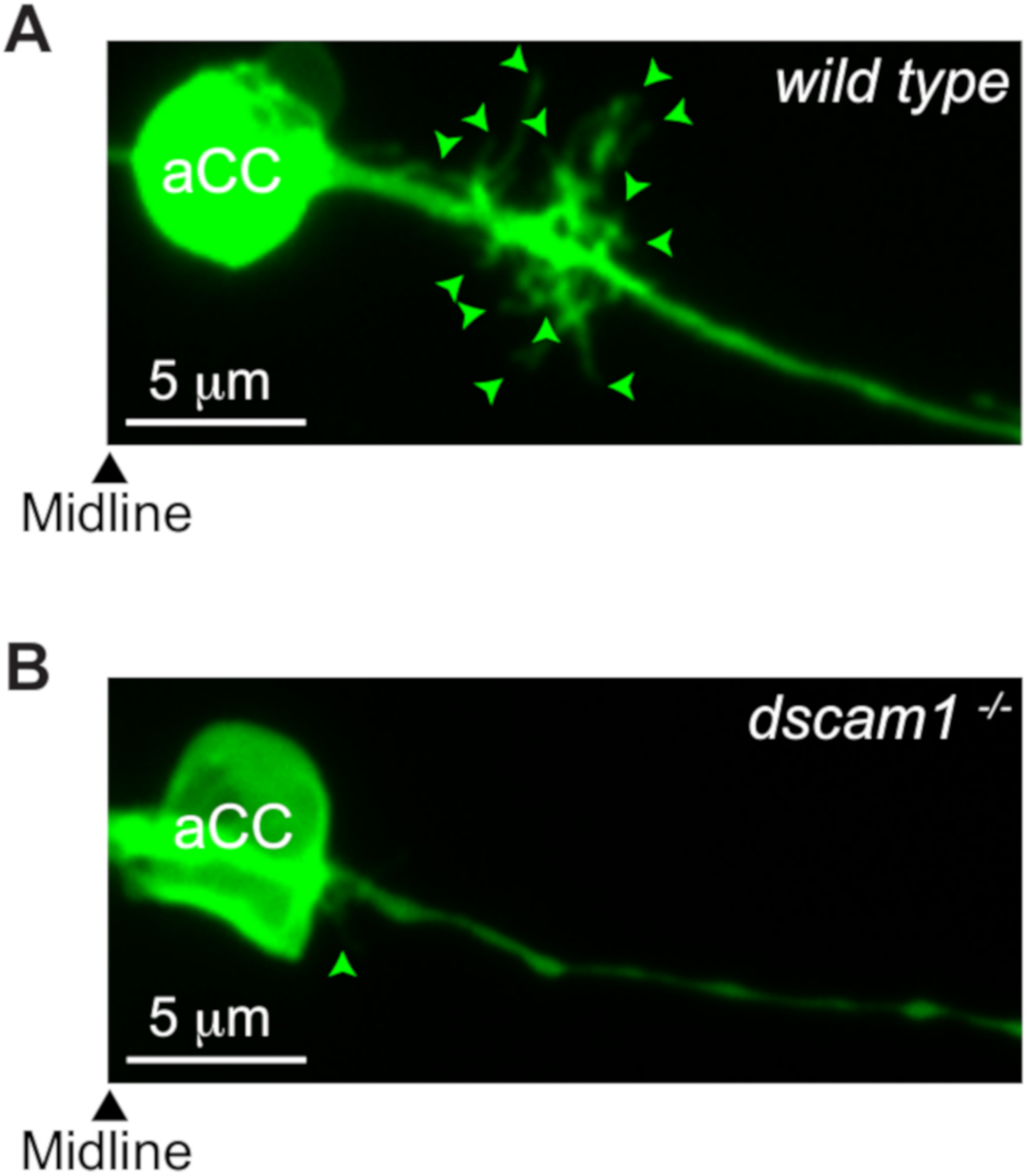

Figure 2.4 aCC dendritogenesis as revealed with retrograde labeling in hour-15 embryos. (**A**) In wild type, aCC extends its dendrites into both ipsilateral and contralateral neuropils. For simplicity, we only display the ipsilateral dendrites from aCC in this figure. aCC is labeled with

DiO, shown in green. (**B**) In *dscam1* mutants (*dscam1*$^{21/21}$ from Dr. Tzumin Lee, Janelia Research Campus), aCC has few ipsilateral dendrites in most cases observed (Kamiyama et al., 2015). Arrowheads show dendritic tips.

2.13 TABLE OF MATERIALS

Name of Material/ Equipment	**Company**	**Catalog Number**	**Comments/Description**
10x objective lens	Nikon		Plan
40x water-immersion lens	Nikon		NIR Apo
Capillary tubing	Frederick Haer&Co	27–31-1	
Confocal microscope	Andor	N/A	Dragonfly Spinning disk confocal unit
Cover glass	Corning		22x22 mm Square #1
DiD	ThermoFisher	V22886	
DiI	ThermoFisher	V22888	
DiO	ThermoFisher	V22887	
Dissecting microscope	Nikon	N/A	SMZ-U
Double Sided Tape	Scotch	665	
Dow Corning High-Vacuum Grease	Fisher Sci.	14–635-5D	
Dumont #5 Forceps	Fine Science Tools	11252–20	
Egg collection cage	FlyStuff	59–100	
FemtoJet 5247	Eppendorf	discontinued	FemtoJet 4i (Cat No. 5252000021)

ImageJ	NIH		Image processing software
Micromanipulator	Sutter	MP-225	
Micropipette beveler	Sutter	BV-10-B	
Needle puller	Narishige	PC-100	
Nutri-Fly Grape Agar Powder Premix Packets	FlyStuff	47–102	
Nylon Net Filter	Millipore		
Paraformaldehyde 16% Solution, EM grade	Electron Microscopy Sciences	15710	Any EM grades
PBS	Roche	11666789001	Sold on sigmaaldrich, boxed 10x solution
Photo-Flo 200	Kodak	146 4510	
Upright fluorescence microscope	Nikon	N/A	Eclipse Ci with a LED light source
Vinyl Electrical Tape	Scotch	6143	
VWR Cell Strainers	VWR	10199–659	
Yeast	FlyStuff	62–103	Active dry yeast (RED STAR)

2.14 REFERENCES

Arzan Zarin, A., & Labrador, J.-P. (2019). Motor axon guidance in Drosophila. *Seminars in Cell & Developmental Biology*, *85*, 36–47. https://doi.org/10.1016/j.semcdb.2017.11.013

Broadie, K., Featherstone, D. E., & Chen, K. (2009). Electrophysiological Recording in the Drosophila Embryo. *Journal of Visualized Experiments*, *27*, 1348. https://doi.org/10.3791/1348

Campos-Ortega, J. A., & Hartenstein, V. (1985). *The Embryonic Development of Drosophila melanogaster*. Springer Berlin Heidelberg. https://doi.org/10.1007/978-3-662-02454-6

Carrero-Martínez, F. A., & Chiba, A. (2009). Cell Adhesion Molecules at the Drosophila Neuromuscular Junction. In H. Umemori & M. Hortsch (Eds.), *The Sticky Synapse* (pp. 11–37). Springer New York. https://doi.org/10.1007/978-0-387-92708-4_2

Doe, C. Q. (2017). Temporal Patterning in the *Drosophila* CNS. *Annual Review of Cell and Developmental Biology*, *33*(1), 219–240. https://doi.org/10.1146/annurev-cellbio-111315-125210

Drosophila Ringer's solution. (2007). *Cold Spring Harbor Protocols*, *2007*(4), pdb.rec10919. https://doi.org/10.1101/pdb.rec10919

Featherstone, D. E., Chen, K., & Broadie, K. (2009). Harvesting and Preparing Drosophila Embryos for Electrophysiological Recording and Other Procedures. *Journal of Visualized Experiments*, *27*, 1347. https://doi.org/10.3791/1347

Fujioka, M., Lear, B. C., Landgraf, M., Yusibova, G. L., Zhou, J., Riley, K. M., Patel, N. H., & Jaynes, J. B. (2003). Even-skipped, acting as a repressor, regulates axonal projections in *Drosophila*. *Development*, *130*(22), 5385–5400. https://doi.org/10.1242/dev.00770

Furrer, M.-P., Kim, S., Wolf, B., & Chiba, A. (2003). Robo and Frazzled/DCC mediate dendritic guidance at the CNS midline. *Nature Neuroscience*, *6*(3), 223–230. https://doi.org/10.1038/nn1017

Furrer, M.-P., Vasenkova, I., Kamiyama, D., Rosado, Y., & Chiba, A. (2007). Slit and Robo control the development of dendrites in *Drosophila* CNS. *Development*, *134*(21), 3795–3804. https://doi.org/10.1242/dev.02882

Homem, C. C. F., & Knoblich, J. A. (2012). *Drosophila* neuroblasts: A model for stem cell biology. *Development*, *139*(23), 4297–4310. https://doi.org/10.1242/dev.080515

Kamiyama, D., & Chiba, A. (2009). Endogenous Activation Patterns of Cdc42 GTPase Within *Drosophila* Embryos. *Science*, *324*(5932), 1338–1340. https://doi.org/10.1126/science.1170615

Kamiyama, D., McGorty, R., Kamiyama, R., Kim, M. D., Chiba, A., & Huang, B. (2015). Specification of Dendritogenesis Site in Drosophila aCC Motoneuron by Membrane Enrichment of Pak1 through Dscam1. *Developmental Cell*, *35*(1), 93–106. https://doi.org/10.1016/j.devcel.2015.09.007

Kim, M. D., Wen, Y., & Jan, Y.-N. (2009). Patterning and organization of motor neuron dendrites in the Drosophila larva. *Developmental Biology*, *336*(2), 213–221. https://doi.org/10.1016/j.ydbio.2009.09.041

Kohsaka, H., & Nose, A. (2009). Target recognition at the tips of postsynaptic filopodia: Accumulation and function of Capricious. *Development*, *136*(7), 1127–1135. https://doi.org/10.1242/dev.027920

Kohsaka, H., Takasu, E., & Nose, A. (2007). In vivo induction of postsynaptic molecular assembly by the cell adhesion molecule Fasciclin2. *The Journal of Cell Biology*, *179*(6), 1289–1300. https://doi.org/10.1083/jcb.200705154

Landgraf, M., Bossing, T., Technau, G. M., & Bate, M. (1997). The Origin, Location, and Projections of the Embryonic Abdominal Motorneurons of *Drosophila*. *The Journal of Neuroscience*, *17*(24), 9642–9655. https://doi.org/10.1523/JNEUROSCI.17-24-09642.1997

Landgraf, M., Jeffrey, V., Fujioka, M., Jaynes, J. B., & Bate, M. (2003). Embryonic Origins of a Motor System: Motor Dendrites Form a Myotopic Map in Drosophila. *PLoS Biology*, *1*(2), e41. https://doi.org/10.1371/journal.pbio.0000041

Manning, L., Heckscher, E. S., Purice, M. D., Roberts, J., Bennett, A. L., Kroll, J. R., Pollard, J. L., Strader, M. E., Lupton, J. R., Dyukareva, A. V., Doan, P. N., Bauer, D. M., Wilbur, A. N., Tanner, S., Kelly, J. J., Lai, S.-L., Tran, K. D., Kohwi, M., Laverty, T. R., … Doe, C. Q. (2012). A Resource for Manipulating Gene Expression and Analyzing cis-Regulatory Modules in the Drosophila CNS. *Cell Reports*, *2*(4), 1002–1013. https://doi.org/10.1016/j.celrep.2012.09.009

Nose, A. (2012). Generation of neuromuscular specificity in Drosophila: Novel mechanisms revealed by new technologies. *Frontiers in Molecular Neuroscience*, *5*. https://doi.org/10.3389/fnmol.2012.00062

Ritzenthaler, S., Suzuki, E., & Chiba, A. (2000). Postsynaptic filopodia in muscle cells interact with innervating motoneuron axons. *Nature Neuroscience*, *3*, 1012–1017. https://doi.org/10.1038/79833

Sink, H., Rehm, E. J., Richstone, L., Bulls, Y. M., & Goodman, C. S. (2001). Sidestep Encodes a Target-Derived Attractant Essential for Motor Axon Guidance in Drosophila. *Cell*, *105*(1), 57–67. https://doi.org/10.1016/S0092-8674(01)00296-3

Urbach, R., & Technau, G. M. (2004). Neuroblast formation and patterning during early brain development in *Drosophila*. *BioEssays*, *26*(7), 739–751. https://doi.org/10.1002/bies.20062

CHAPTER 3

IMAGING OF IN VITRO AND IN VIVO NEURONS IN DROSOPHILA USING STOCHASTIC OPTICAL RECONSTRUCTION MICROSCOPY[2]

---

[2] Inal, M. A., Bui, K. C., Marar, A., Li, S., Kner, P., & Kamiyama, D. (2021). Imaging of In Vitro and In Vivo Neurons in *Drosophila* Using Stochastic Optical Reconstruction Microscopy. *Current Protocols*, *1*(7), e203. Reprinted here with permission of publisher.

3.1 ABSTRACT

The *Drosophila melanogaster* brain comprises different neuronal cell types that interconnect with precise patterns of synaptic connections. These patterns are essential for the normal function of the brain. To understand the connectivity patterns requires characterizing them at single-cell resolution, for which a fluorescence microscope becomes an indispensable tool. Additionally, because the neurons connect at the nanoscale, the investigation often demands super-resolution microscopy. Here, we adopt one super-resolution microscopy technique, called stochastic optical reconstruction microscopy (STORM), improving the lateral and axial resolution to ~20nm. This article extensively describes our methods along with considerations for sample preparation of neurons in vitro and in vivo, conjugation of dyes to antibodies, immunofluorescence labeling, and acquisition and processing of STORM data. With these tools and techniques, we open up the potential to investigate cell-cell interactions using STORM in the *Drosophila* nervous system.

3.2 INTRODUCTION

The nervous system of *Drosophila melanogaster* is an attractive model in which to study the molecular mechanisms of neuronal differentiation and proliferation, neurite outgrowth, synapse formation, and neurodegeneration (Bellen, Tong, & Tsuda, 2010; Clark, Zarin, Carreira-Rosario, & Doe, 2018; Doe, 2017). In particular, the ability to express transgenes has facilitated the use of Drosophila in such studies (Venken, Simpson, & Bellen, 2011). For instance, in the brain, where many neurites are entangled, it is difficult to distinguish a single neurite from others (Schefferetal., 2020). To resolve each neurite at high contrast, membrane markers are commonly expressed in small subsets of neurons in the brain. To this end, it is possible to take advantage of a transgenic fly in which the transcriptional activator *GAL4* is expressed under the control of a cell-type-specific enhancer (Manning et al., 2012). Complementary to this type of in vivo approach, one can also employ primary neuronal cultures from the *Drosophila* brain (Egger, van Giesen, Moraru, & Sprecher, 2013). The availability of well-defined culture media and advanced culture techniques makes it possible to dissociate individual neurons and generate primary neuronal cultures. Primary neuronal cultures have previously been used for high-resolution imaging of neurite arbors, high-throughput screening of genes for developmental brain disorders, and cell recording of neuronal activity (Campusano, Su, Jiang, Sicaeros, & O'Dowd, 2007; Del Castillo, Muller, &Gelfand, 2020; Perrimon & Mathey-Prevot, 2007). Regardless of which system—*in vivo* or *in vitro*—is chosen, analysis of complex neuron morphologies requires optical resolution below the diffraction limit of light (<250 nm), as the nanoscopic processes of neurons (e.g., dendrites <250 nm in diameter) are of high interest for imaging (Lichtman & Denk, 2011). Super-resolution microscopy techniques provide an excellent solution to this difficulty, improving the resolution beyond the diffraction limit (Huang, Bates, & Zhuang, 2009). Although many techniques have been established for super-resolution imaging of Drosophila samples (Gao et al., 2019; Jiang et al., 2018; McGorty, Kamiyama, & Huang, 2013; Schnorrenberg et al., 2016), stochastic optical reconstruction microscopy, also called STORM, is already widely available and can be used with an extensive array of fluorophores that we have found appropriate for our needs.

In this article, we provide detailed protocols for preparing *Drosophila* neurons and taking STORM images of various structures in the neurons. Basic Protocol 1 describes the establishment of primary neuronal cultures and the dissection of embryos for immunostaining. To label the neuronal membranes genetically, we take advantage of the *UAS-GAL4* system. We start with the appropriate genetic crosses to express membrane markers in particular neurons and train the adults to lay eggs in their new cages. Once we collect the embryos, we can either dissociate the embryos to make a primary neuronal culture or dissect them for in vivo analysis. Finally, we fix the samples before immunostaining, the approach for which can differ depending on the protein of interest (we discuss the difference in Basic Protocol 2). For immunostaining and imaging the samples, it is necessary to choose bright dyes that can overcome reduction of signal due to tissue thickness. In the Support Protocol, we describe a method of dye conjugation to antibodies for the selected far-red dye, which is optimal for STORM imaging. Basic Protocol 2 describes the immunostaining approach for these samples. Although in vivo labeling is a time-intensive process, primary neuronal cultures can be labeled and imaged within a couple of hours. Last, we describe our image acquisition approach in Basic Protocol 3 and our reconstruction approach in Basic Protocol 4. For STORM imaging, a 647-nm laser line is used to photo-switch the fluorophores. In this protocol, it is critical to optimize acquisition settings to obtain a high-resolution image. Finally, we describe our step-by-step approach to reconstructing the STORM data using the ThunderSTORM plug-in in Fiji/ImageJ.

3.3 BASIC PROTOCOL 1: PREPARATION OF DROSOPHILA PRIMARY NEURONAL CULTURE AND EMBRYONIC FILLETS

STORM has been previously demonstrated on primary neuronal cultures from the rat cortex (Xu, Zhong, & Zhuang, 2013), which do not deem any complex sample preparation and imaging steps necessary. As opposed to these cultured cells, STORM imaging of the *Drosophila* nervous system is challenging. Typically, we use a whole embryo for immunofluorescence imaging due to the ease of preparation. However, the surrounding tissues and yolk outside of the nervous system provide background fluorescence. The background fluorescence subsequently degrades the detection and localization of single molecules, resulting in STORM images with fewer localizations and worse resolution. To circumvent this, we dissect the embryos in fillet preparation and remove the intestines and trachea, which contribute to the background fluorescence. Here, we describe our method for culturing and plating primary cells dispersed from *Drosophila* mid- to advanced-gastrula embryos and dissecting late embryonic samples for STORM imaging.

Materials

Embryo collection

UAS-myr::GFP flies (Bloomington Drosophila Stock Center, RRID: BDSC_32197)

elav-GAL4 flies (Bloomington Drosophila Stock Center, RRID: BDSC_8765)

Embryo collection cages fitting 60-mm petri dishes

Yeast paste prepared from active dry yeast by mixing with distilled water

Grape juice agar plates

Egg basket: Create an egg basket by cutting a conical tube horizontally and cutting out a circle from the cap; then place a 100-µm nylon mesh filter between the cap and the tube.

Squirt bottle with distilled water

50% household bleach prepared at 1:1 ratio by mixing in distilled water (stored away from light)

Common materials for culturing neurons and embryo dissection

Dissection microscope (Nikon, SMZ-U)

Dumont #5 Forceps (Fine Science Tools, #11252-20)

Capillary tubing with outer diameter of 1.2 mm and an inner diameter of 0.6 without filament for dissection needle and suction needle

Culturing neurons

Parafilm (Sigma-Aldrich, #P7543)

Task wipers (KimTech, #34155)

60-mm petri dishes (Corning, #430166)

70% ethanol

Coverslip (No. 1.5 thickness, Fisherbrand, #12-541B)

Imaging spacer (Electron Microscopy Sciences, #70327-20S)

Bunsen burner

Concanavalin-A (Con-A; Sigma Aldrich, #C5275-5MG)

Humid chamber (or lidded Tupperware with wet tissue)

Supplemented SFX medium (see **Reagent and Solutions**)

Embryo alignment and dissection

Modeling 'Play-Doh' clay

1 mL syringe (BD, #309659)

Double-sided tape (Scotch, # 665)

Pre-cleaned glass microscope slides 25 × 75 × 1 mm (Fisher Scientific, #S13943) with vinyl tape (Scotch, #6143)

Phosphate-buffered saline (PBS)

Special equipment

Micropipette puller (Narishige PC-100)

Training Flies and Collecting Embryos

1. In an embryo collection cage, cross the *GAL4*-driver flies with the *UAS*-reporter flies at 25°C (**Figure 3.1B**, left).

   Having a ratio of 1:5 male-to-females is sufficient for all of the females to lay eggs. A typical cage containing at least 30–50 adult flies should lay a sufficient number of eggs.

2. Prior to the experiment, acclimate the adult flies to the egg collection cage by allowing them to lay eggs for 1–2 days by changing the yeast-streaked agar plates at least once per day. The

plates should be changed until flies can synchronously lay ~500 eggs per collection period in each plate (**Figure 3.1B**, right).

Keep the cages at 25°C with a humidity of about 65% in a 12-hr light and 12-hr dark cycle to facilitate the collection of synchronous embryos.

3. Allow the adult flies to lay eggs on a yeast-streaked agar plate for 1 hour and collect the plate from the cage and replace with a new yeast-streaked plate.
4. Incubate the plates with the embryos until the appropriate developmental stage. Mid-gastrula embryos aged 5–7 hours AEL (after egg laying) – or Stage 11 (Campos-Ortega, 1985) – are ideal for neuronal culture preparation. By our hands, we found that embryos aged up to 10 hours AEL (i.e., Stage 12) can be plated as well.
5. Remove the eggshell from the embryos by adding 50% bleach to the embryo-containing plate for 5 minutes to allow access to the embryo for cell dissociation and dissection.
6. Filter the eggs through the egg basket (Alternatively, a cell strainer can be used).
7. Wash the filter thoroughly with distilled water so that the embryos are cleared of chorions and yeast from the plate.

   This step is especially critical for cell culture preparation to ensure there will be no contamination by yeast.
8. Disassemble the egg basket and blot the mesh filter dry with sterilized task wipers.
9. Transfer the embryos into a petri dish by flipping the mesh so that the embryos will be facing a clean plate and wash them into the plate set beneath the filter.
10. Pour the water off the embryos just before collecting.

In the last part of this protocol, we report two separate methods for in vitro and in situ sample preparation. In steps 11–20, we describe the preparation of primary cell cultures and through steps 21–30, we describe the preparation of dissected embryos.

Collecting the embryo cell culture

11. Prepare the plates by laying down a strip of parafilm on the bottom of a 60-mm petri dish and covering a section of the plate wall with a damp task wiper. Ensure there is enough room to later lay down the double-sided adhesive imaging spacer (of the appropriate diameter) (**Figure 3.1C**).

    The strip of parafilm beneath should roughly be the size of coverslip/imaging spacer. This allows easier removal of the coverslip/imaging spacer from the plate later.

12. Using forceps, sterilize the coverslip by submerging it in 70% ethanol and drying it completely over the Bunsen burner. Lay the sterilized coverslip on top of the parafilm strip inside the plate.
13. Peel the sticker off one side of the spacer and press the adhesive side, facing down, onto the coverslip. Using forceps, firmly press around the circumference of the spacer. This prevents any leakage of ConA or culture media from the coverslip.

    You may skip this step and instead use vacuum grease to mount the sample as described in BASIC PROTOCOL 2 under “Mounting the immunofluorescence labeled samples.”

14. Spread 10 µL of 0.5 mg/mL Con-A to produce a thin layer on the coverslip. Cover the petri dish with its lid. Place the dish in a humid chamber with humidity ~80%, or a lidded Tupperware with a wet tissue inside. Incubate for 30 minutes at room temperature.
15. Make the supplemented SFX medium (see **REAGENTS AND SOLUTIONS**).

16. Remove the Con-A from the coverslip. Add 100 µL of room temperature supplemented SFX medium on the Con-A-coated coverslip in the plate near the open flame of a Bunsen burner, which provides a sterile environment.
17. Take a dissection needle and break off the tip until the diameter is ~60 µm or about 1/3 of the embryo's width, which can be checked in comparison to the embryos. Connect the needle to one end of the suction tube and add a pipette tip to the other end to act as a suction source. (**Figure 3.1A**)
18. Examine the embryos, directly from step 10, underneath the dissection microscope. Use the pipette tip attached to the tube-connected suction needle (**Figure 3.1A**) to suck and release the contents of the embryo to break the cells out of the vitelline membranes.
19. Transfer the cells from the plate onto the center of the coverslip by gently suctioning in and out with the tube-connected suction needle; make sure any large clumps are broken up. Repeat this process until you have dissociated 20 embryos onto the center of the coverslip.

    To prevent contamination, make sure to always place the lid over the plate of your coverslip.
20. Place the lidded plates into the humid chamber and culture the primary cells for 1–2 days at 28°C.

Aligning and dissecting embryos for in situ preparation

21. On a glass slide, create a dissection pool using vinyl tape and place a piece of double-sided tape inside the dissection pool horizontally to align the embryos as demonstrated in **Figure 3.1D**.
22. Collect the embryos at 13–15 hours AEL, which has the four-chambered gut morphology, (i.e., Stage 16 described by Campos-Ortega), using forceps and place them onto the tape with the dorsal side facing up.

Here we chose to look at Stage 16 as synaptogenesis at the neuromuscular junction occurs during this stage, however, it is possible to dissect and image at older or younger stages as needed.

23. Add PBS to prevent the embryos from desiccating.
24. Using a micropipette puller at 12V, pull the capillary tubing to create a sharp needle with a taper of ~0.4 cm in length to make a dissection needle. Mount the dissection needle onto a 1 mL syringe filled with some modeling clay.
25. Using the dissection needle prepared, cut through the midline of the embryo under a dissection microscope inserting the needle from the surface of posterior end pushing to the anterior end.
26. Gently lift the embryo with the needle which should be slightly underneath the brain lobes of the embryo and pull it up-and-away from the tape.
27. Reposition the dissected embryo onto the glass slide. Here, the embryos should adhere to the glass slide by themselves as long as the buffer is not saturated with proteins and the embryos do not have cuticles.

    Please refer to the Commentary and Troubleshooting for further details.
28. Using the yolk and the intestines that come out as cushion for the dissection needle, place the epithelial tissues to either side on the glass. With this, there should be epithelial tissues on both sides of the ventral nerve cord and the brain.
29. Create another tube-connected suction needle by repeating step 17. To suction the internal organs after dissection, the diameter should be around 300 nm which is about the size of the intestines. Any larger or smaller tip sizes will change the speed of suction.

30. Clean up the sample by using a tube-connected suction needle (**Figure 3.1A**) and blowing air or aspirating to detach and remove the dorsal tracheal trunks and any remaining intestines prior to moving onto immunostaining process.

    If the saline has a lot of tissues or cells floating around, you can replace it by using a micropipette to wash the sample with new saline to ensure the sample is clear of debris.

3.4 BASIC PROTOCOL 2: IMMUNOFLUORESCENCE LABELING OF SAMPLES

For immunofluorescence labeling of samples, there are a couple of considerations necessary to obtain the best quality of STORM images. One important consideration is the fixation approach applied to the samples. As a result of insufficient fixation, membrane structures and macromolecule architectures can be broken. In order to avoid this type of artifact, different cellular targets have been optimized to be fixed with certain fixatives. For instance, glutaraldehyde (GA)-based fixation for tubulin is optimal in preserving the microtubule structures, while fixation with paraformaldehyde (PFA) alone is sufficient for preserving membrane structures. Because of its high resolution, STORM can readily uncover such disruptions. Therefore, the choice of proper fixatives is crucial. Next, the density of fluorescent labels should also be considered. When immunostaining membrane structures with a membrane marker, the low density of the marker makes a STORM image discontinuous. With this inadequate labeling density, it is not easy to evaluate whether the structures are related. Here, we describe our method for fixing, immunostaining, and mounting the neuronal culture and brain tissues.

Materials

Drosophila primary culture on coverslip or dissected embryos on glass slide

Phosphate-buffered saline (PBS)

4% Paraformaldehyde (PFA; Electron Microscopy Sciences, #15710) in PBS.

0.1% Glutaraldehyde (GA; Sigma Aldrich, #111-30-8) in PBS.

PBS with 0.1% Triton-X100 (TBS)

0.1% TBS + 0.06% bovine serum albumin (BSA) (TBSB)

Primary antibodies

- 1:200 anti-GFP rabbit monoclonal antibody diluted in TBSB (ThermoFisher, #G10362, RRID: AB_2536526)
- 1:200 DM1A anti-tubulin antibody: (Cell Signaling Technology #3873, RRID: AB_1904178)
- 1:5 anti-HRP antibody: (JacksonImmuno, #123-005-021, RRID: AB_2338952)

Secondary antibodies

- 1:200 anti-rabbit IgG secondary antibody conjugated with AF647 dye (see SUPPORTING PROTOCOL for dye to antibody conjugation) diluted in TBSB

Aspirator (Bio-Rad, Model #1651754P)

Orbital Shaker (CB, KJ-201BD)

Imaging medium (see Reagents and Solutions)

Clean coverslip No. 1.5 thickness (Fisherbrand, #12-541B)

Pre-cleaned glass microscope slides 25 × 75 × 1 mm (Fisher Scientific, #S13943)

Vacuum grease or some other spacer to cushion between the coverslip and the tissues (e.g., Secure Seal Imaging Spacer from Electron Microscopy Sciences, #70327-20S)

Task wipers (KimTech #34155)

Nail polish for sealing the sample

Permeabilization and Staining

1. Using an aspirator, remove the culture medium or saline buffer and replace with 4% PFA in PBS for membrane labeling and with 3% PFA+ 0.1% GA in PBS for microtubule labeling.
2. Incubate on an orbital shaker to fix for 5 minutes at room temperature.

3. Then, wash for 5 minutes each with TBS, 3 times.
4. Block the sample for 10 minutes for cell culture (or 1 hour for dissected embryos) at room temperature using TBSB to reduce/eliminate non-specific binding of primary and secondary antibodies.
5. Exchange the TBSB buffer with the primary antibody in TBSB. Please see the Critical Parameters section under Commentary for our discussion of advantages and disadvantages of using labeled primary antibodies and indirect labeling with secondary antibodies.

   For primary neuronal culture samples, incubate the primary antibody for at least 1 hour at room temperature.

   For dissected embryo samples, incubate the primary antibody overnight at 4°C.
6. Before staining samples with secondary antibody, remove the primary antibody and wash with TBSB for 5 minutes each, 3 times.
7. Dilute the secondary antibody IgG conjugated with AF647 dye to a working concentration in TBSB.
8. Exchange the blocking buffer with the secondary antibody using an aspirator. Ensure that the samples are not dried out during this exchange process.
9. Stain the sample by incubating at room temperature on the orbital shaker.

   For primary neuronal culture samples, incubate the secondary antibody for 1–2 hours.

   For dissected embryo samples, incubate the secondary antibody for 2 hours.
10. Wash the sample with TBS for 5 minutes each, 3 times.
11. Post-fix the sample using the 4% PFA in PBS for 5 minutes at room temperature to crosslink the antibodies strongly and to eliminate floating dyes, which can contribute to creating background signal.

12. Finally, wash with TBS 3 times to remove the fixative from the sample.

Mounting the immunofluorescence labeled samples

13. Using task wipers or an aspirator, remove excess buffer from the sample but ensure the samples do not dry out.

    In case of the in-vivo preparation, remove the tapes that are on the glass slide using forceps first.

14. Exchange the buffer with 100 μL imaging medium.

    Make sure to use as much imaging medium as possible to prevent any large air bubbles from forming in the next step.

15. Mount the coverslip onto the glass slide.
    - *To mount the cells*: Remove the remaining sticker from the spacer and place the glass slide on top of the spacer and make sure it is completely sealed.
      Alternatively, apply vacuum grease to each corner of the coverslip then place the glass slide on the coverslip.
    - *To mount the embryos*: Place the coverslip on the glass slide and push it down to minimize the space between the coverslip and the sample until it touches the CNS.
      This will allow for maximum brightness of fluorophores while imaging for the tissue sample.

16. Remove the excess buffer that has leaked out and seal the edges of the coverslip with nail polish and image or incubate at 4°C until imaging.

    It is ideal if the sample is imaged within 3 hours after mounted in buffer under minimal oxidation conditions for optimal results.

3.5 BASIC PROTOCOL 3: SINGLE MOLECULE FLUORESCENCE IMAGING

In this section, we describe the equipment and steps required for successfully acquiring raw single-molecule data. Although we use a custom-built STORM imaging system for the acquisition (**Figure 3.2**), one can adopt any of the commercial systems currently available, e.g., N-STORM (Nikon).

Materials

Immersion oil (n=1.52) (Cargille, #16242)

Lens paper (Thorlabs, MC-5)

Microscopy Setup

Custom-built inverted microscope (see also **Figure 3.2B**)

Light source

405-nm excitation laser (Coherent, OBIS 405 nm LX 100 mW)

561-nm excitation laser (Coherent, OBIS 561 nm LS 50 mW)

647-nm excitation laser (Coherent, OBIS 647 nm LX 120 mW)

Laser control unit

- Arduino Uno
- Micro-manager Arduino software (https://micro-manager.org/wiki/Arduino)

Spectral filters

- Excitation laser clean-up filters: 516 nm (Semrock, LL02-561-12.5) 647 nm (Semrock, LL02-647-12.5)
- Dichroic mirror (Omega, XF2054,485-555-650TBDR)
- Emission filters: Multi-bandpass (Semrock, FF01-446/523/600/677-25)
  Red detection (Semrock, FF01-605/15)
  Far-red detection (Semrock, FF01-680/42)
- Notch Filters: Red detection (Chroma, ZET561NF)
  Far-red detection (Semrock, NF01-488/64)

60X Oil Objective lens (Plan Apo N, Olympus, N.A. 1.42)

EMCCD camera (Andor, iXon-897 Life)

Image acquisition software (μManager 2.0, RRID:SCR_016865)

Computer workstation (Intel Xeon CPU ES-1603 v4, 2.80 GHz, 16GB RAM) with a 500GB solid-state hard drive

Optimizing image acquisition for cell culture and whole mount immunofluorescence

1. At least 30 minutes prior to imaging, turn on the lasers and camera to allow components to reach a stable operating state.
2. Clean the objective with lens paper.
3. Launch image acquisition software (μManager 2.0) and let the camera temperature stabilize (−70°C for Andor iXon897).
4. Place a drop of immersion oil on the objective lens and place the glass-slide containing the sample in the sample holder with the coverslip facing downwards.
5. Set camera exposure and use a white light source to bring the sample to focus.
   Typical setting for the exposure of an EMCCD camera is 10 ms.
6. Record a single image using the 647 nm laser at an area on the sample where there are no cells. These images can be used to subtract the background later from the raw single molecule data of the respective channels.
7. Using a 647 nm laser record a wide-field image of the cell with low laser power of 1 mW and short exposure time of 10–20 ms.
8. Using the 647 nm laser, start the STORM imaging acquisition using empirically derived camera and laser settings. We derived these settings by inversely adjusting the exposure time and the laser power until the fluorophore emission events are far enough from each other (sparsely distributed) to be individually identified (**Figure 3.3A**, top panel). Our

typical settings for laser power and exposure time at the beginning of acquisition were 15 ms exposure time and laser power of 30 mW. The frame transfer mode is set to off in order to reduce noise, and the EM gain is set to 500. These settings can be found in Micromanager under Devices → Device Property Browser corresponding to each connected device (i.e., camera and lasers).

We can typically collect at least 40,000 images using the AF647 dye with these settings. The number of images to collect (i.e., count under 'Time Points') is set in the Micromanager acquisition menu with an interval of 0 seconds.

9. Turn on the 405 nm laser and let it illuminate the sample in continuous wave (CW) mode to facilitate regeneration of the fluorescent dye molecules.

   At the beginning of the acquisition set the 405 nm laser power to the lowest possible setting (1mW). Increase the laser power of the 405 nm laser about 5 mW every 5,000 frames as the acquisition time increases to record the maximum number of images until all dyes cease to photo-switch. The laser power might increase to 20 mW or more. The laser power is set in the Micromanager Device Property Browser and can be adjusted manually during acquisition. The two lasers are controlled by the laser control unit.

10. After the acquisition ends, the images are available as an image stack in a file in .tiff format. This file can then be opened in ImageJ or other image processing software for analysis.

3.6 BASIC PROTOCOL 4: LOCALIZATION AND VISUALIZATION OF SINGLE MOLECULE DATA

In STORM, an algorithm is used to precisely measure the positions of single molecules from raw camera frames. The algorithm has a fundamental effect on the resolution and fidelity of the final rendered STORM image. The entire process involved in the rendering of a STORM image can be divided into five steps: detecting single molecules from raw camera frames, fitting and localizing the detected molecules, processing the positions of these molecules (e.g., drift correction, density filtering, and intensity thresholding), rendering the final image of the molecular localizations, and finally statistically analyzing these localizations. Many software packages have been developed and published to help non-expert users perform these steps efficiently. Our protocol below gives a brief description of how to choose the critical parameters for image reconstruction using ThunderSTORM (Ovesny, Krizek, Borkovec, Svindrych, & Hagen, 2014), an open-source plug-in for ImageJ. We note that the selected parameters and options described in this protocol are not the only choices. Users need to refer to the manual for a detailed guide to select the proper parameters based on their demands.

Materials

Fiji/ImageJ software (RRID:SCR_002285)

Software for localizing and visualizing single molecules data (e.g., ThunderSTORM, RRID:SCR_016897; use version phasor-intensity-1) (Martens, Bader, Baas, Rieger, & Hohlbein, 2018)

Localization of single molecule data

1. Drag and drop the data file collected using 647 nm laser from the file explorer to ImageJ, or select File → Open in ImageJ, browse to the data file and press Open. This will load the entire image stack into memory.
2. Open the dark frame recorded using the 647 nm laser as mentioned in step 1 in Basic Protocol 3. Using Process → Image Calculator, subtract the dark frame from the dataset to remove the background (**Figure 3.3A**).

3. Set the camera pixel size in the sample plane, conversion factor between photons and digital units, base level offset of the camera digitizer, and EM gain of the camera using Plugins → ThunderSTORM → Camera setup. For our setup, the pixel size is 107nm, the gain is 500, and the conversion factor is 4.83 photons / ADU. The conversion factor and offset are specific to the camera and camera settings and can be found in the documentation that came with your camera.
4. Analog-to-digital units (ADU) are the integer values the camera uses to record intensity. The analog-to-digital converter (ADC) converts the electrons recorded in each pixel into a digital signal measured in ADUs, which is used to quantify the incident number of photons per pixel.
5. After opening the dataset, select Plugins → ThunderSTORM → Run analysis. Select the Wavelet filter (order 3, scale 2) to perform band-pass filtering on the dataset (**Figure 3.3B**).
6. Under the Approximate localization of molecules tab, select Local Maximum for Method and choose a peak intensity threshold between 0.5 to 2 times the standard deviation of the 1st wavelet level, e.g., 1*std (Wave.F1). If the threshold is set too low, some additional peaks are identified due to noise. If the threshold is set too high, then some of the true fluorophores are missed.
7. Select Phasor-based localization 2D as the method for sub-pixel localization of the single molecules with the fit radius being an integer number close to 3*sigma (**Figure 3.3C**).
8. The initial size of sigma can be found by running ThunderSTORM on few images of the data sequence. A histogram of the fitted sizes of sigma (in pixels) can help to find the initial value.

9. The localized data can be visualized using averaged shifted histograms, with a magnification of 20 and 4 lateral shifts. Once the parameters for localization and visualization have been set, press OK (**Figure 3.4A**).
10. The order of post-processing steps is user-specified. However, we recommend the following order: filtering, density filtering (to remove outliers) and finally drift correction. Typically, we will use the filtering step to remove localizations from the first frames of the acquisition when too many fluorophores are emitting. Density filtering is used to remove localizations from unattached, isolated fluorophores that do not label the structure of interest (**Figure 3.4B**). Drift correction accounts for movement of the sample during the acquisition process.
11. Drift correction by cross-correlation can be performed by clicking the drift correction tab (**Figure 3.4C**). Typical settings for the parameters are 5 bins, 5x magnification, and 1.0 for trajectory smoothing. Cross-correlation images with detected peaks can be viewed by checking the "Show cross-correlations" checkbox to fine tune the parameters for different datasets. As shown in **Figure 3.4C**, successful drift correction results in an image with higher resolution and less blurring. Compare the image before drift correction (the middle panel in **Figure 3.4C**) to the image after drift correction (the right panel in **Figure 3.4C**).
12. The output of this process is the table of filtered and corrected localizations and the final super-resolution figure.

3.7 SUPPORTING PROTOCOL: CONJUGATION OF ANTIBODIES WITH STORM COMPATIBLE DYES

STORM images are constructed based on single-molecule imaging of photo-switchable fluorescent probes. Compared to labeling for epi-fluorescence imaging, a single fluorophore emits a weak signal, which makes its detection challenging. Additionally, tissue-induced spherical aberration and light scattering cause a further loss of fluorescence signal and thus degrade localization precision (Kamiyama & Huang, 2012). Various bright probes, including organic dyes and quantum dots, have previously been characterized to circumvent this problem. Among those probes, Alexa Fluor 647 (AF647; a far-red photo-switchable dye) is exceptionally bright, producing high-quality images of central nervous system (CNS) neurons (Dempsey, Vaughan, Chen, Bates, & Zhuang, 2011). Here, we demonstrate the conjugation of AF647 to antibodies.

Materials

Illustra Nap™-5 columns, (20 Columns, 0.5 mL) (Cytiva, #17-0853-01)

1 M $NaHCO_3$ prepared from powder (JT Baker, #3506-01)

Anti-rabbit IgG (JacksonImmuno, #711-001-003, RRID: AB_2340584)

Anti-mouse IgG (JacksonImmuno, #115-001-003, RRID: AB_2338443)

Anti-HRP (JacksonImmuno, #123-005-021, RRID: AB_2338952)

1.5 mL Eppendorf tubes (for conjugation mixture and for collecting product fractions)

Phosphate-buffered saline (PBS)

Alexa Fluor™ 647 NHS Ester (ThermoFisher, #A20006; or any other STORM compatible dye)

Dimethyl sulfoxide (DMSO; Sigma Aldrich, #276855)

Aluminum foil

Nutator (BD Clay Adams™ Nutator Mixer, BD Diagnostics)

Micropipettes (Gilson, SKU #F167380)

Conjugating the primary and secondary antibody with STORM compatible dye

1. For anti-HRP conjugation in an Eppendorf tube, add:
    a. 60 μL of anti-HRP

    b. 20 μL of 1x PBS
    c. 10 μL of 1 M $NaHCO_3$
    d. 1 μL of AF647 dye dissolved in 10 μL DMSO
2. For secondary antibody conjugation in an Eppendorf tube, add:
    a. 20 μL of secondary antibody
    b. 60 μL of 1x PBS, 10 μL of 1M $NaHCO_3$
    c. 6 μL (for anti-rabbit IgG) or 3 μL (for anti-mouse IgG) of AF647 dye dissolved in 10 μL DMSO.

    The amount of antibody or dye may not always provide the same degree of labeling conditions. These amounts may change depending on the conditions of the ingredients.
3. Cover the tube with aluminum foil to protect from light.
4. Incubate at room temperature for 15 minutes on a nutator to allow for reaction to take place.
5. During the reaction, wash the Sephadex column at 4°C with PBS 3 times to equilibrate the resin pores with PBS and drain the PBS from the column.
6. After the reaction is finished, add the reaction mixture to the column slowly with a micropipette.
7. Once the mixture has set into the resin, elute with 400 μL of PBS. In AF647 conjugation, we can see two bands forming; the lower band is the conjugated dye, and the upper band is the unconjugated dyes.
8. Collect the product in 100 μL increments by adding PBS and eluting into different tubes. By looking at the color, we can tell the best conjugated fraction. Typically, the most dye concentrated fractions in the middle– i.e., fractions 3 or 4– are the best conjugated fractions.

To find the degree of labeling we can use UV/Vis absorption measurements.

Using the molar extinction coefficients and the absorptions of dyes at 280 nm, calculate the degree of labeling. The number of dye molecules per antibody (DOL) should be between 1–2 for STORM, and in case of quantitative studies, DOL closer to 1 is ideal.

9. Store the antibodies at 4 °C for up to 1 month or aliquot the antibodies into small tubes and store them at −20°C for up to 1 year.

3.8 REAGENTS AND SOLUTIONS

Supplemented SFX Medium

Prepare the medium in the cell culture hood. When handling the medium afterwards (such as preparing plates), work near the Bunsen burner to avoid bacterial contamination. Use deionized, distilled water in all steps and recipes unless otherwise specified.

To 9.4 mL HyClone SFX-Insect cell culture media (Cytiva, #SH30278.02), add:

- 400 μL fetal bovine serum (R&D Systems, #S11150)
- 100 μL Penicillin-Streptomycin (100X) (R&D Systems, #B21110)
- 100 μL Gibco Insulin-Transferrin-Selenium (Thermo-Fisher, #41400045)
- Aliquot into 200 μL fractions.
- Store up to 12 months at 4°C.

Imaging medium

β-mercaptoethanol is toxic if inhaled; therefore, it is critical to keep it in a well-ventilated area and use a fume hood when making the imaging medium.

- 80 μL PBS
- 20 μL 50% Glucose (w/v)
- 1μL β-mercaptoethanol (Sigma Aldrich, #M3148)

- 1 µL Glucose oxidase with catalase: Prepared by dissolving 1 mg of glucose oxidase in 10 µL PBS (100 mg/mL, Sigma Aldrich, #G2133) and adding 2 µL of catalase (17 mg/mL, Sigma Aldrich, #C40) solution.

Typically, when preparing this buffer, we add the catalase to the glucose oxidase solution. This way, we can store the catalase aliquot of 17 mg/ml in −20°C for multiple uses in the future. This buffer should be switched out after 3 freeze-thaw cycles. Glucose oxidase with catalase has a much shorter lifespan in 4°C, which should be prepared freshly after 3–4 days.

COMMENTARY

3.9 BACKGROUND INFORMATION

Cultured *Drosophila* neurons have been used for investigating the cytoskeletal dynamics in neurons, conducting comparative analysis studies with *in vivo* experiments, carrying genetic RNAi screening (Mohr, Bakal, & Perrimon, 2010), and identifying cell-autonomous neuronal mechanisms such as membrane compartmentalization or presynaptic differentiation (Katsuki, Ailani, Hiramoto, & Hiromi, 2009). Although such *in vitro* approaches play an important role in revealing cellular phenotypes, developmental and functional findings are crucial for understanding neural circuitry development. To investigate the underlying mechanisms, we use embryonic motoneurons in vivo (Furrer, Vasenkova, Kamiyama, Rosado, & Chiba, 2007; Kamiyama & Chiba, 2009; Kamiyama et al., 2015; Sharifai et al., 2014). This system is amenable to targeted genetic manipulation in a cell-type-specific manner, allowing us to study neural specification, axon and dendritic guidance, partner selection, and synaptogenesis. In furthering our understanding of synaptogenesis, the neuromuscular junction serves as an excellent model system due to the stereotypical motoneuron targeting (Keshishian et al., 1996b). For partner recognition to result in a mature synapse, the neuronal growth cone must interact with the muscle through actin-based hairlike structures found in both cells (Ritzenthaler et al., 2000). These fine structures, called filopodia, explore the local environments to match partner cells together (**Figure 3.5**). While some developmental time points have been identified, the nature of the filopodial interactions remains elusive because of their fine structures. However, the protocol described here can be further applied to labeling the neuromuscular junction and applying dual-color STORM, so the details of the filopodial interactions can be further investigated.

Here, we demonstrate STORM, which utilizes photo-switchable organic fluorescent dyes to precisely localize individual molecules. Unlike conventional light microscopy, STORM can achieve resolutions of ~20 nm laterally and ~50 nm axially (Huang et al., 2009). There are numerous examples in which STORM has been applied to biological research (Kamiyama & Huang, 2012). In particular, STORM is a valuable asset to conduct anatomical studies of filopodia. Because the filopodia are so tiny (~200 nm in width and ~5 μm in length), their architecture can be characterized through STORM. Furthermore, we believe that multicolor STORM allows us to visualize filopodia between the motoneuron and the muscle (as demonstrated by confocal microscopy; **Figure 3.5**). For this purpose, we have evaluated many organic dyes at different emissions (M.A.I., and D.K., unpublished data). Although the dyes are photo-switchable under specific buffer conditions, Alexa Fluor 647 exhibits the best photo-switching ability. As an alternative to the STORM technique, multiple groups have recently developed a new approach, called DNA-PAINT (points accumulation for imaging nanoscale topography) (Jungmann et al., 2010, 2014). DNA-PAINT is compatible with the imaging platform of standard STORM. This approach takes advantage of DNA specificity for target recognition using a docking strand of DNA conjugated to an antibody and an imager strand of DNA conjugated to a fluorescent dye. Contrary to the traditional STORM technique, the blinking effect is achieved by the transient binding of these DNA strands. We can apply different orthogonal docking sequences with unique fluorophores to the same sample, which allows the observation of multiple proteins. This approach also has the potential for multicolor imaging of *Drosophila* tissues.

3.10 CRITICAL PARAMETERS

Primary neuronal culture:

To set up for a healthy neuronal culture, adult flies in the mating cage should not be older than one week. This ensures healthy embryos to begin plating neurons. Plating an appropriate density of cells (~1.2×105 cells/cm^2; see also **Figure 3.6**) is key to axonal growth, secured adhesion to the coverslip, and reduced clustering and layering. However, the researcher should keep in mind that a cell density too low may risk the survival of the neurons.

Tissue preparation:

For embryonic dissection, selection of the developmental age is important (Inal et al., 2020). Beyond the age of ~15 hours after embryo laying, the embryos will start depositing cuticles which will prevent the embryos from sticking to the glass slide. While older embryos can also be dissected, the method described here may not be compatible for those experiments. In addition, the number of embryos that can be dissected and placed onto the glass slide becomes limited as the amount of protein in the buffer will be saturated and coat the glass preventing any more embryos from sticking to the slide. When washing the embryos after dissection in the subsequent steps of the protocol, care should be taken to prevent embryos from lifting off the slide or being destroyed due to surface tension.

Fixation:

We usually fix cellular proteins with 4% paraformaldehyde. In contrast, we use the mixed concentration of paraformaldehyde and glutaraldehyde to preserve microtubule structures (Kamiyama & Huang, 2012). To maintain cells in their most natural state, we optimize a fixation approach for the structure of interest. The optimal fixative for the ideal image should be best for preserving the target structure while avoiding structural artifacts.

Immunostaining:

Since the quality of a STORM image depends on labeling density, the immunostaining needs to provide the best labeling density for taking the best image. To achieve this, antibody concentrations higher than the recommended should be used. Additionally, longer incubation times allow for more effective labeling. Therefore, if possible, the primary antibody should be incubated overnight at 4°C and secondary antibody for ~1–2 hours at room temperature. Selecting antibodies that are highly specific for the antigens will minimize nonspecific labeling and background signals. Furthermore, it may be helpful to use primary antibodies that are directly conjugated with the fluorophore to minimize linkage error which results in increased apparent size of structures (Huang et al., 2009).

Antibody conjugation:

The degree of antibody labeling should be between 1–2 for STORM imaging, and this can be measured using a spectrophotometer with the given calculation approach in the methods. The conjugation from one batch to another may not give the same DOL and even within the same batch, the labeling efficiency may vary. In this case, it is advisable to collect the conjugated mixture in smaller (~100 µL) fractions.

Mounting/Imaging buffer:

During long imaging processes the pH value of the buffer decreases as oxygen reacts with the oxygen scavenging component of the imaging buffer. This event can hinder the photo-switching abilities of the fluorophore. Therefore, the freshest buffer should be used and the oxygen concentration in the buffer should be minimized by sealing the sample which can improve the lifespan of imaging buffer. Additionally, the fluorophores may lose photon counts if the sample is far away from the cover-glass. Therefore, the mounting approach, especially for tissues, should minimize the distance between the sample and the cover-glass (Dani, Huang, Bergan, Dulac, & Zhuang, 2010). This will evidently increase the photon counts and resolution.

Acquisition:

The resolution of an image acquired using STORM is inversely proportional to the number of photons emitted by a single molecule (Huang et al., 2009). Apart from the freshness of the imaging buffer and the quality of the dye, the laser power with which the dye is excited plays a vital role in determining the number of photons emitted by the dye. Every dye has a maximum number of photons that it can emit (Dempsey et al., 2011), and the number of photons emitted by a dye is linearly related to the laser power until it reaches the maximum number of photons emitted at which point the dye is saturated and the number of photons emitted remains constant at the maximum. Therefore, to achieve the best acquisition, it is important to excite the sample with the appropriate laser power sufficient to facilitate blinking but not too high that one bleaches the dye too fast.

3.11 TROUBLESHOOTING

Protocol	**Problem**	**Possible Cause**	**Solution**
Sample preparation	Poor neuronal growth/differentiation	• Suboptimal temperature incubation	• Incubate cell culture at a higher

			temperature (e.g., 28 °C)
	Embryo does not stick to glass slide	- Unclean glass slide - Embryo cuticles	- Use clean glass slide - Use younger embryos for dissection
	Embryo is floating or destroyed	- Sample is exposed to meniscus of the buffer	- When exchanging buffers use large volumes for washes to ensure sample remains entirely covered to prevent drying
	Cells are dispersing or floating	- Pressure from the objective lens forcing the cells to float if the buffer leaks out	- Make sure the coverslip perimeter is well-coated and dried in nail polish - Adjust the objective lens to make sure it does not compress the coverslip - Minimize the distance between coverslip and the slide which will increase the working distance for the objective lens
	Filopodia are moving	- Poor fixation	- Increase the length of fixation or the concentration of the fixative
	Poor signal and/or high background	- Non-specific labeling - Large distance from sample to coverslip	- Use highly specific antibodies - Increase antibody concentration - Use blocking buffer/increase blocking time - Minimize distance from the coverslip by pressing the coverslip down. If it is not being imaged,

			the ventral nerve cord can also be removed via suctioning after fixation
	Inconsistent labeling efficiency	• Variable antibody degree of labeling	• Collect conjugates in smaller fractions and test degree of labeling
Acquisition	Low photon count from fluorophores	• Excitation laser is not aligned perfectly through the objective lens. • Reflectivity of mirrors in excitation path is low causing loss of laser power before reaching sample	• Re-align the system • Measure reflectivity of mirrors in the excitation pathway and change mirrors accordingly. We recommend the use of dielectric mirrors for the highest reflectivities.
	Fluorophores are not turning off/blinking	• Low laser power • Buffer is not fresh	• Increase the laser power until blinking can be observed • Make sure the enzymes (glucose oxidase and catalase) in the imaging buffer are freshly prepared • Imaging buffer has an expiration after 2–3 hours
	Fluorophores are not turning on	• Fluorophore is photobleached • Buffer is not fresh	• Alternatively use an activation laser such as UV (405 nm) and increase its laser power See above about imaging buffer.
Post-processing	Axons appear blurry once reconstructed	Lateral or optical drift	• Ensure the stage is stabilized prior to acquisition • Perform drift correction on reconstructed image

	Reconstructed image has too many localizations	Inaccurate intensity thresholding	- Filter out unwanted molecules by changing the intensity threshold

3.12 UNDERSTANDING RESULTS

Reconstruction of super-resolution images acquired via STORM

We must consider for reconstruction, the parameters such as background intensity levels and the Min/Max values in selecting individual blinking events to achieve the highest resolution without compromising the quality of the reconstructed image. In BASIC PROTOCOL 4 (see also **Figures 3.3** and **3.4**), we show our workflow to identify the optimal parameters for our samples. These parameters can vary between setups, sample types (culture neuron vs. in vivo neuron) and even individual acquisition samples. Although there is not a one-size-fits-all approach, the variability among acquisition samples is not significantly different to require testing many different parameters each time. Therefore, the results of reconstruction should be easily reproducible among multiple samples.

STORM imaging of in vitro and in vivo neurons

We show a conventional widefield image of a neuron in culture (**Figure 3.6**) and the reconstruction of the same neuron using STORM imaging (**Figure 3.7**). With the protocol we describe here, we can image not only the membranes of the neuronal cells in culture but also the cytoskeletal architecture of them. In **Figure 3.7A**, we show images of the microtubules acquired from primary neuronal cultures. As the inset indicates, we can clearly see each microtubule bundle, compared to the inset of the widefield image. In **Figure 3.7B and C**, we show different approaches to label the neuronal membrane using anti-HRP (pan-neuronal membrane marker) or anti-GFP (expressed on the cell membrane through *UAS-GAL4* system) antibodies. And in **Figure 3.7D** we demonstrate that we can also use photoconvertible fluorescent proteins such as tdEos to image the membrane structures of the neurons. Using similar labeling approaches, we also apply these tools to in vivo neuronal imaging. We demonstrate in **Figure 3.8A**, the neurons labeled with the anti-HRP antibody and also in **Figure 3.8B**, labeled with the *UAS-GAL4* system and immunostained against GFP with the AF647 dye.

While we demonstrate a limited set of examples for using these tools, other proteins can also be imaged with this method using STORM to individually localize and elucidate their cellular roles at resolutions of ~20 nm. Additionally, other photo-switchable dyes or fluorescent proteins can be used to look at cellular or molecular interactions in multi-color STORM imaging.

3.13 TIME CONSIDERATIONS

Flies need to be trained for 2 days prior to primary culture and embryonic sample preparations. The culturing step for primary neurons takes an additional ~2 days for neuronal morphology to differentiate before immunostaining. On the other hand, the embryos can be collected immediately following the 2-day training period and dissected. Dissection of embryos can take as little as 5 minutes for 10 embryos for an experienced individual. A beginner may take 5 minutes or longer for dissecting a single embryo at first. Depending on the efficiency of the individual the number of embryos to be dissected can be modified especially for developmentally time sensitive experiments. After the fixation step which takes 5 minutes, permeabilization and blocking take around 1 hour and 15 minutes. This is a good point for pausing, if necessary. This is also a good time to prepare dye-conjugated antibodies which can be stored for subsequent experiments. For indirect labeling, primary antibody incubation takes place overnight and secondary antibody incubation takes 2 hours. In case of direct labeling incubation takes maximum 2 hours at room temperature. The subsequent washing steps and post-fixation should take ~25 minutes.

The image acquisition is controlled by µManager running on a Dell workstation (Intel Xeon CPU ES-1603 v4, 2.80 GHz, 16GB RAM) with a 500GB solid-state hard drive. Acquiring 40,000 raw frames with a 15ms exposure time takes about 15 minutes. On the same computer, the analysis can take up to 20 minutes depending on the number of localizations that are found and the analysis steps that are used. Opening the acquired data takes 5 minutes. The image stack is then analyzed as described in BASIC PROTOCOL 4. Running the analysis in Thunderstorm takes 3 to 4 minutes. Running the density filter take 3–4 minutes, and if drift correction is performed that will take an additional 5 minutes. The post-processing steps must typically be run a few times to optimize the parameters in order to generate an optimal final image.

3.14 FIGURES

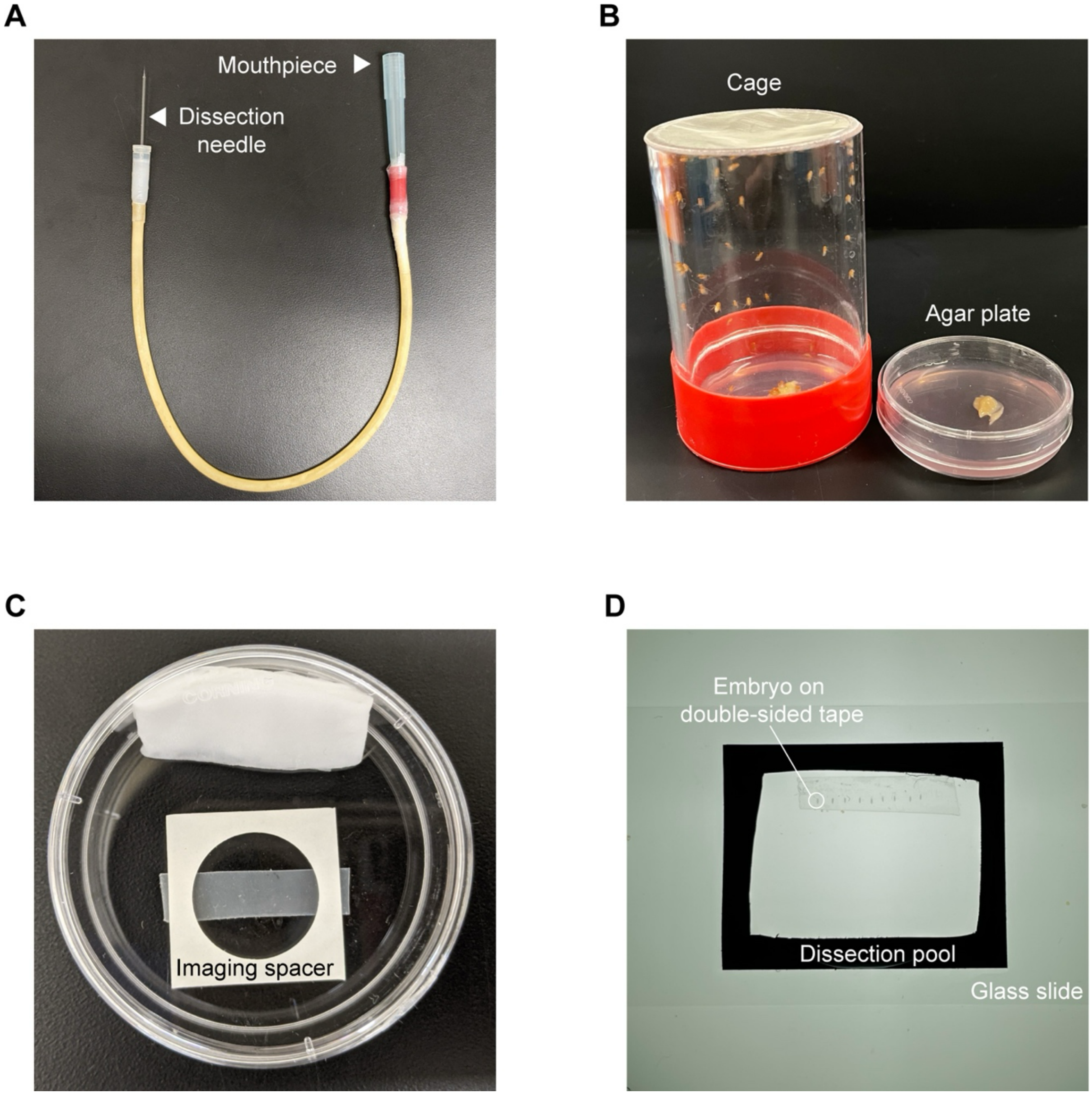

Figure 3.1 Equipment for sample preparation.

(A) Tube-connected suction needle. A pipette tip (blue) attached to the tube is used as the mouthpiece (arrowhead). At the other end of the tube, a dissection needle attaches to an adaptor piece (arrowhead). **(B)** Embryo collection cage with a mesh top and yeast-streaked plate. The yeast-streaked agar plate is used by flies to lay eggs. **(C)** Coverslip preparation inside a humid chamber. The double-sided adhesive imaging spacer overlays the coverslip. Cells should be plated inside the well chamber. **(D)** Glass slide preparation with a dissection pool for dissecting the embryos. The embryos (e.g., encircled) are aligned onto a piece of double-sided tape and submerged in saline. The dissection pool is created from vinyl tape on a clean glass slide.

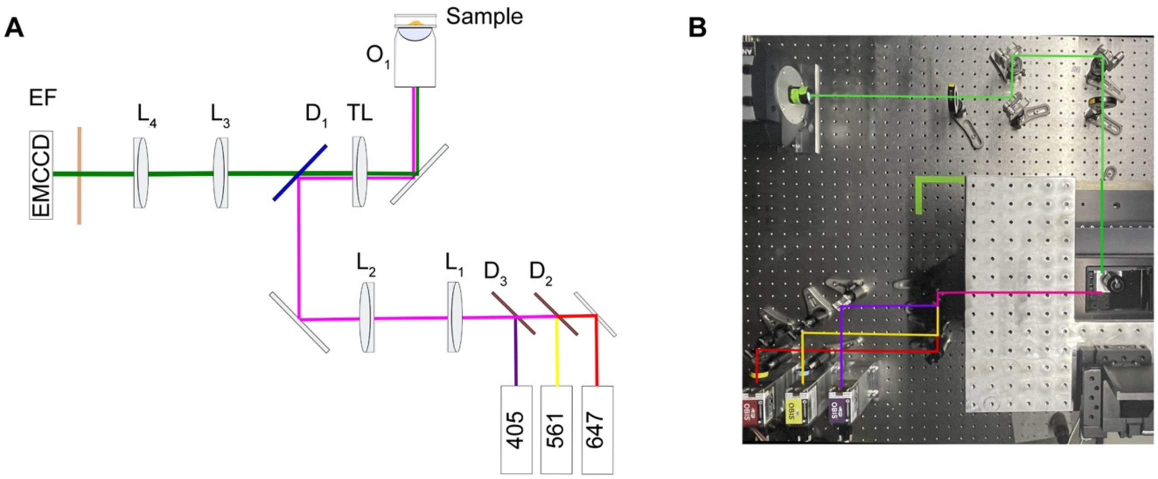

Figure 3.2 Microscopy setup.

(A) Schematic of the single molecule localization microscope. Three lasers at Wavelengths 647nm (Coherent, OBIS LX 647-120mW), 561nm (Coherent, OBIS LS 561-50mW), and 405nm (Coherent, OBIS LX 405-100mW), are combined with Dichroics D2 (Thorlabs DMLP605T) and D3 (Thorlabs, DMLP425T). Laser Line filters are used to filter out spontaneous emission for the 647 laser (Semrock, LL02-657-12.5) and the 561 laser (Semrock, LL02-561-12.5). Lenses L2 (Newport, PAC052; efl=100mm) and L3 (Opto-Sigma, 026-1132; efl=120.1mm) expand the laser beams to a diameter (1/e2) of 0.96mm. The excitation beams are then demagnified by 60x by the tube lens, TL (Olympus, 180mm) and the objective lens, O1 (Olympus 60x) to a beam diameter of 16 µm. The emitted light is separated from the excitation light by the dichroic D1 (Omega Optical, XF2054, 485-555-650 TBDR). The emission from the sample is imaged on to the EMCCD Camera (Andor, Ixon-897 Life) first to 60x magnification by the objective lens O1 and the tube lens TL and then by an additional 2.5x by lenses L3 (120 mm) and L4 (300 mm) for a total magnification of 150. The camera pixel size is 16 µm so the effective pixel size at the sample is 107 nm. Two emission filters (Semrock, FF01-446/523/600/677-25 and FF01-680/42) and a notch filter (Semrock, NF01-488/647) are placed before the camera to block excitation and stray light. **(B)** Photograph of the system. The excitation paths and emission path are traced in red, yellow, purple, and green respectively.

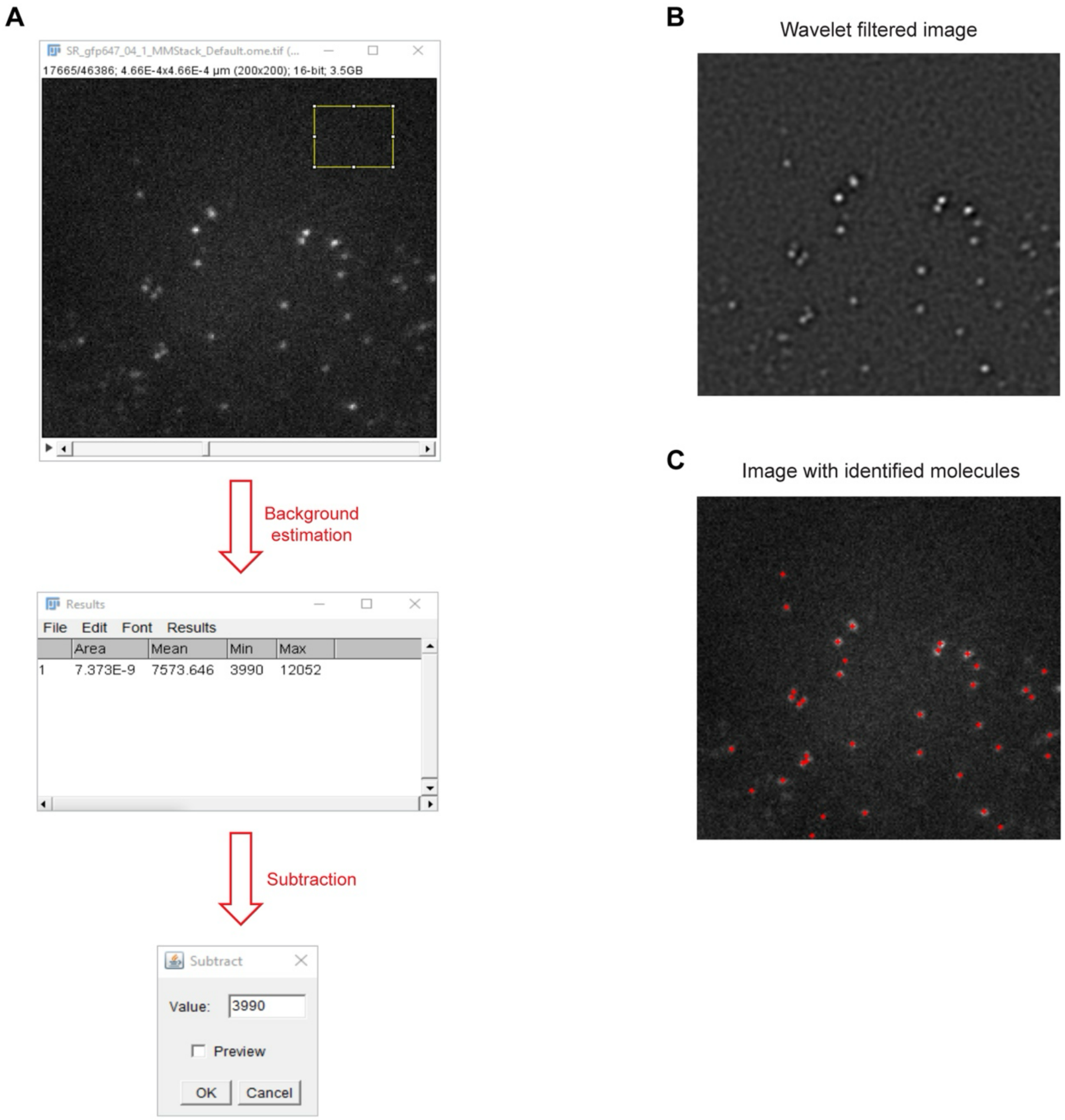

17665/46386; 4.66E-4x4.66E-4 µm (200x200); 16-bit; 3.5GB

	Area	Mean	Min	Max
1	7.373E-9	7573.646	3990	12052

Value: 3990

☐ Preview

Figure 3.3 Workflow to detect single molecules and localize the detected molecules.

(A) Illustration of background subtraction (Min) and peak detection (Max). The background intensity was estimated from an area with no emitting fluorophores (yellow box) using the Measure function in ImageJ, and the minimum background value was then subtracted from all frames. **(B)** Demonstration of fluorophore localization. The image shows the wavelet filtered image which is used to find the fluorophores. **(C)** The image identifies the emitting fluorophores. The local maximum approach with '8-connected neighborhoods' is used to set parameters.

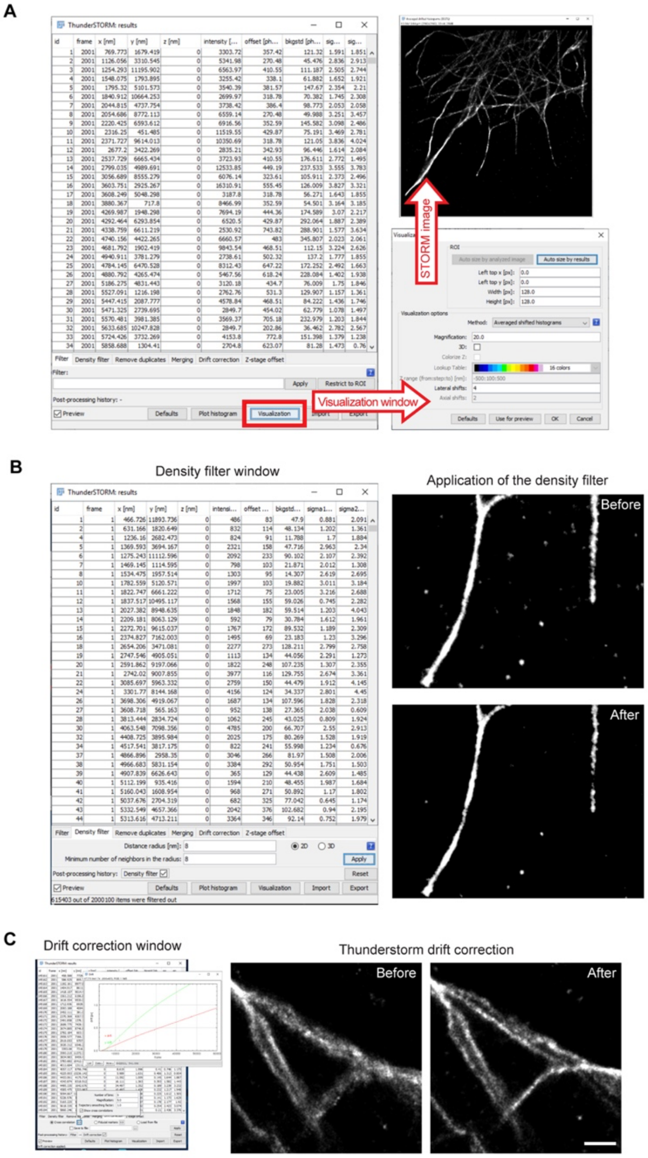

Figure 3.4 Visualization of single molecule data.

(A) Clicking on the visualization button on the Thunderstorm results window opens the Visualization window. Set the parameters and click OK to create the image. **(B)** The density filter removes unattached fluorophores by removing localizations that are not close to other localizations and are therefore not part of a structure. Here the cutoff is 8 localizations within an 8 nm radius. As these numbers increase, more localizations are removed which can start to affect continuous structures as well as unattached fluorophores. (left) Thunderstorm Density filter window and settings. (right-top) Image of microtubules before application of the density filter. (right-bottom) After application of the density filter. Notice that there are fewer isolated spots between the microtubules, and the microtubule on the right is less continuous as well. **(C)** Drift correction corrects for movement of the sample during data acquisition which leads to a blurring of the image. We select the cross-correlation method with the following settings: number of bins, 5; magnification, 5; trajectory smoothing factor, 1.0. (left) Thunderstorm drift correction window and plot of sample trajectory vs. frame. (middle) Image of microtubules before drift correction. (right) Image of microtubules after drift correction. Scale bar: 0.5 μm.

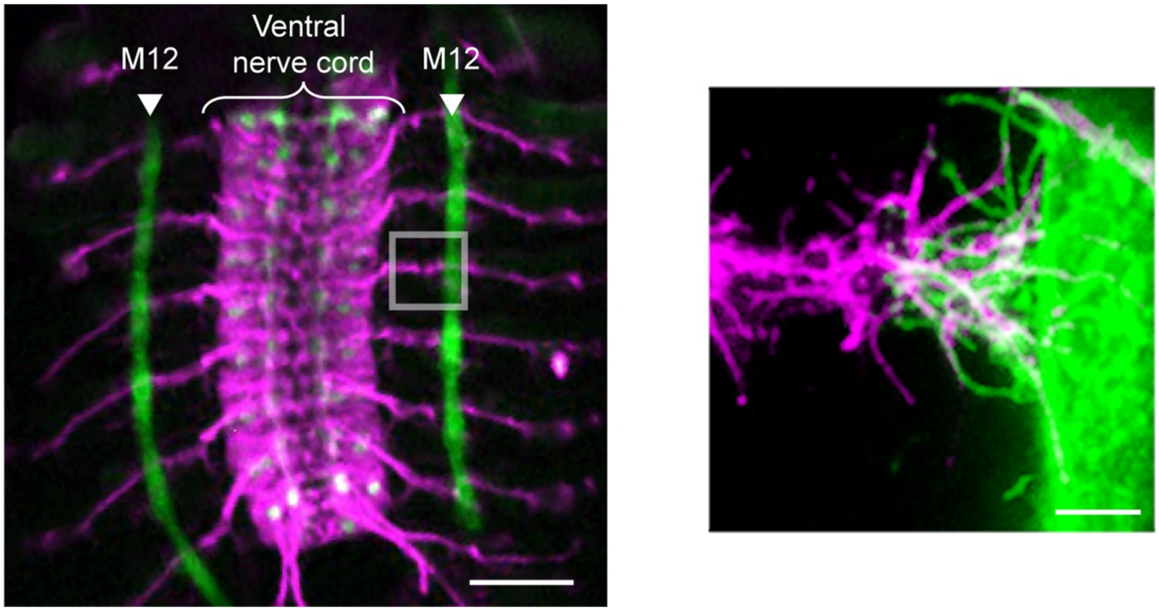

Figure 3.5 *in vivo* central nervous system.

The central nervous system is labeled with anti-HRP antibody (magenta) and a single muscle (M12) is labeled using *2702-GAL4* driver with GFP (green). The boxed region highlights the neuromuscular junction of the embryo. The right panel is a representative growth cone and muscle filopodia interaction during synaptogenesis. Once the initial contact is made, the filopodia undergo morphological changes by clustering at the synaptic site to form the synapse. Images were acquired with 10x objective (left) and 100x oil immersion objective (right). Scale bars: (left) 50 µm and (right) 5 µm. Genotype: *UAS-CD4-tdGFP, 2702-GAL4 / TM3*.

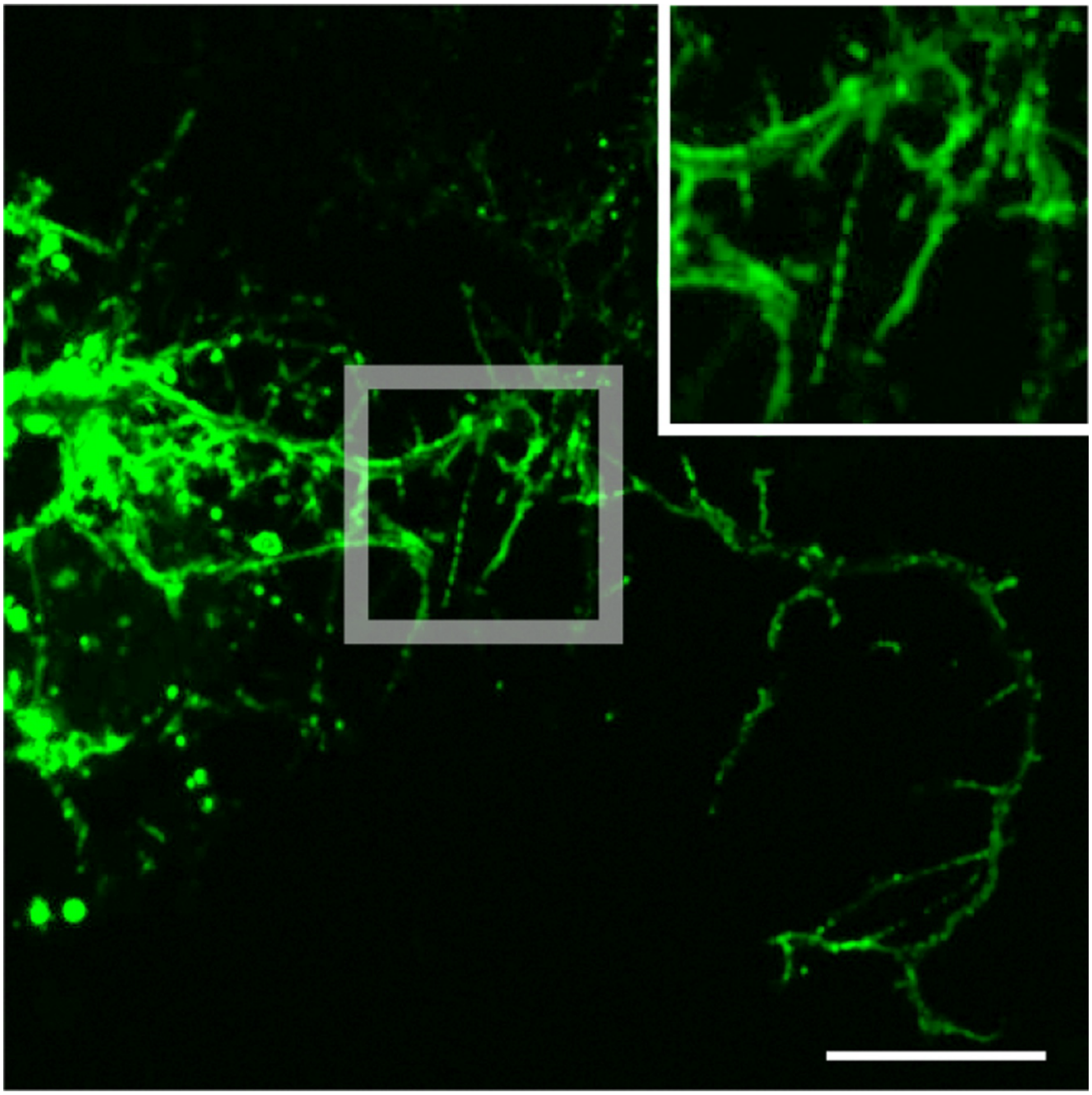

Figure 3.6 Neuronal cell culture expressing GFP on the plasma membrane.

The boxed region details the fine structural components of the neurite. The components such as filopodia and lamellipodia are important in forming mature synapses with their partners. Scale bar: 15 µm. Genotype: *UAS-myr::GFP; elav-GAL4.*

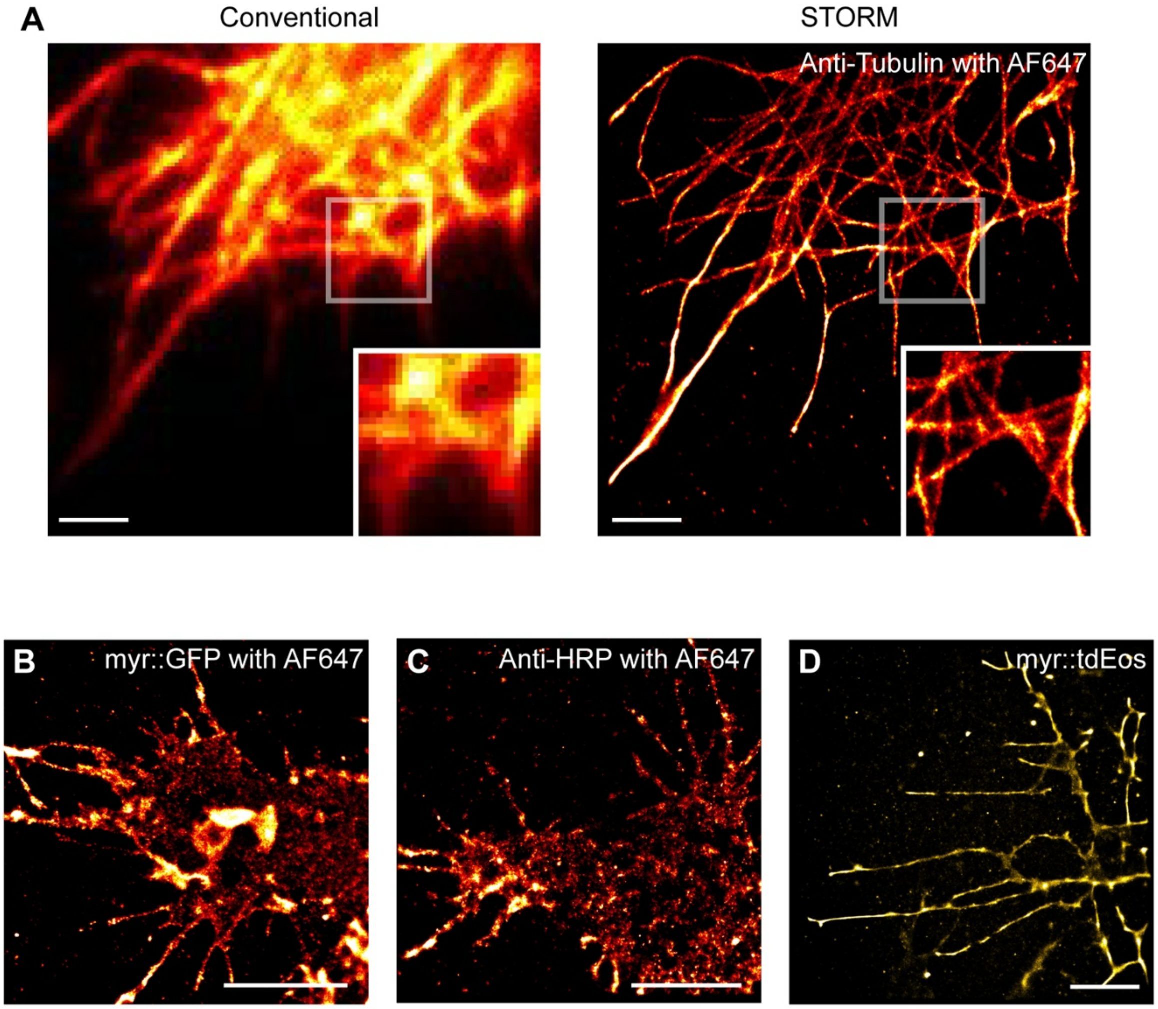

Figure 3.7 Reconstructed super-resolution images of various proteins labeled in primary neuron culture.

(**A**) Conventional wide-field (left) and super-resolution STORM (right) images of microtubules from primary neuronal cells, immunostained with Alexa Fluor 647. The super-resolution image is reconstructed from 60,000 acquired frames. The insets show the magnified regions of the white boxes. (**B-D**) Neurons immunostained with Alexa Fluor 647 (B and C) or labeled with tdEos (D). Scale bars: 2 µm. Genotypes: (A) *UAS-myr::GFP; elav-GAL4*, (B and C) *UAS-myr::GFP; elav-GAL4*, and (D) *UAS-myr::tdEos; elav-GAL4*.

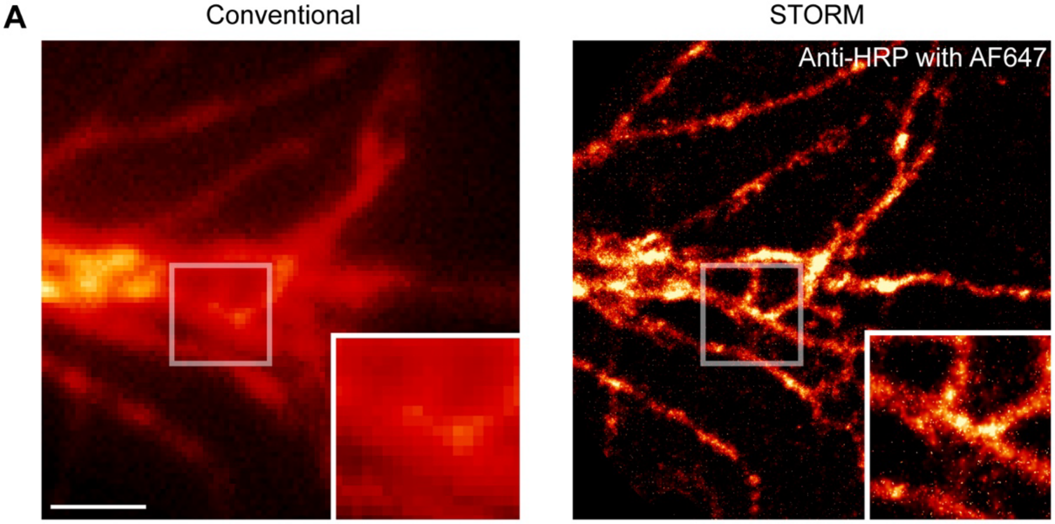

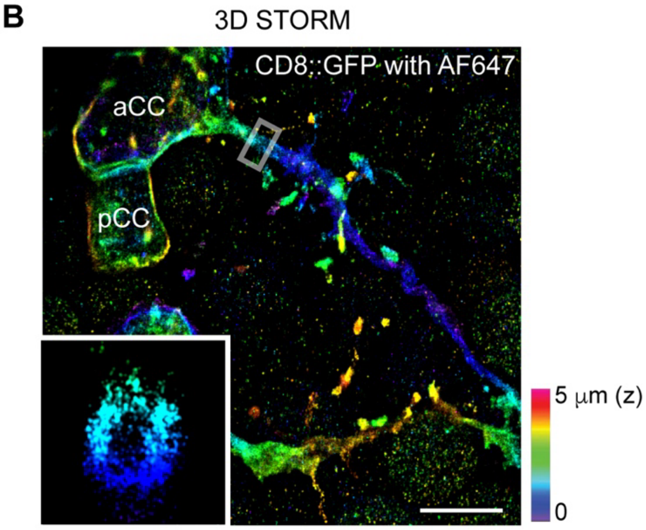

Figure 3.8 Reconstructed super-resolution images of neuronal membranes in dissected embryos.

(A) Conventional wide-field (left) and super-resolution STORM (right) images of motor neuron RP5 in anti-HRP labeled embryos, immunostained with AF647. The insets show the magnified regions of the white boxes. **(B)** An example of 3D STORM image. 3D reconstructed super-resolution image of aCC/pCC motoneurons labeled with GFP and immunostained with AF647.

The image is reconstructed from six z-slices that cover a total of 5 μm. The inset shows a hollow cross-section of the axon from the boxed region. Scale bars: (A) 2 μm, (B) 3 μm. Genotypes: (A) *UAS-CD4-tdGFP, 2702-GAL4 / TM3* and (B) *UAS-CD8-GFP, eve-GAL4*^{RN2}.

3.15 REFERENCES

Bellen, H. J., Tong, C., & Tsuda, H. (2010). 100 years of Drosophila research and its impact on vertebrate neuroscience: A history lesson for the future. *Nature Reviews Neuroscience*, *11*(7), 514–522. https://doi.org/10.1038/nrn2839

Campos-Ortega, J. A., & Hartenstein, V. (1985). *The Embryonic Development of Drosophila melanogaster*. Springer Berlin Heidelberg. https://doi.org/10.1007/978-3-662-02454-6

Campusano, J. M., Su, H., Jiang, S. A., Sicaeros, B., & O'Dowd, D. K. (2007). nAChR-mediated calcium responses and plasticity in *Drosophila* Kenyon cells. *Developmental Neurobiology*, *67*(11), 1520–1532. https://doi.org/10.1002/dneu.20527

Clark, M. Q., Zarin, A. A., Carreira-Rosario, A., & Doe, C. Q. (2018). Neural circuits driving larval locomotion in Drosophila. *Neural Development*, *13*(1), 6. https://doi.org/10.1186/s13064-018-0103-z

Dani, A., Huang, B., Bergan, J., Dulac, C., & Zhuang, X. (2010). Superresolution Imaging of Chemical Synapses in the Brain. *Neuron*, *68*(5), 843–856. https://doi.org/10.1016/j.neuron.2010.11.021

Del Castillo, U., Müller, H.-A. J., & Gelfand, V. I. (2020). Kinetochore protein Spindly controls microtubule polarity in *Drosophila* axons. *Proceedings of the National Academy of Sciences*, *117*(22), 12155–12163. https://doi.org/10.1073/pnas.2005394117

Dempsey, G. T., Vaughan, J. C., Chen, K. H., Bates, M., & Zhuang, X. (2011). Evaluation of fluorophores for optimal performance in localization-based super-resolution imaging. *Nature Methods*, *8*(12), 1027–1036. https://doi.org/10.1038/nmeth.1768

Doe, C. Q. (2017). Temporal Patterning in the *Drosophila* CNS. *Annual Review of Cell and Developmental Biology*, *33*(1), 219–240. https://doi.org/10.1146/annurev-cellbio-111315-125210

Egger, B., Van Giesen, L., Moraru, M., & Sprecher, S. G. (2013). In vitro imaging of primary neural cell culture from Drosophila. *Nature Protocols*, *8*(5), 958–965. https://doi.org/10.1038/nprot.2013.052

Furrer, M.-P., Vasenkova, I., Kamiyama, D., Rosado, Y., & Chiba, A. (2007). Slit and Robo control the development of dendrites in *Drosophila* CNS. *Development*, *134*(21), 3795–3804. https://doi.org/10.1242/dev.02882

Gao, R., Asano, S. M., Upadhyayula, S., Pisarev, I., Milkie, D. E., Liu, T.-L., Singh, V., Graves, A., Huynh, G. H., Zhao, Y., Bogovic, J., Colonell, J., Ott, C. M., Zugates, C., Tappan, S., Rodriguez, A., Mosaliganti, K. R., Sheu, S.-H., Pasolli, H. A., … Betzig, E. (2019). Cortical column and whole-brain imaging with molecular contrast and nanoscale resolution. *Science*, *363*(6424), eaau8302. https://doi.org/10.1126/science.aau8302

Huang, B., Bates, M., & Zhuang, X. (2009). Super-Resolution Fluorescence Microscopy. *Annual Review of Biochemistry*, *78*(1), 993–1016. https://doi.org/10.1146/annurev.biochem.77.061906.092014

Inal, M. A., Banzai, K., & Kamiyama, D. (2020b). Retrograde Tracing of Drosophila Embryonic Motor Neurons Using Lipophilic Fluorescent Dyes. *Journal of Visualized Experiments*, *155*, 60716. https://doi.org/10.3791/60716

Jiang, N., Kim, H.-J., Chozinski, T. J., Azpurua, J. E., Eaton, B. A., Vaughan, J. C., & Parrish, J. Z. (2018). Superresolution imaging of *Drosophila* tissues using expansion microscopy.

Molecular Biology of the Cell, *29*(12), 1413–1421. https://doi.org/10.1091/mbc.E17-10-0583

Jungmann, R., Avendaño, M. S., Woehrstein, J. B., Dai, M., Shih, W. M., & Yin, P. (2014). Multiplexed 3D cellular super-resolution imaging with DNA-PAINT and Exchange-PAINT. *Nature Methods*, *11*(3), 313–318. https://doi.org/10.1038/nmeth.2835

Jungmann, R., Steinhauer, C., Scheible, M., Kuzyk, A., Tinnefeld, P., & Simmel, F. C. (2010). Single-Molecule Kinetics and Super-Resolution Microscopy by Fluorescence Imaging of Transient Binding on DNA Origami. *Nano Letters*, *10*(11), 4756–4761. https://doi.org/10.1021/nl103427w

Kamiyama, D., & Chiba, A. (2009). Endogenous Activation Patterns of Cdc42 GTPase Within *Drosophila* Embryos. *Science*, *324*(5932), 1338–1340. https://doi.org/10.1126/science.1170615

Kamiyama, D., & Huang, B. (2012). Development in the STORM. *Developmental Cell*, *23*(6), 1103–1110. https://doi.org/10.1016/j.devcel.2012.10.003

Kamiyama, D., McGorty, R., Kamiyama, R., Kim, M. D., Chiba, A., & Huang, B. (2015). Specification of Dendritogenesis Site in Drosophila aCC Motoneuron by Membrane Enrichment of Pak1 through Dscam1. *Developmental Cell*, *35*(1), 93–106. https://doi.org/10.1016/j.devcel.2015.09.007

Katsuki, T., Ailani, D., Hiramoto, M., & Hiromi, Y. (2009). Intra-axonal Patterning: Intrinsic Compartmentalization of the Axonal Membrane in Drosophila Neurons. *Neuron*, *64*(2), 188–199. https://doi.org/10.1016/j.neuron.2009.08.019

Keshishian, H., Broadie, K., Chiba, A., & Bate, M. (1996b). The *Drosophila* Neuromuscular Junction: A Model System for Studying Synaptic Development and Function. *Annual*

Review of Neuroscience, *19*(1), 545–575. https://doi.org/10.1146/annurev.ne.19.030196.002553

Lichtman, J. W., & Denk, W. (2011). The Big and the Small: Challenges of Imaging the Brain's Circuits. *Science*, *334*(6056), 618–623. https://doi.org/10.1126/science.1209168

Manning, L., Heckscher, E. S., Purice, M. D., Roberts, J., Bennett, A. L., Kroll, J. R., Pollard, J. L., Strader, M. E., Lupton, J. R., Dyukareva, A. V., Doan, P. N., Bauer, D. M., Wilbur, A. N., Tanner, S., Kelly, J. J., Lai, S.-L., Tran, K. D., Kohwi, M., Laverty, T. R., … Doe, C. Q. (2012). A Resource for Manipulating Gene Expression and Analyzing cis-Regulatory Modules in the Drosophila CNS. *Cell Reports*, *2*(4), 1002–1013. https://doi.org/10.1016/j.celrep.2012.09.009

Martens, K. J. A., Bader, A. N., Baas, S., Rieger, B., & Hohlbein, J. (2018). Phasor based single-molecule localization microscopy in 3D (pSMLM-3D): An algorithm for MHz localization rates using standard CPUs. *The Journal of Chemical Physics*, *148*(12), 123311. https://doi.org/10.1063/1.5005899

McGorty, R., Kamiyama, D., & Huang, B. (2013). Active microscope stabilization in three dimensions using image correlation. *Optical Nanoscopy*, *2*(1), 3. https://doi.org/10.1186/2192-2853-2-3

Mohr, S., Bakal, C., & Perrimon, N. (2010). Genomic Screening with RNAi: Results and Challenges. *Annual Review of Biochemistry*, *79*(1), 37–64. https://doi.org/10.1146/annurev-biochem-060408-092949

Ovesný, M., Křížek, P., Borkovec, J., Švindrych, Z., & Hagen, G. M. (2014). ThunderSTORM: A comprehensive ImageJ plug-in for PALM and STORM data analysis and super-resolution imaging. *Bioinformatics*, *30*(16), 2389–2390. https://doi.org/10.1093/bioinformatics/btu202

Perrimon, N., & Mathey-Prevot, B. (2007). Applications of High-Throughput RNA Interference Screens to Problems in Cell and Developmental Biology. *Genetics*, *175*(1), 7–16. https://doi.org/10.1534/genetics.106.069963

Ritzenthaler, S., Suzuki, E., & Chiba, A. (2000b). Postsynaptic filopodia in muscle cells interact with innervating motoneuron axons. *Nature Neuroscience*, *3*(10), 1012–1017. https://doi.org/10.1038/79833

Scheffer, L. K., Xu, C. S., Januszewski, M., Lu, Z., Takemura, S., Hayworth, K. J., Huang, G. B., Shinomiya, K., Maitlin-Shepard, J., Berg, S., Clements, J., Hubbard, P. M., Katz, W. T., Umayam, L., Zhao, T., Ackerman, D., Blakely, T., Bogovic, J., Dolafi, T., … Plaza, S. M. (2020). A connectome and analysis of the adult Drosophila central brain. *eLife*, *9*, e57443. https://doi.org/10.7554/eLife.57443

Schnorrenberg, S., Grotjohann, T., Vorbrüggen, G., Herzig, A., Hell, S. W., & Jakobs, S. (2016). In vivo super-resolution RESOLFT microscopy of Drosophila melanogaster. *eLife*, *5*, e15567. https://doi.org/10.7554/eLife.15567

Sharifai, N., Samarajeewa, H., Kamiyama, D., Deng, T.-C., Boulina, M., & Chiba, A. (2014). Imaging Dynamic Molecular Signaling by the Cdc42 GTPase within the Developing CNS. *PLoS ONE*, *9*(2), e88870. https://doi.org/10.1371/journal.pone.0088870

Venken, K. J. T., Simpson, J. H., & Bellen, H. J. (2011). Genetic Manipulation of Genes and Cells in the Nervous System of the Fruit Fly. *Neuron*, *72*(2), 202–230. https://doi.org/10.1016/j.neuron.2011.09.021

Xu, K., Zhong, G., & Zhuang, X. (2013). Actin, Spectrin, and Associated Proteins Form a Periodic Cytoskeletal Structure in Axons. *Science*, *339*(6118), 452–456. https://doi.org/10.1126/science.1232251

CHAPTER 4

TWO ORTHOGONAL BINARY EXPRESSION SYSTEMS TARGETING DISTINCT NEURONAL AND MUSCLE SUBSETS IN *DROSOPHILA* EMBRYOS[3]

---

[3] Inal, MA. and Kamiyama, D. To be submitted to *G3: Genes, Genomes, Genetics*

4.1 ABSTRACT

In this study, we screened and identified orthogonal *Gal4* and *LexA* drivers for 2-color visualization of the neuromuscular junction (NMJ) in *Drosophila*. Here, we report a set of *Gal4* drivers useful in labeling subsets of muscles in spatial groups as well as a set of drivers that have stochastic activity single cell resolution for visualization of embryonic muscles. We also provide a small set of orthogonal *LexA* drivers that have early onset or late onset expression in motor neurons. Through time-lapse imaging of different muscles (VL1 and VO2), we gained new insights into development of the NMJ interactions. We also note the potential uses in studying muscle fusion events at single myoblast resolution. Altogether, understanding the roles of the genes that provide cell-specificity of *Gal4* activity in lines described in this report has high potentials to unlocking mechanisms that dictate muscle identity as well as machinery that controls synaptic specificity during neuromuscular development.

4.2 INTRODUCTION

Cell-to-cell contact is essential for the development and organization of multicellular organisms. In order to form functional tissues and organs, differentiated cells must locate and interact with their correct partners. This process is complicated by the fact that cells exist in highly dynamic and complex environments filled with diverse signaling cues. To establish proper connections, cells undergo coordinated changes in migration, restructure their internal components, and secrete signaling molecules to facilitate communication with neighboring cells. These responses are crucial for orchestrating embryogenesis and enabling tissue remodeling throughout development. A particularly striking example of the importance of cell-to-cell contact is observed during brain development. Neurons, despite the vast diversity of cell types and spatial complexity, are able to form precise synaptic connections with specific partners. These highly organized patterns of connectivity are vital for constructing functional neural circuits and supporting cognitive and sensory processes.

Model organisms have been instrumental in uncovering the mechanisms behind neuronal contact and connectivity. The fruit fly, *Drosophila melanogaster*, has emerged as a powerful system due to its sophisticated genetic tools, relatively small brain, and rapid development. Recently, advances in connectomics—using serial electron microscopy reconstructions—and single-cell RNA sequencing have enabled researchers to study neural interactions at multiple levels, from molecular signaling to whole-brain architecture (Dorkenwald et al., 2024; H. Li et al., 2022; Winding et al., 2023). Because of the dynamic and spatially complex nature of cell-to-cell interactions, high-resolution imaging techniques are essential for studying these processes in detail. Recent advances in deep-tissue live imaging have enabled researchers to observe how olfactory receptor neurons extend axons and how projection neuron (PN) dendrites target specific regions within the glomeruli during olfactory circuit formation (T. Li et al., 2021). Their studies revealed the dynamic behavior of axonal and dendritic filopodia during synaptic partner matching. Another widely studied model for synaptic partner matching is the neuromuscular junction (NMJ) during embryogenesis. The NMJ is an ideal system because of its well-characterized anatomy, stereotyped development, and dynamic cellular interactions. Additionally, *Drosophila* embryos are transparent, and the NMJ forms at relatively shallow locations, making it highly accessible for live imaging.

In each abdominal hemisegment of the embryo, 36 motor neurons innervate a precise set of 30 muscle fibers (Arzan Zarin & Labrador, 2019; Landgraf et al., 1997). This connectivity pattern is remarkably stereotyped across embryos, providing an ideal system to study the molecular and cellular mechanisms that ensure accurate synaptic partner selection during development. For many years, it was thought that the axonal growth cones extended filopodia that actively sensed and responded to chemical cues—both short-range and long-range—provided by the muscle cells, which were viewed as passive targets. However, the discovery of dynamic filopodia-like structures on the muscle cells themselves, known as myopodia, has fundamentally shifted this perspective (Ritzenthaler et al., 2000; Suzuki et al., 2000). This finding suggests that synaptic partner matching is a bidirectional process, with both motor neurons and muscle fibers contributing to contact formation and stabilization. Furthermore, Ritzenthaler's studies have shown that muscle cells can also play a repulsive role by eliminating inappropriate contacts with non-partner motor neurons (Ritzenthaler & Chiba, 2003). This dual role—promoting correct connections while discouraging incorrect ones—ensures the specificity and robustness of neuromuscular connectivity during development.

These insights were particularly evident in studies of the interaction between muscle 12 (M12) and its corresponding motor neurons (MN12s). To visualize these interactions, researchers employed the *GAL4/UAS* binary expression system (Ritzenthaler et al., 2000). A muscle-specific *GAL4* driver, *M12-GAL4*, was used to express membrane-targeted GFP in M12, allowing for the fluorescent labeling of the muscle membrane. Simultaneously, motor neurons were labeled using an anti-horseradish peroxidase (HRP) antibody following live fillet dissection, which broadly marks neurons by recognizing a sugar moiety found in insect neuronal membranes. Using two-color live imaging, researchers were able to simultaneously observe GFP-labeled muscle cells and HRP-stained neurons (Ritzenthaler et al., 2000). This approach enabled direct visualization of the dynamic behaviors of both myopodia and motor neuron filopodia during the process of synaptic partner matching. Despite these important findings, some technical limitations remain. The number of available muscle-specific *GAL4* lines is limited, which restricts the ability to investigate other muscle-motor neuron pairs beyond the M12-MN12 system. Additionally, the absence of a complementary binary expression system, such as LexA-based drivers for motor neurons, limits simultaneous, cell-type-specific labeling and manipulation of both pre- and postsynaptic components in other circuits.

To address these limitations, we present a genetic toolkit comprising *GAL4* and *LexA* drivers designed to facilitate the study of contact formation between muscles and motor neurons. In this toolkit, we identified seven new *GAL4* drivers that enable the labeling of distinct muscle groups (ventral, lateral, and dorsal) with stable expression. Additionally, we found three *GAL4* lines that offer stochastic, single-cell resolution labeling across the musculature. For motor neurons, we identified three *LexA* drivers with distinct temporal expression profiles: two exhibit early-onset expression, allowing for the investigation of early neuromuscular connectivity, with clear resolution between ventral and dorsal motor neuron populations; the third shows late-onset expression. Using this toolkit, we observed a variety of membrane protrusion-based contact sites between muscles and neurons. We also identified filopodia that do not interact with motor neurons, suggesting additional complexity in muscle membrane dynamics during development. These genetic tools not only enable detailed studies of neuromuscular contact formation but also have the potential to advance our understanding of how individual muscles are developmentally programmed during embryogenesis, due to the versatility of the *Drosophila* genetic system.

RESULTS

4.3 SCREENING STRATEGY TO IDENTIFY *GAL4* LINES SPECIFIC TO SUBSETS OR SINGLE MUSCLES

To identify driver lines specific to subsets or single muscles, we took advantage of the series of GAL4 lines generated as a large-scale effort allowing to test the enhancer activity of genomic DNA in neurons as well as other cell types (Pfeiffer et al., 2008). This extensive collection of *GAL4* lines was developed by research groups at Janelia Research Campus. Leveraging the associated large-scale imaging datasets (https://flweb.janelia.org/cgi-bin/flew.cgi), we designed a pipeline for systematic screening (**Figure S4.1A**). First, we reviewed images of stage 16 (around 13:00-16:00 h after egg laying [AEL]) embryos with body wall annotation for 2480 lines in the datasets. We prioritized candidates that had small subsets of expression in the body wall, and excluded lines whose expression was largely found in epithelia, narrowing our search to 85 lines. We then screened these lines using a membrane-targeted GFP marker (*UAS-gapGFP*) in dissected embryos at 10x magnification with a confocal microscope. This preliminary screen led to identification of 10 lines which we grouped into two sets. The first set of lines have expression in groups of muscles that are stably expressed in each segment, in multiple animals. The latter set has less stable expression in various parts of the body which provides single muscle resolution expression. Details of these two sets are described below.

4.4 IDENTIFICATION AND CHARACTERIZATION OF SEVEN *GAL4* DRIVERS WITH STABLE EXPRESSION IN SMALL SUBSETS OF EMBRYONIC MUSCLES

In our first set of muscle specific *GAL4* drivers, there are 7 lines that provide stable expression in subsets of different muscle groups based on their position along the body wall. Based on their expression patterns, we organized these lines into four categories defined by spatial muscle groupings (**Figure S4.1B**): ventral (3 lines), lateral (1 line), ventral/dorsal (2 lines) or broad (subsets of muscle in each of the positional groups; 1 line). In our descriptions we use nomenclature systems from Landgraf et al., 1997 and use line names given by Janelia to refer to specific drivers.

The muscles are innervated by motor neurons that project through two main nerve roots except for the transverse nerve (TN), which runs along the segmental border to innervate VT1 (25) (**Figure S4.1B**). These two tracks are split into the segmental nerve (SN) or the intersegmental nerve (ISN) (Landgraf et al, 2003, PLOS Biology). Based on our categories, the ventral muscle group is innervated by SNc, ISNd and ISNb nerves (**Figure S4.1B**; magenta group). The lateral muscle group is innervated by SNa, which targets lateral transverse muscles 1-4 (LT1-4; 21-24), lateral oblique muscle 1 (LO1; 5) and segmental border muscle (SBM; 8) (**Figure S4.1B**; green group). Included in this group due to its orientation and relative spatial positioning are DT1 (18) and LL1 (4), which are innervated by ISN (**Figure S4.1B**; green). The remainder of the musculature is categorized as dorsal muscles and is innervated by ISN. (**Figure S4.1B**; cyan group).

Ventral muscle drivers

We found 2 lines specific to only a subset of ventral muscles. R33E02 (RRID: 49751) is primarily active in ventral oblique musculature innervated by ISNb (VO1-2), excluding VO3 (28) (**Figure 4.1A**). In contrast to the previous line, this line has activity in ventral lateral muscle VL1 (12) which is also innervated by ISNb (**Figure 4.1A**). R15F04 (RRID: 47866) is the line that has the highest coverage in all the ventral lateral musculature which are innervated by ISNb (VL1-4; 7, 6, 13, 12) (**Figure 4.1B**). Similar to R27F08, it also has expression in the ventral oblique musculature (VO4-6; 15-17) (**Figure 4.1B**).

Ventral + dorsal muscle drivers

We found 3 lines that have expression in subsets of ventral and dorsal musculature. R27F08 (RRID: 49232) has activity in the ventral-most oblique musculature near the ventral nerve cord. Expression is found in muscles VO4, 5 (15, 16) as well as VL1, VL2. Dorsal expression is observed in LL1 (4) and DT1 (18) (**Figure 4.2A**). R11H11 and R48D05 (RRID: 48480 and 50362) have similar dorsal expression pattern covering DA1, DA2, DO1, and DO2 (1,2,9,10), although they have different ventral muscle coverage (**Figures 4.2B** and **4.2C**). R11H11 has a broader coverage of ventral musculature with expression in ventral oblique muscles (VO4-6), and subset of ventral lateral muscles 1 and 3 (12 and 6) (**Figure 4.2B**). On the other hand, R48D05 is restricted to a subset of oblique muscles in the ventral region (VO3-6; 28, 15-17) (**Figure 4.2C**).

Lateral muscle driver

R40A07 (RRID: 50074) expression is primarily found in external muscles. This line targets all of the lateral transverse muscles LT1-4 (21-24) as well as the dorsal transverse muscle (18) which is innervated by ISN (**Figure 4.2D**). In addition, this line targets 2 external ventral muscles (VA1, VA2; 26, 27) (**Figure 4.2D**).

Broad driver

The previous lines have specific expression in only one or two specific groups of musculatures allowing specifically targeted studies in such groups. We found that R31F06 (RRID: 49684) might be a useful line to increase coverage while not targeting all muscles. While this line shows expression in ventral, lateral, and dorsal muscle groups, it is restricted to selected subsets of muscles, providing single-muscle resolution with broader overall coverage. In the ventral domain, VO4-6, VO1-2, VL1 have activity (**Figure 4.2E**). In the lateral domain LT2-4, and LL1 are active (**Figure 4.2E**). In the dorsal domain, similar to the lines described above, we observe the DA1-2 and DO1-2 activity (**Figure 4.2E**).

4.5 *GAL4* EXPRESSION IN RANDOM SUBSETS OF MUSCLES FOR SINGLE-MUSCLE STUDIES

During our screening of *GAL4* drivers, we observed that some drivers exhibited expression in random subsets of muscles. While stable lines are valuable for studying muscles in clusters, the stochastic nature of *GAL4* expression in certain lines can be advantageous for achieving true single-muscle experiments. Thus, our second set of *GAL4* drivers was selected to provide single-cell resolution expression with medium to high coverage. For this we further characterized R9H06, R23B04 and R28E05 (RRID:47439, 49016 and 49459) to assess the stochastic coverage of each muscle. We crossed these lines to membrane-targeted GFP makers (*UAS-CD4::tdGFP* or *UAS-gapGFP*) and used anti-GFP antibody to closely examine each *GAL4* line at stage 16.

R9H06-GAL4 is a powerful line for achieving single cell resolution in 29/30 of the muscles due to its completely stochastic nature. Because the muscles don't have a stable expression, each sample can have a different combination of muscle expression. Within the same animal, this also translates to segmental expression differences (**Figure 4.3A**). This line has additional coverage of the dorsal musculature that were also not stably active previous lines. Although this line has the highest stochastic muscle coverage, in the ventral musculature VA2 and VT1 (27 and 25) are least frequently observed (<10%) (**Figure 4.3B**). Similarly, in the lateral region LT1 (21) and LT4 (24) are rarely visualized and dorsally DO5 (20) has the least frequent expression (**Figure 4.3B**). On the other hand, we were not able to observe any expression in VA3 (29) (**Figure 4.3B**).

R23B04 (RRID: 49016) provides coverage of 12 muscles at single cell resolution VO4 (15), VO6 (17), LO1/SBM (5/8), LT1-4 (21-24), DT1 (18), LL1(4), DO4 (19), DA2 (2) (**Figure 4.3B** and **S4.2A**). The stochasticity is particularly useful to target VA3 (29), which is missing in the R9H06 line (**Figure 4.3B**). There is also coverage in ventral lateral musculature. The ventral muscles VL 4 and 1 (7 and 12, respectively) are randomly expressed, while VL3 (6) activity found in each segment, though they are not single cell resolved (**Figure 4.3B** and **S4.2A**). In addition, VO4-6 (15-17) near the ventral nerve cord is expressed in combination across segments (**Figure 4.3B** and **S4.2A**).

Lastly, R28E05 (RRID: 49459) provides the lacking coverage into single cells by stochastic expression in VL2, VO1, DO5 (13, 30 and 20) (**Figure 4.3B** and **S4.2B**), adding up to total coverage of 30/30 muscles at single cell resolution. Interestingly, this line provides wide coverage of ventral and dorsal musculature while lacking expression in lateral transverse muscles entirely. Altogether these lines provide coverage of every muscle with at least 20% frequency (VT1, VA3, VO6), although majority of them are active at ≥30% frequency.

Finally, we note that these *GAL4* lines are active in the late stage 15 embryo, and we occasionally observed labeling in presumptive muscle cells before myoblast fusion was complete (**Figure S4.2C**). This early expression provides an additional advantage for studying the cellular dynamics of myogenesis (see also Discussion).

4.6 DISCOVERY OF NOVEL *LEXA* DRIVERS SPECIFIC TO MOTOR NEURONS

One of the key events of post-synaptic differentiation follows presynaptic contact by the motor neuron. There are various immunofluorescence-based approaches that allow the visualization of the presynaptic motor neuron in conjunction with the post synaptic muscle such as using the anti-HRP (against a sugar moiety only found in the neurons of insects) or anti-Fas2 (primarily expressed by motor neurons) antibodies. Among these, anti-HRP has been successfully used for live imaging following live fillet dissection of embryos. However, its application is limited to short-term imaging due to tissue viability constraints. Alternatively, the use of an orthogonal expression system such as the bacterial *LexA/LexAop* constructs can provide the necessary resolution to study the intercellular communication between motor neurons and muscles in developing whole animals. However, *LexA* lines specific to motor neurons, particularly during embryonic stages, have not been well-characterized. To address this, we initiated a screening effort to identify suitable lines.

Motor Neuron-Specific VGlut Driver

There have been previous reports on *GAL4* drivers that are motor neuron specific, and some are generated by relying on the activity of *VGlut* gene or its enhancers. These lines are typically used in larval studies primarily rather than embryos. Nevertheless, previous literature report that *VGlut* activity begins from stage 15 (11:20-13:00 h AEL), prior to neuromuscular interaction (Mahr & Aberle, 2006). Thus, we reasoned this driver can be used to study the formation of neuromuscular junction. We tested the expression pattern of *VGlut* gene-trap *LexA* line by crossing it to a membrane-targeted GFP maker (*LexAop2-CD4::tdGFP*). We found the expression pattern is exclusive to the motor neurons (**Figure 4.4A**). Since the activation of the *LexAop* and translation of the FP takes some time, we found that the earliest activity of this gene does not allow the live visualization of the very first contact between the neuron and the muscle but has improved activity the later stages, where the FP expression is increased resulting in continuous labeling of the membrane towards the end of stage 16 (15:00-16:00 h AEL onward).

Early-Onset Neuronal LexA Driver

While the *VGlut-LexA* is a valuable tool for studying NMJ development, its limited expression during the early onset of motor neuron–muscle contact restricts its use for cellular studies at early stage 16 (13:00-14:00 h AEL). Thus, we wanted to find a driver that has strong activity early on in development that allows studies of early synaptic contact between the motor neuron and the muscle. To this end, like the *GAL4* screen, we screened a set of *LexA* lines generated by Janelia.

Since the efforts of making these lines were specific to study neuronal populations, we looked at annotations for both stages 9-12 (i.e. germ band elongated) and 16 of each line (Manning et al., 2012; Pfeiffer et al., 2008). We screened ~20 candidate drivers annotated to be active in small or large subsets during stage 16, and in all neurons during germ band elongation stage. To check the expression pattern of the *LexA* drivers, we crossed them to *LexAop-rCD2::RFP* and imaged them under 10x objective. In this screen there were 7 lines that had any strong expression in the ventral nerve cord. Of these, we found two lines to be useful as motoneuron drivers (R11D01, R45B10; RRID: 52430, 53646) and looked at them at higher magnification. Both lines showed strong LexA activity during stage 16 (**Figure 4.4B, C**). In particular, we found R11D01 have a cleaner expression in the ventral region for imaging ISNb motoneurons while R45B10 had more frequent leaky expressions in the ventral musculature. Based on these findings, R11D01 was identified as a promising candidate. However, we also observed additional labeling in non-motor neuron cells (**Movie 4.1** and **Figure S4.2**), which should be taken into account when designing experiments.

4.7 TWO-COLOR LIVE IMAGING OF NEUROMUSCULAR JUNCTIONS DURING EMBRYOGENESIS

Finally, with our new tools, we studied the dynamics of motor neuron–muscle contacts before and after the onset of muscle contraction. For this, we used *R11H11-GAL4* (with *UAS-CD4::tdGFP*) in conjunction with *VGlut-LexA* (with *LexAop2-CD4::tdTomato*), to study VO2 (14.1) activity following the time point of stable contact formation in VL1. While gut morphology is important for assessing the general developmental stage of an embryo, synaptic contacts form in a short window and develop rapidly, making subcellular level synchronization challenging. Since this driver also has single cell resolution VL1 (12) activity, we used it as an internal marker for a direct temporal comparison for VO2 (14.1). To our knowledge, this represents the first report characterizing how VO2 establishes contact with motor neurons at the subcellular level.

To assess neuron–muscle interactions prior to the onset of muscle contraction, we focused on the time point when VL1 forms stable contacts, approximately 15:30 h AEL as previously described (Kohsaka & Nose, 2009) (**Movie 4.2**). At this stage, VL1 has a sheet-like structure that interacts with the characteristic two branches of its partner neuron at the presumable synaptic site as reported previously (Halpern et al., 1991). The sheet-like structure also has a dip between the bifurcation site of the motor neuron (**Figure 4.5A'**, asterisk). Although the morphology of the interaction site resembles the sheet-like structures reported in previous studies, there appear to be dynamic filopodial activity that subside, leading to a smoother edge for the sheet-like structure (**Figure 4.6A'**). Interestingly, VO2 also has filopodia activity at its surface (**Figure 4.6A, A''**). This activity is found in the anteriodorsal part of the muscle. These projections appear as clustered filopodia and may interact with branches of a different motor neuron, RP1. In contrast to VL1 at this stage, VO2 does not have any sheet-like structures at this timepoint (**Figure 4.6A, A''**), suggesting timing and/or morphology of synaptic contacts are different between partners.

We next examined the morphology of VL1 and VO2 after the onset of muscle contraction. Once functional synapses are formed, muscle contraction begins around 16:30 h AEL in isolated twitches that propagate across segments (Crisp et al., 2008). We used whole embryonic preparation with the same genetic crosses from the previous set to track the changes on morphology in VL1 and VO2 (**Movie 4.3**). Interestingly, during this time point, we observed large sheet-like structures extending from VL1 at the NMJ (**Figure 4.5A, A'**). These structures relative to the earlier time point appear to also have thin structures connected at the edge, although they do not appear to have dynamic filopodial activity. In addition, this sheet-like structure has a different morphology than the earlier structure described above. While in the younger embryo, the sheet-like structure was split into two regions at the bifurcation point of the motor neuron, at the onset of contraction the gap has been filled between the two regions resulting in a single sheet (**Figure 4.6A, A'**). In addition, the motor neuron appears to be tightly integrated into the sheet, remaining attached even during vigorous muscle twitches **(Movie 4.3)**. On the other hand, the surface of VO2 appears to be lacking any protrusions, filopodia or sheet-like structure (**Figure 4.5A''**). However, there appear a few ridges in place of what used to be filopodia (**Figure 4.6A''**). These observations suggest that the morphological activity of muscle surfaces decreases as contraction begins.

Together, our observations demonstrate that neuron–muscle contact dynamics vary across muscle types, both in timing and structure. Following the onset of muscle contraction, synaptic contacts appear to stabilize, with a reduction in dynamic morphological features.

4.8 DISCUSSION

In this study, we report a set of *GAL4* drivers that provide specificity in spatially distinct muscle groups as well as drivers that provide stochastic single cell resolvable muscle activity for genetic and morphological studies. In addition, we identified a small set of *LexA* drivers that have activity in motor neurons during axon guidance (early onset) or during synaptogenesis (late onset). Using these tools during neuromuscular junction development in conjunction with high spatiotemporal resolution confocal microscopy, we gained novel insights into NMJ development.

Morphological Specificity of Synaptic Contacts

While motor neurons successfully reach their target muscles during development, the underlying mechanisms that guide this precise connectivity remain incompletely understood. This study was inspired by early observations—around the turn of the millennium—highlighting the importance of filopodia–filopodia interactions in neuron–muscle targeting. Although VL1 (12) muscle has been well studied, little is known about the morphological features of other muscles, primarily due to the lack of tools that enable high-resolution imaging of small muscle subsets.

Our study reveals that different muscles develop distinct morphological characteristics during synaptogenesis. For example, VL1 forms stable contacts with its partner motor neuron via a sheet-like structure (**Figure 4.5A and A'**). Although VL1 initially exhibits a filopodial cluster, these filopodia mature into a sheet-like formation, a transition previously described (Inal et al., 2021; Kohsaka et al., 2007; Kohsaka & Nose, 2009; Ritzenthaler et al., 2000). Interestingly, VL1's sheet-like structure further evolves into a smoother, single-peaked form during muscle contraction (**Figure 4.6A and A'**). Live imaging suggests that this sheet-like structure develops in two steps: first, the axon terminal makes specific contacts at the anterior and posterior branches of the partner neuron, forming two distinct sheet-like structures. Subsequently, through a mechanism yet to be defined—possibly involving mechanical tension at the neuron-muscle interface—these two sheets merge into a single cohesive structure that remains stable during early muscle contractions.

A key new finding is that during VO2 filopodia clustering, its partner motor neuron lacks sheet-like processes at its terminal. Instead, VO2 engages the motor neuron through a cluster of filopodia at the presumptive synaptic site, which later transitions into membrane ridges at the synaptic site (**Figure 4.6A and A''**). These findings are intriguing because muscles that appear morphologically similar at first glance display clear and evolving structural differences over time. This raises important questions: why do these morphological differences arise? Are they functionally significant, and do they influence synaptic specificity or robustness?

Molecular Specificity in Neuromuscular Matching

The specificity of neuron–muscle connections has led to the hypothesis that corresponding neurons and muscles express matching sets of adhesion molecules, functioning like a "key and lock" system. Researchers also proposed that a local balance of adhesion and repulsion signals could fine-tune specificity. These models often assume that different muscles express distinct cell surface proteins at specific times and locations during development. Identifying which proteins are involved and how they are spatially and temporally regulated is a crucial next step.

Our collection of GAL4 lines, each active in specific muscle subsets, provides powerful tools to explore these questions. We have characterized six lines to date (see **Supplementary Table 4.1**), each constructed by linking GAL4 to distinct cis-regulatory modules (CRMs) near specific genes. For example, R48A07 is derived from an enhancer sequence located within an intron between the third and fourth exons of the apterous gene, spanning 2,554 base pairs. Imaging data confirm that R48A07 drives expression exclusively in external muscles (LT1-4; VA1-2, and DT1) (**Figure 4.2D**). This aligns with apterous, a well-characterized muscle identity transcription factor (iTF) known for defining the distinct properties of external muscles. The expression pattern of apterous closely mirrors the activity of R48A07.

We are now investigating how the other *GAL4* lines—R27F08, R33E02, R15A04, R11H11, and R48D05—and their associated genes (*Limpet, Src64B, single-minded, GycBeta100B, and Dpr10*) contribute to muscle identity and synaptic connectivity. For instance, *Limpet* is recognized as a negative regulator of the *Wnt* signaling pathway, potentially dampening β-catenin–dependent transcription of genes critical for muscle differentiation and surface protein expression. Although these *GAL4* lines may not fully replicate the endogenous expression patterns of their corresponding genes (Ashley et al., 2019; Hammonds et al., 2013; Tomancak et al., 2002, 2007), they offer valuable entry points for studying the molecular logic of synaptic specificity. Continuing this work will help uncover how precise neuron–muscle connections are established and may shed light on broader principles of neuromuscular development.

Broad Applications and Future Directions

Because our *GAL4* lines are active early in development, they also provide access to key stages of muscle formation, including the fusion of fusion-competent myoblasts (FCMs) with founder cells (FCs). FCs, each defined by unique molecular identities, are spatially arranged in specific domains of the embryonic body wall and fuse with adjacent FCMs. However, how subsets of FCMs are specified to fuse with particular FCs—and how they acquire FC-like molecular identity—remains poorly understood (Baylies et al., 1998; Dobi et al., 2015).

Our system offers a means to explore these questions in greater detail. In particular, the stochastic driver *R23B04-GAL4* enables single-cell resolution when multiple FCMs are located near a given FC (**Figure S4.2C**). Unlike existing FCM-specific drivers such as *sns-GAL4*, which label all FCMs and obscure individual fusion events, *R23B04-GAL4* provides the specificity necessary to resolve single FCM dynamics. Using this driver, we observed isolated FCM expression adjacent to growing myotubes at stage 15—a developmental window during which fusion frequency is significantly reduced (Beckett & Baylies, 2007). At this stage, we captured high spatiotemporal resolution of FCM recruitment to FCs, including interactions mediated by podosome-like structure (PLS). PLS are gaining attention as key mediators in the early stages of myoblast fusion. With our genetic tools, we can directly visualize how PLS contribute to the acquisition of FC-like identity in a cell-type–specific and time-resolved manner. Furthermore, this system allows us to investigate whether FCMs from the same spatial domain exhibit divergent fusion behaviors, pointing to potential molecular heterogeneity prior to fusion.

Beyond early fusion events, this framework supports investigation of later aspects of muscle development, including myonuclear positioning, myotendinous junction formation, sarcomere organization, and myofibrillogenesis. Our *LexA* driver lines further broaden this platform by enabling parallel studies of glia–muscle interactions (**Figure S4.3**), offering a valuable toolset for examining diverse cell–cell communication processes during embryogenesis. These tools also allow us to explore how dynamic cellular structures—such as filopodia and sheet-like extensions—contribute to morphogenesis and functional circuit formation. Altogether, this genetic toolkit provides a versatile and high-resolution approach to studying muscle development and synaptic connectivity with single-cell precision.

4.9 FIGURES

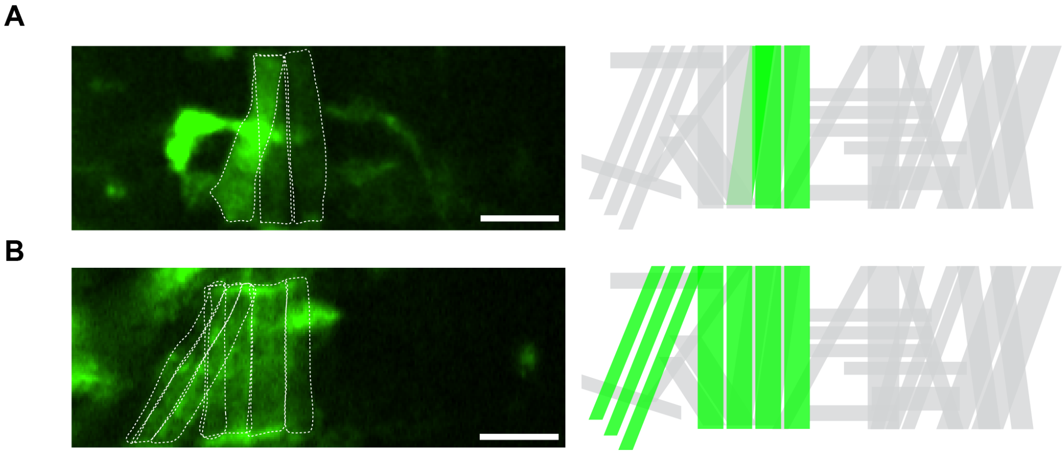

Figure 4.1 ***Gal4*** **drivers specific to ventral muscle groups are visualized by UAS-GapGFP reporter in filleted embryos during stage 16.**

Single representative segment expression is demonstrated for each line. The right panel is a colored-in muscle schematic highlighting in green which muscles have activity in each driver. The same muscles in a single segment are also shown in the right panel with dotted outlines. Other bright regions that do not match with the musculature layout may represent non-muscle derived cells. (**A**) *R33E02-Gal4* pattern. **(B)** *R15F04-Gal4* pattern. Scalebar: 50 µm.

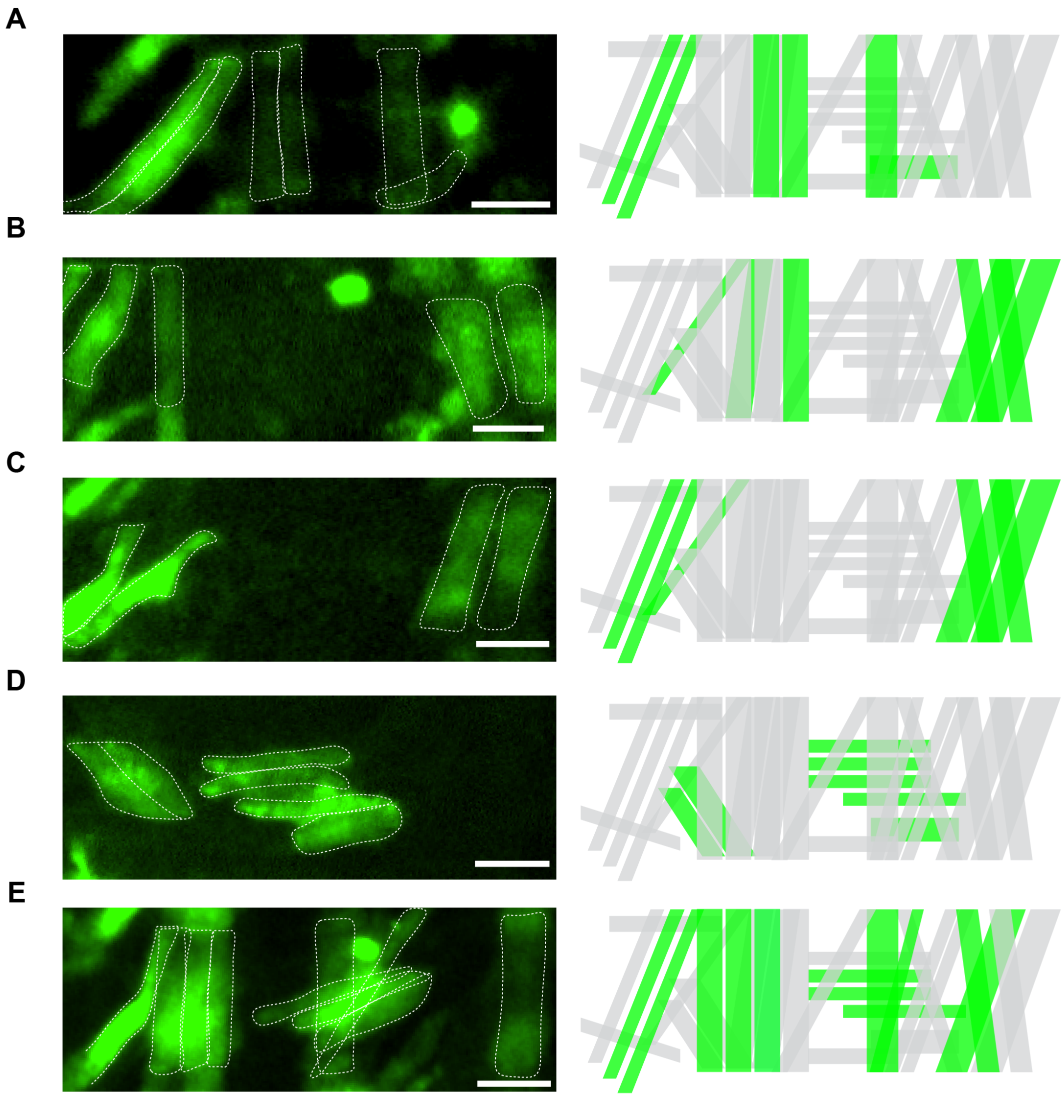

Figure 4.2 *Gal4* drivers with ventral+dorsal (A,B, C), lateral (D) and broad (E) muscle activities as in Figure 4.1.

(A) *R27F08-Gal4* pattern. There is an unmarked muscle in the upper left corner of the image, which was omitted due to presence of same muscle labeling in the posterior segment which was outlined. **(B)** *R11H11-Gal4* pattern. Posterior segment muscles were omitted in the outline. **(C)** *R48D05-Gal4* pattern. Anterior segment muscles were omitted in the outline. **(D)** *R40A07-Gal4* pattern. **(E)** *R31F06-Gal4* pattern. Anterior segment muscles were omitted in the outline. Scalebar: 50 µm.

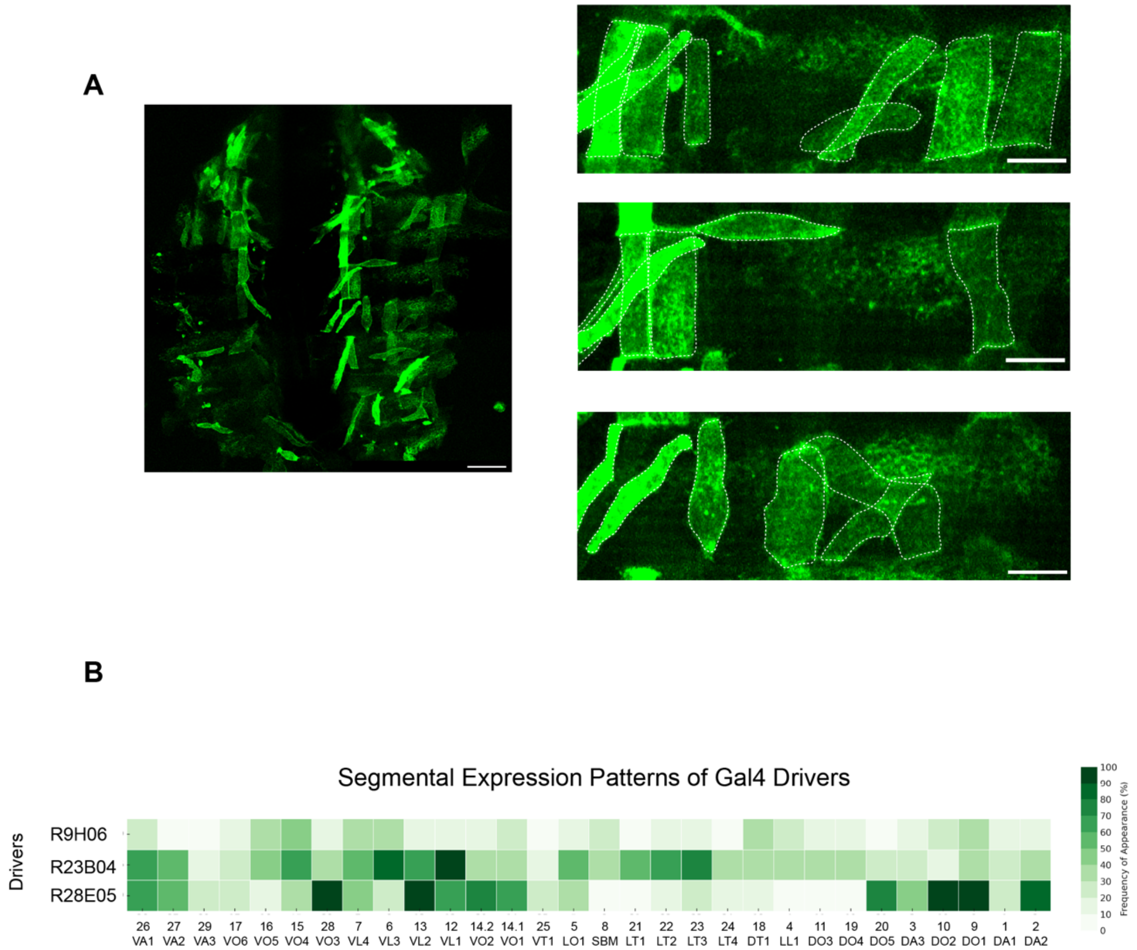

Figure 4.3 *Gal4* drivers with stochastic muscle activity.

(A) R9H06-Gal4 crossed to *UAS-CD4::tdGFP* was filleted as stage 16 embryo and immuno-stained with anti-GFP. Three panels are magnified right hemisegments with muscle cells outlined from the complete embryo demonstrating the variation of expression among segments. Some fluorescence signal comes from the epithelial cells. Scalebar: 50 µm (left), 20 µm (right). **(B)** Expression frequency of each muscle between A1-A6 segments for the *Gal4* drivers (R9H06, R23B04. R28E05) that have stochastic single cell activity. The layout is organized from ventral to distal domains of body wall; each cell has a muscle ID indicated below the heatmap. n = 36, 30, 30 hemisegments (5 embryos each) respectively.

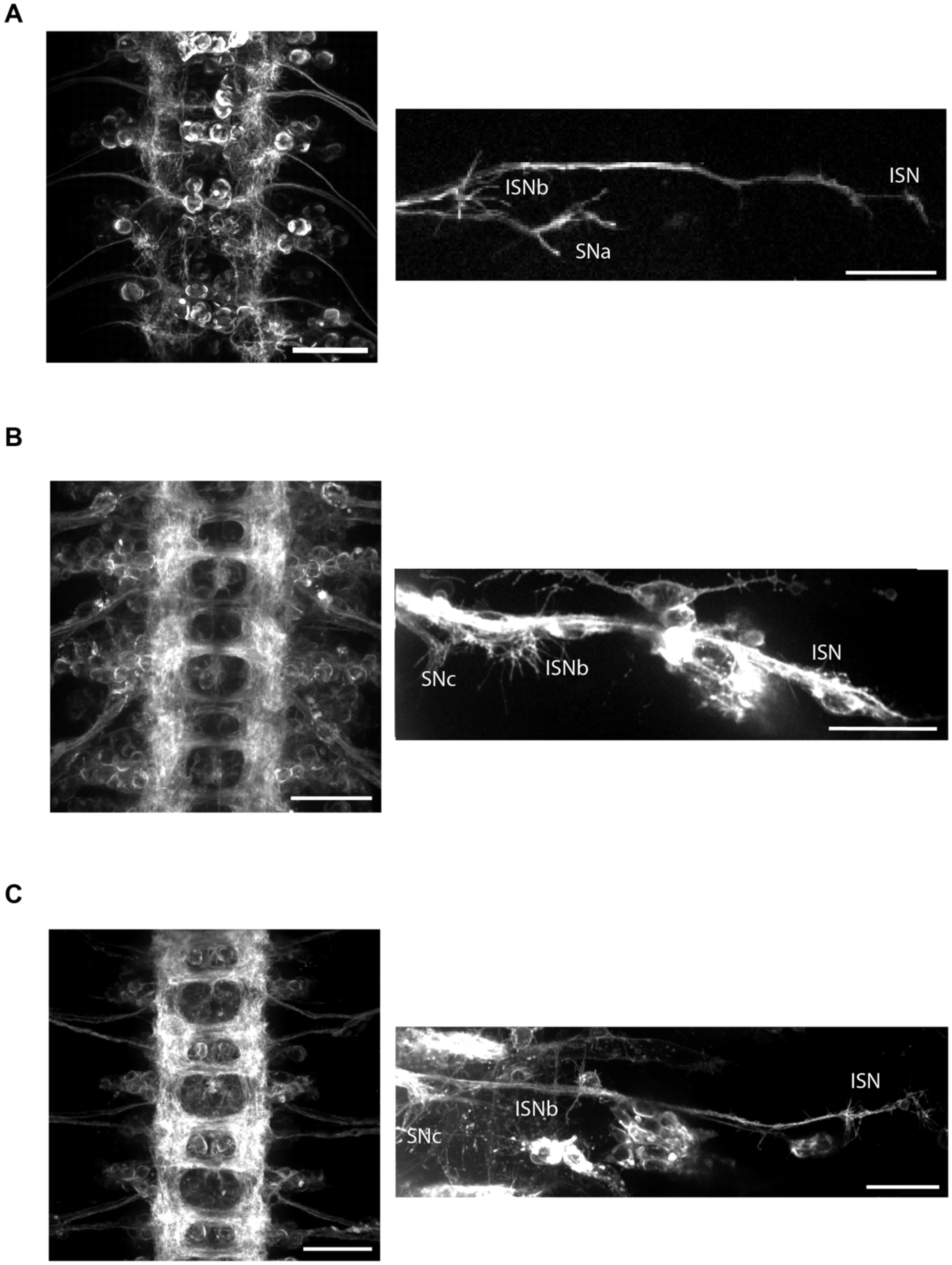

Figure 4.4 *LexA* drivers that have activity in motor neurons during stage 16.

Left panels demonstrate activity in the ventral nerve cord and the right panels demonstrate activity in the body wall. Major identifiable nerve tracks are labeled with text. Scalebar: 20 µm **(A)** *VGlut-*

LexA was live imaged and visualized with *LexAop2-CD4::tdTomato*. **(B)** R11D01-LexA was visualized with *LexAop2-CD4::GFP* after fixation. This line doesn't have frequent leaky activity in musculature but has sensory nervous system activity, which is further characterized in Figure S4.2. **(C)** *R45B10-LexA* was visualized with *LexAop2-CD4::GFP* after fixation. The ventral regions show weak muscle expression along with other cell activities.

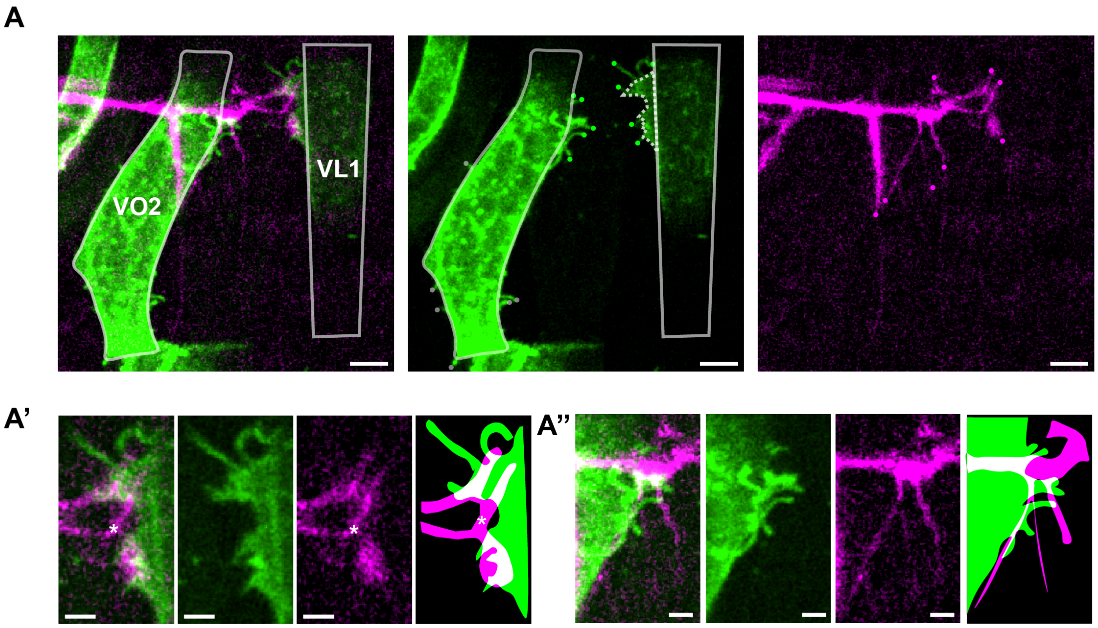

Figure 4.5 VO2 and VL1 muscles are visualized in living tissue before contractile activity in muscles (~15:30 h AEL).

Genotype: *VGlut-LexA, LexAop2-CD4::tdTomato/+; R11H11-Gal4, UAS-CD4::tdGFP*.

(A) 2-color projection of a single timepoint from Movie 4.2 (02:40 minutes). Left to right: Merged image, muscle only, neuron only. The tips of axon branches are emphasized with magenta dots and muscle filopodia are emphasized with green (if found at the contact interface with the neuron) or gray (if found outside of contact interface). The dotted line in VL1 masks the sheet-like structure observed. Scalebar: 5 µm. **(A', A'')** Magnified muscle neuron interaction site. Left to right: merged, muscle only, neuron only, cartoon tracing. Scalebars: 2 µm. **(A')** Sheet-like structure at VL1. At VL1 muscle edge, there is a 2-peak sheet-like structure with filopodia protruding from various sites on the surface. The asterisk (*) denotes the bifurcation point of MN12 which also coincides with the trough of the sheet-like structure. **(A'')** Filopodia clustering at VO2. At the contact interface of VO2 and ISNb, there are multiple filopodia protruding from VO2 and interacting with various axon terminals, including that which innervates VO2 (MN14, embryonic counterpart unknown) as well as the axon bundle passing by VO2.

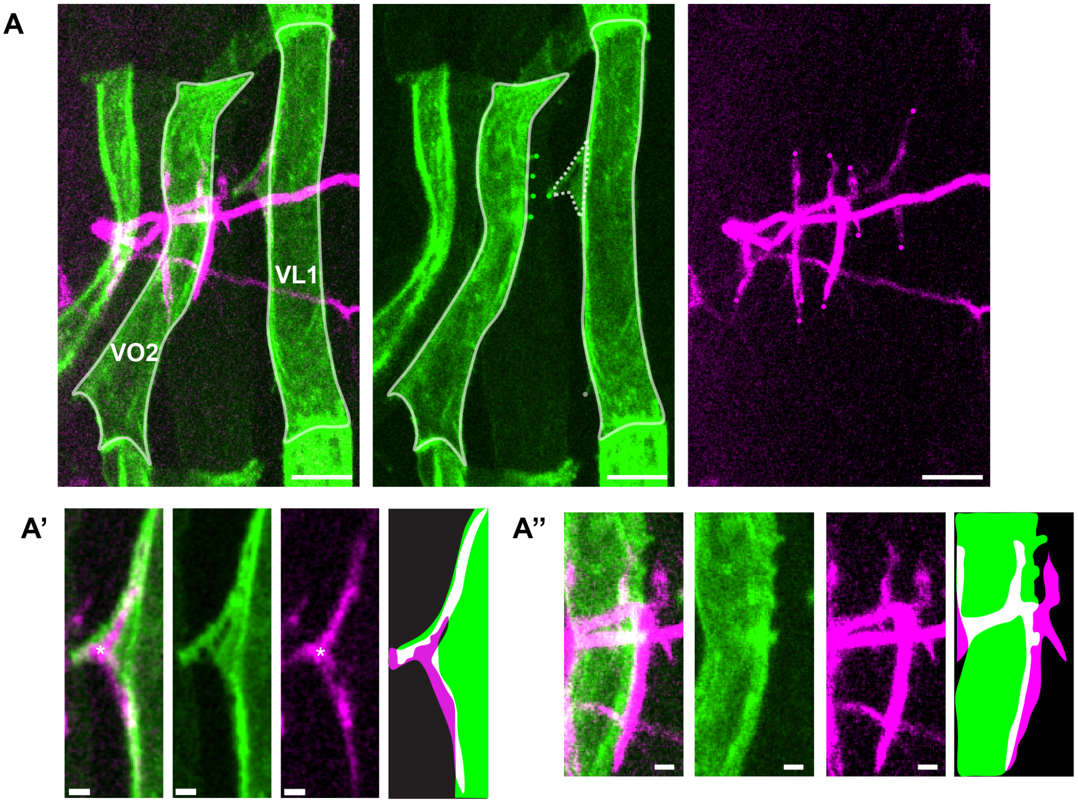

Figure 4.6 VO2 and VL1 muscles are visualized in living tissue after contractile activity in muscles (16:30 h AEL).

Genotype: *VGlut-LexA, LexAop2-CD4::tdTomato/+; R11H11-Gal4, UAS-CD4::tdGFP.*

(A) 2-color projection of a single timepoint from Movie 4.3 (20:00 minutes). Left to right: Merged image, muscle only, neuron only. The tips of axon branches are emphasized with magenta dots, muscle ridges (VO2) and filopodia (VL1) are emphasized with green dots (at the contact interface), filopodia-like structure on VL1 found outside of contact interface is in gray dot. The dotted line in VL1 masks the sheet-like structure observed. Scalebar: 10 µm. (**A’, A’’**). Magnified muscle neuron interaction site. Left to right: merged, muscle only, neuron only, cartoon tracing. ISN and SNa nerve are omitted from the cartoon tracing for simplification of the NMJ visualization. Scalebars: 2 µm. **(A’)** Sheet-like structure at VL1. The sheet-like structure has a single peak. The sheet has an unfilled region between a filopodia-like membrane protrusion and the remainder of the sheet-like structure. The asterisk (*) denotes the bifurcation point of MN12. The bifurcation point of MN12 coincides with the peak of the sheet-like structure. **(A'')** Membrane ridges on the VO2 surface near the interaction interface. There are four ridges on VO2 near the interaction site making contact primarily with the MN14. While MN13 terminal is also proximal to the ridges, they do not seem to make a contact with VO2.

4.10 SUPPLEMENTARY FIGURES

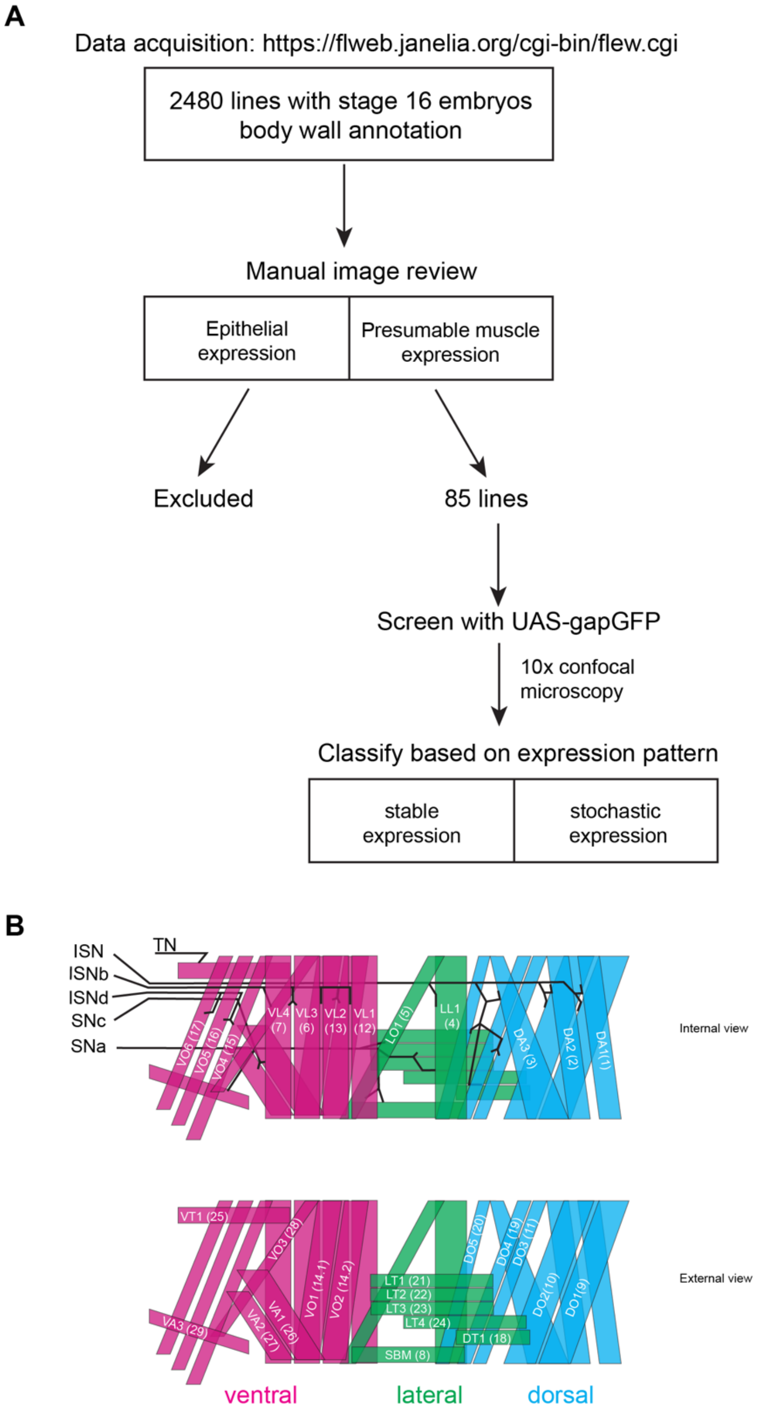

Supplementary Figure 4.1 Screening and characterization pipeline of Gal4 drivers.

(A) Previously available datasets were acquired through the Flylight image database. Images of 2480 *Gal4* drivers at embryonic stage 16 with body wall annotations were reviewed manually to assess for segmentally distinct expressions which may indicate muscle activity. 85 candidate drivers were screened using a membrane targeted GFP (*UAS-gapGFP*) with 10x confocal microscopy in filleted stage 16 embryos. The hits with subsets of muscle expressions were characterized into two groups. The stable expression group represented drivers with consistent muscle expression patterns while stochastic expression group represented those drivers with variable expression of individual muscles. **(B)** Internal and external schematic views of musculature. Top: Internal view of musculature with the innervation pattern of each nerve. Nerve tracks are labeled on the left side of the schematic. Only the internal muscles are labeled. Bottom: External view of the musculature where external muscles are labeled separately from the internal muscles. Musculature is colored based on the defined groupings in the main text: ventral in magenta, lateral in green and dorsal in cyan.

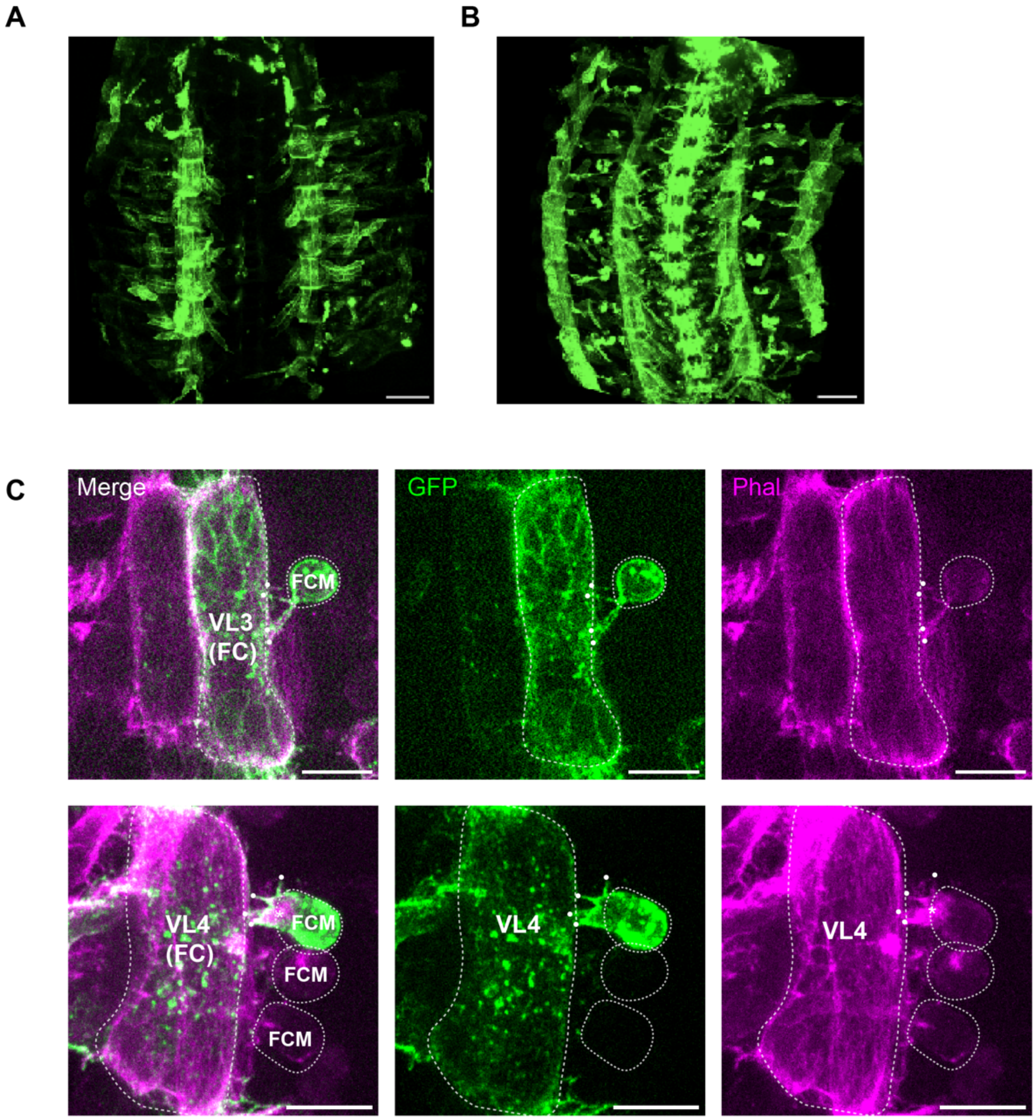

Supplementary Figure 4.2 Embryonic expression patterns of stochastic *Gal4* drivers.

(A) *R23B04-Gal4* and **(B)** *R28E05-Gal4* crossed to *UAS-CD4::tdGFP* was filleted as stage 16 embryo and immuno-stained with anti-GFP. Scalebar: 50 µm. **(C)** Late stage 15 *R23B04-Gal4* muscle fusion events of single muscles. Top: Fusion between VL3 FC and FCM. Bottom: Fusion between VL4 FC and FCM. The FCs and FCM bodies are outlined in dotted line. The PLS tips are denoted with white points. Asterisk in the bottom panel demonstrates the actin foci during fusion. GFP: anti-GFP immunostain; Phal: phalloidin, F-actin marker. Scalebar: 20 µm.

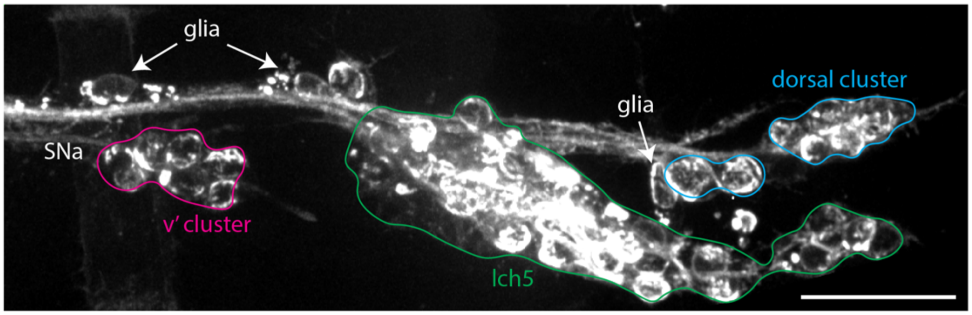

Supplementary Figure 4.3 Cell types active in the body wall in *R11D01-LexA*.

Using the exclusion of anti-HRP (for detecting sensory and motor neurons) and anti-Fas2 (for detecting motor neurons only), we found there were additional cells that were GFP positive. In the ventral region, one of the 3 exit glia appears to have activity, while also present is activity of sensory neurons along the SNa tract (v' cluster neurons; magenta outline). Most of the sensory neuron activity is observed in the lateral cluster cells, including the chordotonal organ (lch5; green outline). There is also activity in peripheral glia found near this sensory neuron cluster as well as lbd (not labeled in this figure) and its associated glia (white arrows). Finally, a small subset of the dorsal cluster of the sensory neurons has activity (blue outline).

4.11 SUPPLEMENTARY TABLE

Supplementary Table 4.1 List of *Gal4* and *LexA* drivers summarized with associated gene and expression pattern.

Line ID	BDSC Stock Number	Enhancer activity associated gene (gene symbol)	Expression pattern
R27F08	49232	*Limpet (Lmpt)*	Ventral muscles
R33E02	49751	*Src oncogene at 64B (Src64B)*	Ventral muscles
R15F04	47866	*single-minded (sim)*	Ventral muscles
R11H11	48480	*Guanylyl cyclase β-subunit at 100B (Gycbeta100B)*	Ventral + Dorsal muscles
R48D05	50362	*defective proboscis extension response 10 (dpr10)*	Ventral + Dorsal muscles
R40A07	50074	*apterous (ap)*	Lateral muscles
R31F06	49684	*Ultrabithorax (Ubx)*	Broad
R9H06	47439	*twin of eyeless (toy)*	Stochastic
R23B04	49016	*fruitless (fru)*	Stochastic
R28E05	49459	*Dscam1 (Down syndrome cell adhesion molecule 1)*	Stochastic
VGlut-LexA	60314	Not applicable; Gene-trap	Motor neuron *LexA*
R11D01	52430	*bifid (bi)*	Motor neuron + PNS *LexA*
R45B10	53646	*pointed (pnt)*	Motor neuron + PNS *LexA*

4.12 METHODS

Drosophila lines

All *Gal4* lines and *LexA* lines identified in this study are listed in **Table S4.1**. Reporter lines were: *5x UAS-GAP::GFP* (gifted by Carlos Lois) was used for screening Gal4 activity, *UAS-CD4::tdGFP* (RRID: BDSC_35836) was used for higher magnification characterization of the stochastic Gal4 drivers and live imaging experiments. *LexAop2-CD4::tdGFP* (RRID: BDSC_77176) was used for screening the *LexA* drivers. *LexAop2-CD4::tdTomato* (RRID: BDSC_77178) was used for imaging *VGlut-LexA*. Flies were reared at 25ºC, and staging have been determined at this temperature based on hours after egg laying and morphological criteria described by Campos-Ortega and Hartenstein (1997).

Dissection and immunohistochemistry

Embryonic dissections and immunostaining were performed as previously described (Inal Current Protocols). For screening, fillet-dissected stage 16 embryos were fixed with 4% paraformaldehyde (EMS) for 5 minutes at room temperature and counter-stained with 1:100 anti-HRP conjugated with Cy3 (data not shown; JacksonImmuno Research, RRID: AB_2338959). For characterization of stochastic Gal4 drivers and the new LexA driver crossed to GFP reporter line, further immunostaining was performed. Following fixation, the sample was washed with PBS/0.01% Triton X-100 (TBS) and blocked for 1 hour at room temperature (RT) in PBS/0.01% Triton X-100 with 0.06% BSA (TBSB). Primary antibodies were diluted in TBSB, and embryos were incubated overnight in 4ºC. The Gal4 samples were incubated in monoclonal rabbit anti-GFP (1:200; Thermo-Fisher, RRID: AB_2536526), and LexA driver was incubated with monoclonal mouse anti-Fas2 (1:50; DSHB_1D4, RRID: AB_528235). Next day, secondary antibodies were incubated for 2 hours at RT. The *Gal4* samples were incubated with donkey anti-Rabbit Alexa Fluor 488

(1:200; Thermo-Fisher, RRID: AB_2535792) and TRITC- phalloidin (1:500; Sigma, P1951). The *LexA* samples were incubated in donkey anti-mouse IgG-AF647 (1:200; Thermo-Fisher, RRID: AB_162542) and anti-HRP Cy3 (1:200). Following immunohistochemistry samples were washed and mounted in TBS.

Confocal microscopy

Confocal microscopy images of fixed filleted embryos were captured using an inverted fluorescence microscope (Ti-E, Nikon) with either 10× 0.30 NA air objective, 40× 0.80 NA water immersion objective or 100× 1.45 NA oil immersion objective (Nikon). For live imaging timelapse movies were acquired under 40× 1.25 NA silicone immersion objective (Nikon). The microscope was attached to the Dragonfly Spinning disk confocal unit (CR-DFLY-501, Andor). Three excitation lasers (40 mW 488 nm, 50 mW 561 nm, and 110 mW 642 nm lasers) were coupled to a multimode fiber passing through the Andor Borealis unit. A dichroic mirror (Dragonfly laser dichroic for 405-488-561-640) and three bandpass filters (525/50 nm, 600/50 nm, and 725/40 nm bandpass emission wheel filters) were placed in the imaging path. Images were recorded with an electron-multiplying charge-coupled device camera (iXon, Andor).

Image processing

Images were processed in ImageJ (NIH) to improve brightness and contrast. To smooth for the background artifacts in live movies, a Gaussian blur (0.5) was applied. Images for stochastic Gal4 drivers were taken using 40× objective and stitched together in ImageJ using the Grid/Collection stitching plugin (Preibisch et al., 2009). Due to embryonic movement as a result of rolling behavior, the movie was stabilized using Linear Stack Alignment with SIFT multichannel plugin. Using a translation transformation, the motor neuron channel was set as the registration channel for the correction (Lowe, 2004). Region of interests for Figures 5 and 6 were generated using the

Biovoxxel Figure Tools plugin (Jan Brocher & mutterer, 2024). Figures were curated using Adobe Illustrator 2025 (Adobe).

Heatmap generation of *Gal4* activity

Each muscle's expression in single segments (A1-A6) across 5 embryos were counted for each driver. The frequency of expression was split into 10 percent bins. The heatmap was generated using a custom Python script with "greens" colormap from the seaborn package.

4.13 REFERENCES

Ashley, J., Sorrentino, V., Lobb-Rabe, M., Nagarkar-Jaiswal, S., Tan, L., Xu, S., Xiao, Q., Zinn, K., & Carrillo, R. A. (2019). Transsynaptic interactions between IgSF proteins DIP-α and Dpr10 are required for motor neuron targeting specificity. *eLife*, *8*, e42690. https://doi.org/10.7554/eLife.42690

Baylies, M. K., Bate, M., & Gomez, M. R. (1998). Myogenesis: A View from Drosophila. *Cell*, *93*(6), 921–927. https://doi.org/10.1016/S0092-8674(00)81198-8

Beckett, K., & Baylies, M. K. (2007). 3D analysis of founder cell and fusion competent myoblast arrangements outlines a new model of myoblast fusion. *Developmental Biology*, *309*(1), 113–125. https://doi.org/10.1016/j.ydbio.2007.06.024

Campos-Ortega, J. A., & Hartenstein, V. (1997). *The Embryonic Development of Drosophila melanogaster*. Springer Berlin Heidelberg. https://doi.org/10.1007/978-3-662-22489-2

Crisp, S., Evers, J. F., Fiala, A., & Bate, M. (2008). The development of motor coordination in *Drosophila* embryos. *Development*, *135*(22), 3707–3717. https://doi.org/10.1242/dev.026773

Dobi, K. C., Schulman, V. K., & Baylies, M. K. (2015). Specification of the somatic musculature in *Drosophila*. *WIREs Developmental Biology*, *4*(4), 357–375. https://doi.org/10.1002/wdev.182

Halpern, M., Chiba, A., Johansen, J., & Keshishian, H. (1991). Growth cone behavior underlying the development of stereotypic synaptic connections in Drosophila embryos. *The Journal of Neuroscience*, *11*(10), 3227–3238. https://doi.org/10.1523/JNEUROSCI.11-10-03227.1991

Hammonds, A. S., Bristow, C. A., Fisher, W. W., Weiszmann, R., Wu, S., Hartenstein, V., Kellis, M., Yu, B., Frise, E., & Celniker, S. E. (2013). Spatial expression of transcription factors in Drosophilaembryonic organ development. *Genome Biology*, *14*(12), R140. https://doi.org/10.1186/gb-2013-14-12-r140

Inal, M. A., Bui, K. C., Marar, A., Li, S., Kner, P., & Kamiyama, D. (2021). Imaging of In Vitro and In Vivo Neurons in *Drosophila* Using Stochastic Optical Reconstruction Microscopy. *Current Protocols*, *1*(7), e203. https://doi.org/10.1002/cpz1.203

Jan Brocher, & mutterer. (2024). *biovoxxel/BioVoxxel-Figure-Tools: BioVoxxel Figure Tools - v4.0.0* (Version bvft-4.0.0) [Computer software]. Zenodo. https://doi.org/10.5281/ZENODO.7268127

Kohsaka, H., & Nose, A. (2009). Target recognition at the tips of postsynaptic filopodia: Accumulation and function of Capricious. *Development*, *136*(7), 1127–1135. https://doi.org/10.1242/dev.027920

Kohsaka, H., Takasu, E., & Nose, A. (2007). In vivo induction of postsynaptic molecular assembly by the cell adhesion molecule Fasciclin2. *The Journal of Cell Biology*, *179*(6), 1289–1300. https://doi.org/10.1083/jcb.200705154

Landgraf, M., Bossing, T., Technau, G. M., & Bate, M. (1997). The Origin, Location, and Projections of the Embryonic Abdominal Motorneurons of *Drosophila*. *The Journal of Neuroscience*, *17*(24), 9642–9655. https://doi.org/10.1523/JNEUROSCI.17-24-09642.1997

Lowe, D. G. (2004). Distinctive Image Features from Scale-Invariant Keypoints. *International Journal of Computer Vision*, *60*(2), 91–110. https://doi.org/10.1023/B:VISI.0000029664.99615.94

Mahr, A., & Aberle, H. (2006). The expression pattern of the Drosophila vesicular glutamate transporter: A marker protein for motoneurons and glutamatergic centers in the brain. *Gene Expression Patterns*, *6*(3), 299–309. https://doi.org/10.1016/j.modgep.2005.07.006

Manning, L., Heckscher, E. S., Purice, M. D., Roberts, J., Bennett, A. L., Kroll, J. R., Pollard, J. L., Strader, M. E., Lupton, J. R., Dyukareva, A. V., Doan, P. N., Bauer, D. M., Wilbur, A. N., Tanner, S., Kelly, J. J., Lai, S.-L., Tran, K. D., Kohwi, M., Laverty, T. R., … Doe, C. Q. (2012b). A Resource for Manipulating Gene Expression and Analyzing cis-Regulatory Modules in the Drosophila CNS. *Cell Reports*, *2*(4), 1002–1013. https://doi.org/10.1016/j.celrep.2012.09.009

Pfeiffer, B. D., Jenett, A., Hammonds, A. S., Ngo, T.-T. B., Misra, S., Murphy, C., Scully, A., Carlson, J. W., Wan, K. H., Laverty, T. R., Mungall, C., Svirskas, R., Kadonaga, J. T., Doe, C. Q., Eisen, M. B., Celniker, S. E., & Rubin, G. M. (2008). Tools for neuroanatomy and neurogenetics in *Drosophila*. *Proceedings of the National Academy of Sciences*, *105*(28), 9715–9720. https://doi.org/10.1073/pnas.0803697105

Preibisch, S., Saalfeld, S., & Tomancak, P. (2009). Globally optimal stitching of tiled 3D microscopic image acquisitions. *Bioinformatics*, *25*(11), 1463–1465. https://doi.org/10.1093/bioinformatics/btp184

Ritzenthaler, S., Suzuki, E., & Chiba, A. (2000b). Postsynaptic filopodia in muscle cells interact with innervating motoneuron axons. *Nature Neuroscience*, *3*(10), 1012–1017. https://doi.org/10.1038/79833

Rose, D., & Chiba, A. (2000). Synaptic target recognition at Drosophila neuromuscular junctions. *Microscopy Research and Technique*, *49*(1), 3–13. https://doi.org/10.1002/(SICI)1097-0029(20000401)49:1<3::AID-JEMT2>3.0.CO;2-E

Tomancak, P., Beaton, A., Weiszmann, R., Kwan, E., Shu, S., Lewis, S. E., Richards, S., Ashburner, M., Hartenstein, V., Celniker, S. E., & Rubin, G. M. (2002). Systematic determination of patterns of gene expression during Drosophila embryogenesis. *Genome Biology*, *3*(12), research0088.1. https://doi.org/10.1186/gb-2002-3-12-research0088

Tomancak, P., Berman, B. P., Beaton, A., Weiszmann, R., Kwan, E., Hartenstein, V., Celniker, S. E., & Rubin, G. M. (2007). Global analysis of patterns of gene expression during Drosophila embryogenesis. *Genome Biology*, *8*(7), R145. https://doi.org/10.1186/gb-2007-8-7-r145

CHAPTER 5

MUSCLE FILOPODIA HAVE DISTINCT COMPARTMENTALIZATION AND FUNCTIONS FOR NORMAL CIRCUIT DEVELOPMENT[4]

---

[4] Inal, M.A., Li, S., Kner, P.A. and Kamiyama, D. To be submitted to *Development.*

5.1 ABSTRACT

During neuromuscular circuitry development, muscles extend numerous filopodia on their surface mediating contacts with motor neurons. In this study, we found that filopodia in muscle 12 (M12) show two distinct sites of increased activity, corresponding to interaction sites with ISNb and SNa neurons. Using structural illumination microscopy, we characterized the morphological traits of muscle filopodia including their lengths, widths and interactions. We found that the number of filopodia interactions differentiate the two hotspots of filopodia activity in determining where the synapse will form. Next, we used constitutively active form of an actin-regulating GTPase Cdc42^{V12} overexpression in M12 to knock down filopodia activity and we found guidance, targeting, and synaptogenesis in both ISNb and SNa are altered while defasciculation decisions were also altered in SNa. Here, we propose the filopodia on muscle contribute to refinement of motor circuit by participating in multiple roles in distinct subcellular compartments.

5.2 INTRODUCTION

The assembly of functional neural circuits requires that motor neurons not only reach appropriate target domains but also identify specific partner cells for synapse formation. In the developing neuromuscular system of *Drosophila melanogaster*, this intricate process is orchestrated through tightly regulated temporal and spatial cues, many of which remain poorly understood. While previous work has mapped the gross trajectories of motor axons and identified guidance cues at early developmental choice points (Arzan Zarin & Labrador, 2019; Jeong, 2021; Nose, 2012), the mechanisms by which synaptic specificity is achieved at the level of individual muscle fibers are still emerging.

A growing body of research suggests that the muscle is not merely a passive recipient of innervation but plays an active role in partner selection and synaptogenesis. One of the most striking demonstrations of this is the presence of actin-rich protrusions, or filopodia, on both the presynaptic growth cone and the postsynaptic muscle surface (Kohsaka & Nose, 2009; Ritzenthaler et al., 2000; Suzuki et al., 2000). These filopodia dynamically extend and retract to explore the surrounding environment, providing a physical substrate for cell-cell contact, recognition, and potential signaling exchange. On the muscle side, such structures—often referred to as myopodia—appear during the critical window of synapse formation and have been hypothesized to facilitate partner matching and synaptic stabilization (Carrero-Martínez & Chiba, 2009; Nose, 2012).

Despite their structural similarity, it is unknown whether all filopodia on a single muscle fiber contribute equally to synaptogenesis. For example, muscle 12 (M12) is a well-characterized target of the RP5 motor neuron (MN12), forming a robust synapse at its anteroventral domain (Halpern et al., 1991; Hoang & Chiba, 2001). However, the same muscle also lies along the path of the segmental nerve a (SNa), particularly the MN5/8 sub-branch, raising the possibility that it engages in additional, perhaps non-synaptic, interactions. Whether these interactions are functionally distinct, and how the muscle's filopodial landscape contributes to their outcomes, remains an open question.

In this study, we set out to address whether spatially localized muscle filopodia correspond to distinct motor neuron interactions and whether they differ in their morphology, dynamics, or capacity to support synapse formation. Using a combination of live imaging, dual-labeling strategies, and super-resolution microscopy, we first map the filopodial activity landscape of M12 during late embryogenesis. We identify two hotspots of activity—one at the canonical MN12 synapse site and another on the posterior surface that opposes the MN5/8 branch of SNa.

We then assess whether these two filopodia populations lead to distinct outcomes. We find that while both engage motor axons, only the anterior site leads to synapse formation, as evidenced by glutamate receptor clustering and Dlg accumulation. Interestingly, the non-synaptic interaction at the posterior site precedes the synaptic interaction temporally, suggesting a guidance or checkpoint role. Using morphometric analysis and filopodia quantification, we show that filopodia at both sites are similar in size and number but differ in the extent of their contacts with motor axons. Furthermore, genetic disruption of filopodia via overexpression of constitutively active Cdc42 in M12 leads to aberrant axon pathfinding and reduced synapse formation, underscoring the instructive role of muscle filopodia.

Taken together, our results demonstrate that muscle filopodia are not homogenous structures but can be functionally specialized within the same cell. These findings suggest that postsynaptic filopodia contribute not only to synaptic partner matching but also to guidance decisions that shape the architecture of the neuromuscular circuit. This work extends our understanding of how subcellular structures mediate developmental precision and highlights the muscle's active role in defining the connectivity of the motor system.

5.3 RESULTS

Filopodial activity of M12

Since muscle filopodia are found broadly throughout and become localized during motor neuron interactions **(Fig 5.1A)**, we characterized the filopodia activity on M12 during stage 16 (13:00-15:00 h AEL) to determine whether other distinct filopodia populations exist. For this, we imaged filleted embryos expressing membrane bound GFP (CD4::tdGFP) in M12 and immunostained them to enhance the fluorescence signal **(Fig. 5.1B)**. We then generated a heatmap of activity by splitting the muscle into 16 equal bins in total and counted the number of filopodia found in each bin (**Fig. 5.1B, C** and **Table 5.1**). Interestingly, we observed two distinct sites of increased filopodia activity. First, as reported previously, we found high levels of filopodia activity in the anteroventral bins of the M12, covering about 50% of the muscle height. The bin with the highest filopodia activity was found in the 25.0-37.5% bin from the anterior of the muscle with an average of 3.1 ± 0.52 (mean ± SEM) filopodia in this area, similar to previously reported activity (**Fig. 5.1C** and **Table 5.1**) (Ritzenthaler et al., 2000). The second site of increased filopodia activity corresponded to a single bin in the posterodorsal region of the muscle at the 75.0-87.5% bin. On average there were 2.3 ± 0.85 filopodia in this bin. The remainder of the bins averaged to a range of 0.5-1.4 filopodia. Altogether, these results suggest that there are two distinct sites of filopodia activity during stage 16 in M12.

M12 filopodia interact with MN12 and the MN5/8 branch of SNa

During guidance, motor nerves make stereotyped decisions to reach their target muscles. The ISNb nerve, which targets M12, first defasciculates from ISN and enters the ventral target domain. Later, individual motor neurons defasciculate from one another to survey and innervate their ventrolateral target muscles (Krueger et al., 1996). Similarly, SNa enters its target domain just after passing M12, splitting into two pathways to form the posterior (e.g., MN5/8) and dorsal branches (e.g. MN21-24) (Chiba, 1999; Kaufmann et al., 1998).

Because of this axonal trajectory, we suspected that the filopodia activity sites might correspond to ISNb interaction site in the anterior site and an SNa interaction site in the posterior site. Indeed, upon co-staining the muscle with a neuronal membrane marker, we found that both hotspots corresponded to interaction site with motors neurons (**Fig. 5.2A**). While ISNb contacted M12 on the anteroventral filopodia site (**Fig. 5.2A**, inset i), the MN5/8 apposed the second filopodial hotspot on the posterior domain of M12 (**Fig. 5.2A**, inset ii).

To further confirm the colocalization of the axon terminals and the muscle filopodia were a product of their interaction, we used two orthogonal binary expression systems, *UAS/Gal4* and *LexAop/LexA* to label M12 and motor neurons using membrane targeted FPs (**Movies 5.1** and **5.2**). With live imaging, we were able to observe that filopodia activity on the anteriomedial site dynamically resulted in tight interactions close to the edge of the muscle body, an indication of filopodia clustering events (**Fig. 5.2B**). On the other hand, we observed that filopodia from the posterior domain of M12 interacted with the posterior MN5/8 branch of the SNa (**Fig. 5.2C**). Particularly, multiple filopodia from the muscle were reaching to SNa and appeared to be pulling the branch in a posterior direction (**Movie 5.2**). Altogether these results suggest that M12 interacts through filopodia with two distinct motor neuron groups at two unique sites on the muscle surface.

Distribution of synapses

Previous studies have placed embryonic and larval synapses of M12 at the MN12 interaction site at the anterio-ventral edge (Halpern et al., 1991; Hoang & Chiba, 2001). However, the interaction site of M12 with SNa branch has not been investigated for possible transient synapse localization during embryonic development. Since the NMJs are glutamatergic, we decided to assess the localization of glutamate receptors using an antibody specific to the IIA subunit. During embryonic development, glutamate receptors' enrichment cannot be detected by immunostaining until 18:00 h AEL (Marrus et al., 2004). Thus, we investigated the receptor localization in both sites from 18:00-19:00 h AEL. Interestingly, we were able to observe punctate structures accumulate near the MN12 interaction site, though we cannot clearly conclude whether this accumulation is NMJ-specific (**Fig. 5.3A'-A''**). Thus, we opted to use a marker for post-synaptic density, anti-Dlg antibody, which localizes strongly to the synaptic sites in late embryogenesis (**Fig. 5.3B, B'**). In conjunction with the pan-neuronal antibody, we were able to mark the site of interaction and the nascent synapse. Although this protein is localized in both pre- and post-synapses, the spatial separation of the SNa motor neuron from the muscle provided sufficient resolution to assess the localization of the synapses at M12 (**Fig. 5.3B**). Here, we found that in late embryos or larval stages, M12 does not have a second synaptic site corresponding to the interaction site of SNa (**Fig. 5.3B''**). These results suggest that filopodia interaction with two distinct neurons have different outcomes: a synapse forms through filopodia that interact with MN12 (referred to as synaptic filopodia, hereafter), while no synapse is formed through filopodia that interact with SNa (referred to as non-synaptic filopodia, hereafter).

Timeline of filopodia interactions in M12

Interestingly, the filopodia interaction between M12 and SNa did not result in a synapse (**Fig. 5.3B''**), suggesting a potentially different role of interaction at this site. Since the timing of interaction during synaptic formation occurs in synchrony across the musculature, we reasoned timing of interactions may provide insight into the functions of the filopodia. For instance, if the interactions have different roles during neuromuscular circuit development, then their timing may be different. Therefore, we dissected embryos between 12:00-14:00 h AEL and looked at filopodia based interactions (**Fig. 5.4**).

By the time M12 completes its fusion events preparing for the anterior/posterior ends to reach the tendon cells for insertion into the epithelia, SNa has already crossed to the distal side of M12 (**Fig. 5.4A-A''**, 12:00). During this time, ISNb extends from the nerve cord making initial contacts with the proximal targets M7/6 (data not shown) (Halpern et al., 1991). Although M12 has filopodia activity in the medial side of the muscle, this activity compared with later stages of filopodia activity upon the onset of MN12 interaction is not localized (**Fig. 5.4A-A''**, 13:30). On the other side, SNa makes interactions with filopodia comparable to the levels observed at 13:30

h AEL (**Fig. 5.4A-A''**, 13:30). At 14 hours and beyond, the synaptic interaction is increased through accumulation of filopodia at the contact site, while non-synaptic filopodia activity is ceased and the posterior SNa branch is placed against the edge of the muscle as it reaches towards muscles 5/8 (**Fig. 5.4A-A''**, 14:00). Altogether, these observations suggest that the difference in the roles between synaptic and non-synaptic filopodia may arise from their differences in timing.

Characterization of filopodia

How could one cell with presumably same protrusions in distinct locations establish only a single synapse? So far, our observations suggest that interaction between neuron and muscle filopodia is not sufficient to make a synapse. Thus, we asked: can morphological differences between synaptic and non-synaptic filopodia explain where synaptogenesis may occur? Since the filopodia contact on M12 on both sites occurs at 13:30 h AEL, this is the developmental time point we further characterize the filopodia (**Fig. 5.4A-A''**). First, we asked if the morphological characteristics of muscle filopodia distinguish the two sides from being able to form synapses. For this we measured the lengths and widths of filopodia found on muscle using super-resolution imaging. Since the widths of the filopodia can be below the diffraction limit of light, we opted to use structural illumination microscopy (SIM), in conjunction with immunofluorescence of the cell membranes (**Fig. 5.5A-B**). We first measured the lengths of filopodia from the tip to the edge of the muscle and found that there were no statistically significant differences: 4.163 ± 0.262 μm on the synaptic side and 3.542 ± 0.368 μm on the non-synaptic side **(Fig. 5.5C**).

Next, we measured the widths of filopodia in both groups. For this, we averaged the widths of filopodia along their lengths at 70 nm increments and compared the mean widths between synaptic and non-synaptic sites (**Fig. 5.5D'**). Similarly, we found there to be no difference between 124.70 ± 1.124 nm synaptic, 124.98 ± 1.28 nm and non-synaptic widths (**Fig. 5.5D**).

Characterization of M12 interactions

Our observations so far failed to reveal obvious differences in morphology of filopodia, suggesting that the dynamic interactions between the neuron and the muscle may be different. We hypothesized that if filopodia-based interactions will initiate synaptogenesis, then they must be able to surpass a specific threshold that results in a positive feedback loop and increases the numbers of filopodia interactions as synaptogenesis begins. To test this, we quantified filopodia interactions, defined as parallel contacts between the neuron and the muscle for at least 125 nm (based on the average width of the filopodia: 124.70-124.98) (**Fig. 5.5E and F**). We compared the number of interactions MN12 makes to the MN5/8 interactions. We found that the synaptic filopodia make on average 6.0 ± 0.7 interactions while the non-synaptic filopodia are involved in 2.3 ± 0.2 interactions (**Fig. 5.5G**). Thus, the number of non-synaptic interactions was limited (between 1-4 interactions) while synaptic number of interactions had a larger range (between 2-12 interactions).

Disruption of filopodia using UAS-cdc42^{V12}

Filopodia interactions appeared to be an important factor in synaptogenesis. To test the role of filopodia in synaptogenesis, we aimed to eliminate the filopodia activity. Since actin depolymerizing drugs like Cytochalasin D have a broad impact on all cells, including both neuron and muscle processes, we opted to target filopodia using genetic manipulations. For this, we conducted a small screen of actin-related proteins with the *UAS/Gal4* system (details in methods). Surprisingly, we found that the overexpression of a constitutively active mutant of Cdc42 (cdc42^{V12} OE hereafter) led to a significant loss of filopodia in M12 (n= 42 muscle) (**Fig. 5.6A**). This loss of filopodia resulted in two distinct aberrant phenotypes in 80% of the M12 NMJs: stalling (70%) and overshooting of the MN12 (10%) (**Fig. 5.6D**). We found that upon cdc42^{V12}

OE, the overall number of filopodia was significantly reduced: control 43 ± 2.136 vs. cdc42^{V12} OE 22.79 ± 1.629 (**Fig. 5.6B**). To compare the distribution of the filopodia activity, we regenerated a filopodia heatmap, this time specific to 13:30 h AEL (**Fig. 5.6C**). We compared the changes of filopodia activity in each of the bins and found that both filopodia activity sites showed a significant loss of filopodia activity (**Fig. 5.6C**, asterisks).

In addition to loss of filopodia on the muscle, we observed an increased filopodia activity on the axon terminal (**Fig. 5.6D**). To confirm this observation, we counted the number of growth cone filopodia. Since filopodia can reach past lengths equivalent to the diameter of its neighboring muscles, we measured the filopodia activity of ISNb within a diameter of M12 in the given segment. Indeed, we found that the growth cone of ISNb terminal in cdc42^{V12} OE had 4.389 ± 1.501 more filopodia than control (**Fig. 5.6E**). These results suggest that loss of filopodia activity on muscle leads to an increase of filopodia activity in the partner neuron, near the neuromuscular contact field.

Since neurons use filopodia at their terminal to sense and guide the axon, we wondered whether the changes in the muscle filopodia activity led to changes in axon's steering. For this we used a grid system and split the anterior-posterior axis into 8 bins and counted the number of filopodia within each bin from ISNb for the placements of ISNb filopodia. Interestingly, we observed an increase of MN filopodia activity in the 0-12.5% bin near the anterior segmental border (Mann-Whitney test; p= 0.0071) (**Fig. 5.6F**). This suggests that the loss of filopodia activity on the muscle may affect the pre-synaptic growth cone behavior. To see downstream consequences of filopodia loss, we looked at larval NMJs and counted the numbers of Dlg-positive boutons on M12 (**Fig. 5.6G**). We found that in cdc42^{V12} OE muscles (7.07 ± 0.47), there were less boutons compared with control (11.23 ± 0.40), suggesting that loss of filopodia activity may lead to smaller number of synaptic structures (**Fig. 5.6G-H**).

Non-synaptic effects of cdc42^{V12} OE

Next, we investigated the effects of filopodia loss in non-synaptic roles, such as axon guidance, and non-target synaptic development. We reasoned since the filopodia do not play a role in synaptogenesis, an alternative role for those filopodia may be to guide the axon, also supported by our observations with ISNb. Therefore, we focused on changes in SNa guidance and development upon interaction with M12.

First, we measured the exit site of SNa from the distal side of the M12, by looking at motoneuron positioning. The mean height of the SNa position is not significantly different (WT: 69.62 ± 0.82, cdc42^{V12} OE 68.85 ± 0.93) (**Fig. 5.7A, B**). We found that interestingly, the decision-making for guidance is disrupted and the exit site of the SNa becomes more variable without proper filopodial anchoring (**Fig 5.7B**; F-test; $p = 0.0089$). Next, we measured the defasciculation point of MN5/8 from MN22-24. For this, we traced the length of the axon from the point the MN5/8 turn posterior to their target to the edge of M12. Since defasciculation events happen at the distal edge of M12, we reasoned the filopodia activity on the non-NMJ side may be contributing to the defasciculation events. We found that normal defasciculation happens 2.35±0.17 μm away from the edge of M12 (**Fig. 5.7C**). In contrast, we found that this distance is increased to 3.50±0.26 μm in cdc42^{V12} OE embryos (**Fig. 5.7C**). These data suggest that disruption of muscle filopodia activity results in variation of SNa exit site and spatially delayed defasciculation of MN5/8 from MN22-24.

If the defasciculation site on M12 acts as an anchoring point from which the SNa neurons begin their search for their partners, the loss of filopodia activity in this site may also affect targeting events. To test this idea, we looked at the length of MN24 axon terminal which targets the most distal muscle in SNa path to see if the axon terminal stopped at the appropriate innervation site (**Fig. 5.7D**). In embryonic stages, we found the axon terminal of MN24 is more elongated when filopodia are absent from M12 (**Fig. 5.7E**). To characterize the development of synapses in the other muscles, we investigated the synaptic structures on muscle 24 in late-second/early-third instar larval stage. Interestingly we found that in cdc42^{V12} OE larvae, there are more synapses (Dlg-positive densities colocalized with MN marker) compared with control larvae (**Fig. 5.7F**). Altogether, our experiments with cdc42^{V12} suggest that M12 filopodia are necessary for proper synaptogenesis and decision making for axons, which also affect synaptic development in M24.

5.4 DISCUSSION

In this study, we investigated the morphology and spatial organization of muscle-derived filopodia and their roles in guiding motor axons and establishing synaptic connections during neuromuscular circuit development in *Drosophila melanogaster*. While prior studies have highlighted the contribution of muscle filopodia to synaptic site selection (Johansen et al., 1989; Ritzenthaler et al., 2000), our work reveals that filopodial activity is spatially compartmentalized on the muscle surface and that this compartmentalization extends beyond synaptogenesis to influence earlier guidance decisions.

Despite the anatomical simplicity of *Drosophila* muscles, our data suggest that subcellular specialization at the membrane level plays a critical role in both synaptogenesis and earlier guidance decisions. This underscores the capacity of individual muscle fibers to exert fine-grained control over circuit assembly.

We identified two such domains on muscle 12 (M12): an anterior domain corresponding to the canonical NMJ site of MN12/ISNb innervation, and a posterior domain contacted by the

SNa/MN5/8 branch during axon guidance. Both regions displayed filopodial activity, yet they were associated with distinct outcomes—synapse formation versus guidance modulation. Morphometric analysis revealed that filopodia from both compartments were similar in size and number; however, the frequency of interactions with motor axons differed significantly, with NMJ filopodia exhibiting nearly three times more contacts (~6.1 vs. ~2.3). This quantitative difference suggests a threshold-based mechanism for synapse formation, whereby a critical number of stable contacts may be required to initiate synaptogenesis. These quantitative differences in interaction number may also reflect differences in the timing of filopodial activity onset across compartments, which we further investigated in the following experiments.

Our observations suggest that filopodia activity in the posterior (non-NMJ) compartment begins earlier than in the anterior NMJ domain. Previous studies have identified two distinct phases of muscle filopodia dynamics at the NMJ: an early, neuron-independent phase (13:00–15:00 h AEL) and a later, neuron-dependent phase (15:00–16:00 h AEL), during which filopodia recruitment is enhanced by presynaptic signaling (Ritzenthaler et al., 2000). This biphasic model implies that initial filopodial projections form autonomously but are later stabilized or expanded in response to neuronal input. Our study focused primarily on morphological and interaction differences during the early, neuron-independent phase. As such, it remains to be determined whether the temporal onset or stabilization of filopodia in the different compartments is regulated by distinct cues, or whether compartmentalization itself evolves dynamically over time.

To further test the functional relevance of these compartments, we overexpressed constitutively active Cdc42 (Cdc42^{V12}) in muscle cells to disrupt filopodia formation. Loss of muscle filopodia resulted in a marked increase in growth cone filopodia from the presynaptic ISNb axon, consistent with a model of reciprocal regulation. Previous work using prospero mutants similarly showed that muscle filopodia retract in the absence of neuronal input (Ritzenthaler et al., 2000). Our findings complement this model by showing that presynaptic neurons increase exploratory behavior when deprived of muscle-derived cues. We also observed that growth cones often failed to extend filopodia toward M12 in Cdc42^{V12} embryos and instead overshot the target, suggesting that muscle filopodia not only provide recognition signals but also play an active role in arresting and positioning growth cones for terminal branching.

In addition to overshooting, we observed stalling phenotypes in which the growth cone failed to advance toward M12. Together, these observations suggest that muscle filopodia are essential for completing the final step in targeting—bringing the axon to the edge of the muscle membrane where synaptogenesis can begin.

Previous mutant studies report similar phenotypes in which ISNb targeting in the ventral musculature is disrupted (Arzan Zarin & Labrador, 2019; Jeong, 2021; Nose, 2012). These genetic disruptions often result in pathfinding errors or failure to defasciculate, resembling our observed phenotypes upon loss of muscle filopodia. Localization of the implicated genes within the muscle could provide insight into molecular contributors of filopodia activity and how they facilitate accurate targeting events.

Our findings support the idea that muscle filopodia are actively involved in instructive signaling, but they also raise the possibility of bidirectional communication during early targeting. Upon contact, motor neuron filopodia may receive positional or molecular feedback from the muscle surface, influencing cytoskeletal remodeling or pausing behavior. Such feedback could explain the stalling or overshooting phenotypes observed in the absence of muscle filopodia. Whether these contacts elicit local calcium transients, cytoskeletal anchoring, or ligand-receptor clustering in motor axons remains to be tested, but they may represent an early layer of synaptic specificity establishment.

Strikingly, we also observed that disrupting the posterior, non-synaptic filopodia domain altered SNa pathfinding and defasciculation behavior. The axon showed targeting errors after crossing a "filopodia-free" M12, leading to altered synaptic morphology in its eventual target field. This finding implies that non-synaptic filopodia act as a transient spatial checkpoint during the guidance phase, providing cues for axon positioning before a synaptic match is made.

Together, these findings show that muscle-derived filopodia are not uniform in function. Instead, they form distinct spatial domains with separable roles in axon guidance and synapse formation. This membrane-level compartmentalization likely reflects an early layer of synaptic specificity, one that precedes molecular matching events mediated by adhesion molecules or synaptic organizers.

To our knowledge, this is the first demonstration of functional membrane sub-compartmentalization in Drosophila muscle during early neuromuscular development. Similar principles have been observed in other organisms—for example, recent work in C. elegans revealed distinct muscle membrane subdomains marked by differentially localized proteins (Peysson et al., 2024). These findings suggest that spatial compartmentalization may be a conserved strategy for facilitating localized signaling and neuron–target matching during development.

5.5 FIGURES

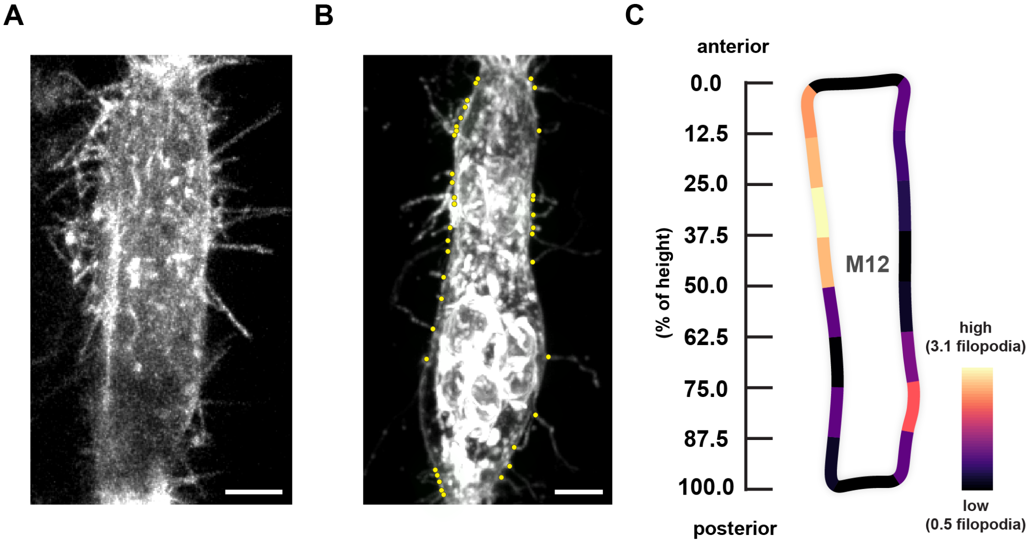

Figure 5.1 Filopodia activity in M12.

(A) Numerous filopodia decorate the surface of M12 in live-dissected embryo visualized with CD4::tdGFP (14:30-15:00 h AEL). **(B)** Filopodia (marked in the bases for quantification) in 13:00-14:00 h old embryo. Immunolabeled against GFP. **(C)** Quantitative heatmap of the filopodia activity of M12 between 13:00-14:30 h AEL. The ruler on the left denotes the position of the bins quantified. The raw data used for generating the heatmap is provided in **Supplementary Table 5.1.** Legend: Maximum color value denotes an average of 3.1 filopodia while the minimum denotes 0.5 filopodia. Scalebars: 5 µm.

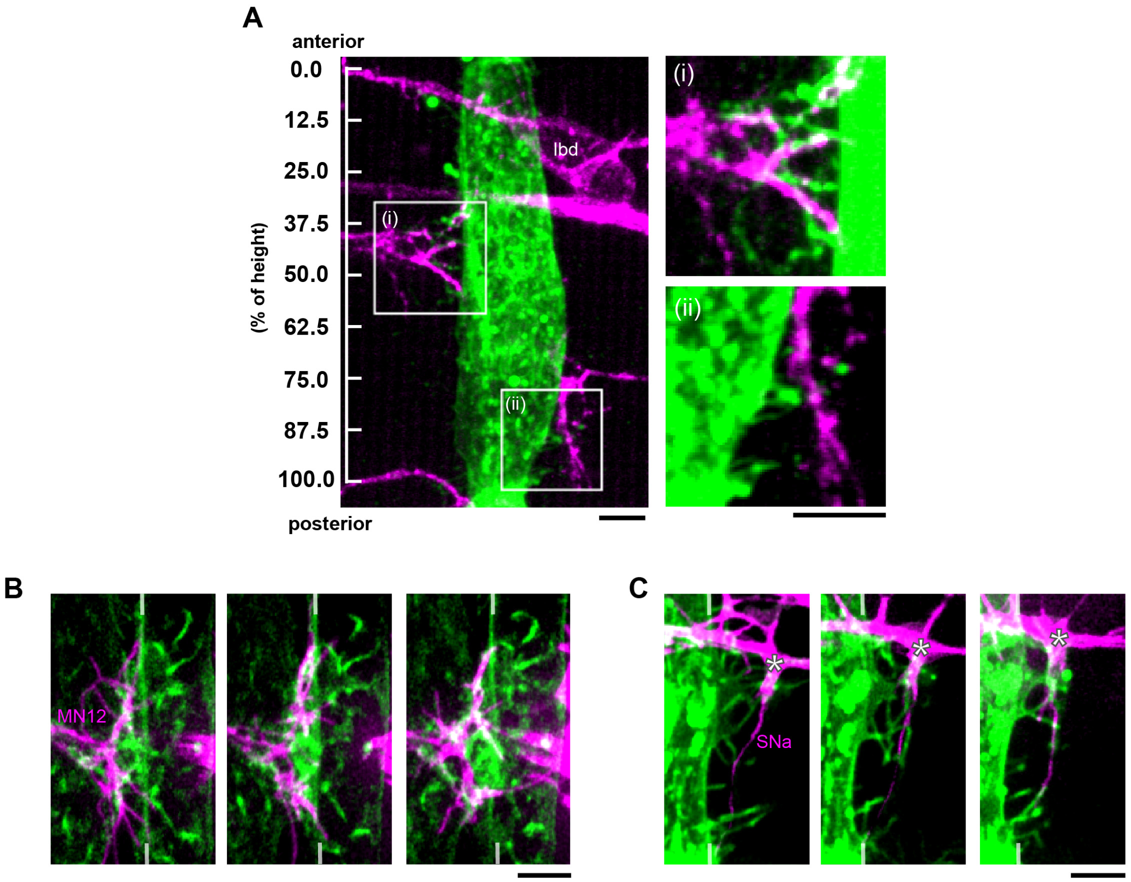

Figure 5.2 Motor neuron placement in relation to M12 filopodia activity.

(A) Filopodia activity coincide with the placements of two motor axon terminals. The box labeled (i) is the ISNb terminal, MN12 interacting with M12 filopodia. The box labeled (ii) marks the SNa terminal reaching posterior for muscles 5/8. The insets show higher contrast magnified views of the filopodial interactions at both regions. **(B)** Filopodia interactions are dynamic, and clustering events observed at the MN12 interaction site with M12. Snapshots from live timelapse movie demonstrate interactions at the MN12 activity site, same as inset (i) in Figure A. **(C)** Filopodia on the muscle are longer reaching the SNa. As SNa is brought closer to the muscle, the muscle filopodia reach the intersection point (defasciculation point; marked with asterisk) of posterior terminal (MN5/8) from the lateral terminal (MN22-24). Snapshots from timelapse interactions at the SNa activity site, same as inset (ii) in Figure A. Scalebars: 5µm

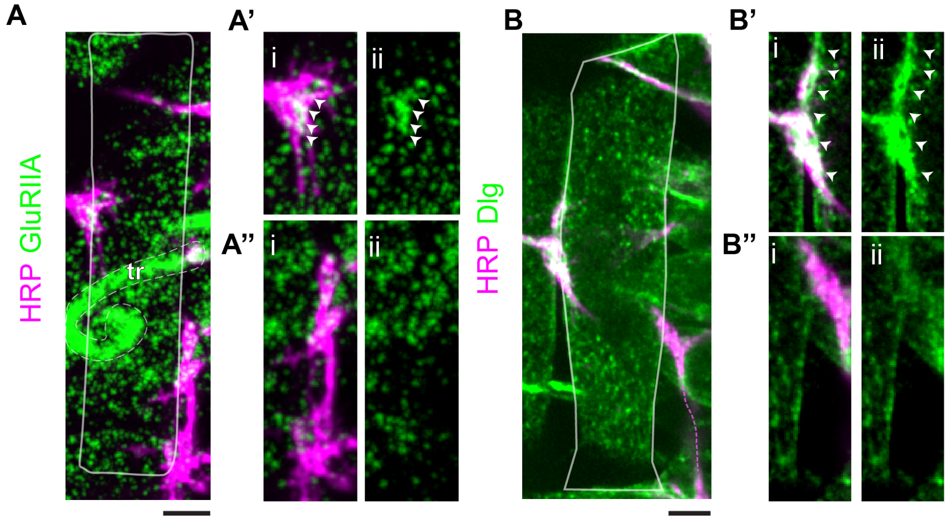

Figure 5.3. Synaptic sites of M12 in late embryo (18:00 h AEL).

Synaptic sites labeled using antibodies against GluRIIA and Dlg. Merged images (A, A'i, A''i, B, B'i, B''i) demonstrate the motor neuron placement, while green panels (A'ii, A''ii, B'ii, B''ii) show the localization of the markers. M12 boundary is outlined (A, B). Scalebars: 5 µm. **(A)** GluRIIA (green) localizes weakly to the synaptic site. Strong tracheal artifact is observed (dashed outline). **(A'-A'')** Magnified sites of motor neuron activity. (A') NMJ accumulation of GluRIIA puncta near MN12 terminal (i, ii; arrowheads). (A") Non-NMJ localization of GluRIIA. The accumulation at the HRP-positive region of the MN5/8 cannot be distinguished from the non-overlapping area (i,ii). **(B)** Dlg (green) localizes strongly to the synaptic site during late embryonic stages. **(B'-B'')** Magnified sites of motor neuron activity. (B') NMJ accumulation of Dlg overlapping with MN12 (i, ii; arrowheads). (B") Non-NMJ localization of Dlg. The HRP-positive region does not make close association with the muscle, and the area of contact does not have clear accumulation of Dlg in the muscle (i,ii).

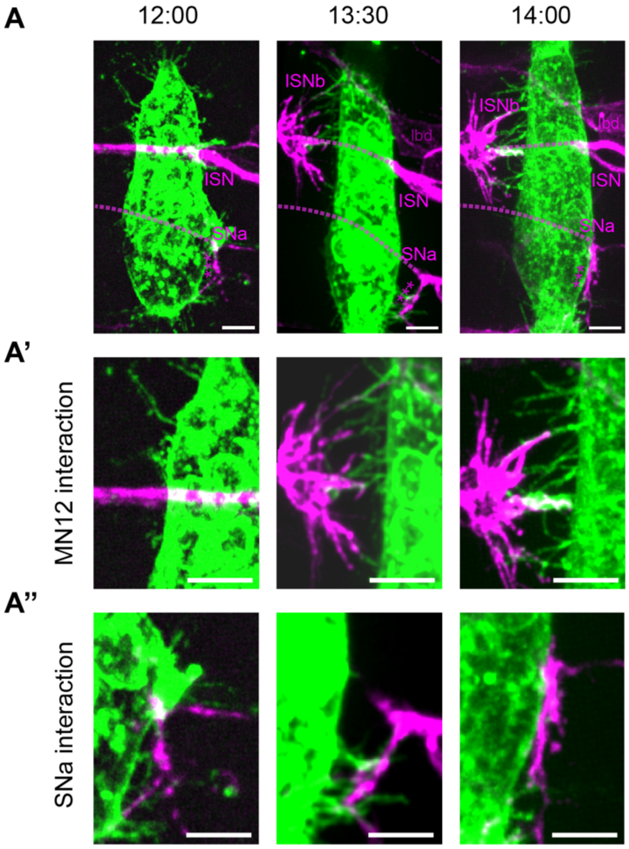

Figure 5.4 Developmental timeline of M12 and filopodia activity

Temporal sequence of filopodia activity from 12:00 to 14:00 h AEL, left to right. **(A)** At 12:00 h AEL, M12 is completing its insertion into epithelia, while ISNb (MN12) has not yet reached the surface of it, SNa is already crossed to the distal side of the muscle. At 13:30 h AEL, both filopodia sites have interactive activity with the motor neurons. At 14:00 h AEL, filopodia activity increase at the MN12 interaction site and the activity ceases at the SNa interaction site. **(A')** Inset of MN12 interaction sites from A. At 12:00 h AEL, filopodia activity is sparse at the MN12 interaction site. ISNb or MN12 is not yet directly interacting with M12. At 13:30 and 14:00 h AEL filopodia activity has increased pre- and post-synaptically. At 14:00 h AEL filopodia cover the edge of the muscle, increasing interactions with the MN12 filopodia. **(A'')** Inset of SNa interaction sites from A. At 12:00 h AEL, filopodia interactions have initiated between M12 and SNa, close to the posterior insertion site of the muscle. At 13:00 h AEL, filopodia activity is substantially increased with SNa posterior branch. At 14:00 h AEL filopodia activity is completely diminished, the SNa branch is closely placed at the edge of M12. There are some residual filopodia that SNa appears to interact with. Scalebars: 5 µm

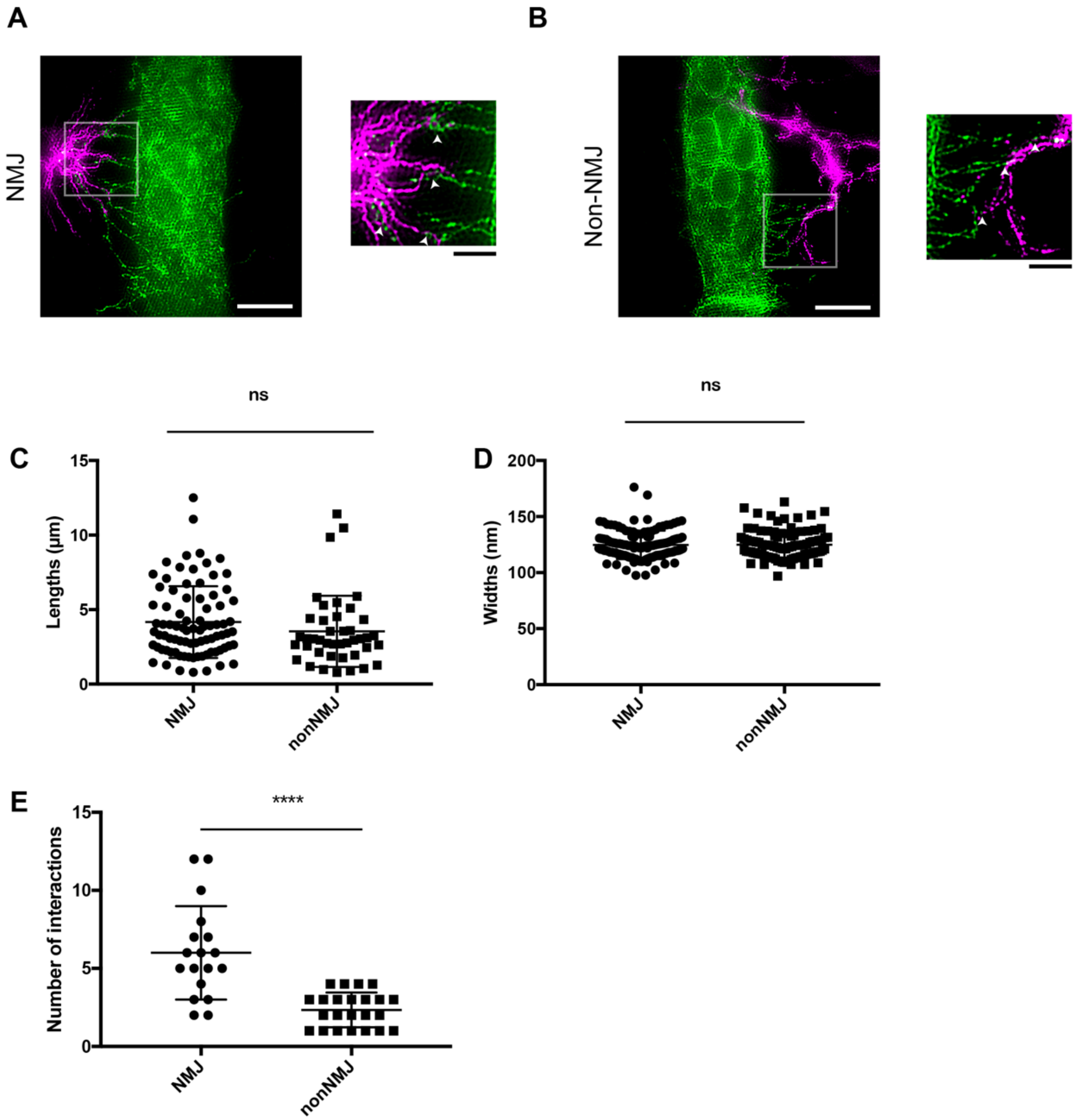

Figure 5.5 Morphological characterization of M12 filopodia at the NMJ and Non-NMJ using 2-color SIM.

(A, B) 2-color SIM images of NMJ and non-NMJ filopodia activity. Insets with arrowheads demonstrate interactions between neuronal and muscle filopodia. Scalebars: 5µm left panels, 2 µm insets. **(C)** Quantification of the lengths of NMJ filopodia (n = 84) and non-NMJ filopodia (n = 42) from the base of the muscle to the tips (in µm). Mann-Whitney test (p = 0.1040). **(D)** Quantification of the widths of NMJ filopodia (n = 127) and non-NMJ filopodia (n = 99) averaged at 70 nm increments (in nm). Mann-Whitney test ($p = 0.9788$). n.s. = not significant. **(E)** Quantification of the number of interactions at the NMJ ($n = 18$) and non-NMJ ($n = 23$). Mann-Whitney test (****: $p < 0.0001$).

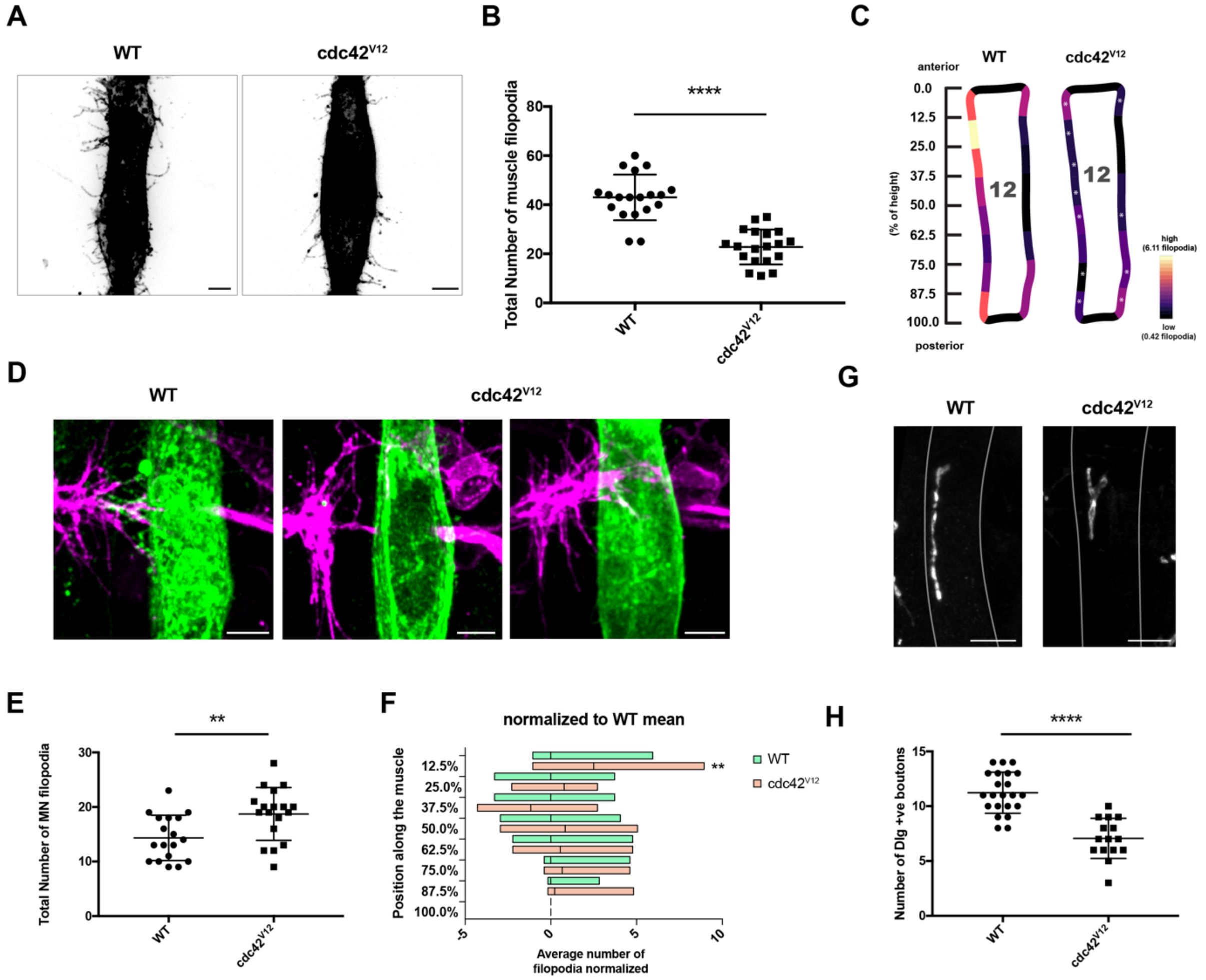

Figure 5.6 Synaptic effects of cdc42^{V12} OE in M12.

(A) Filopodia activity in M12. WT labeled with CD4::tdGFP, Cdc42^{V12} OE labeled with cdc42^{V12}::GFP; both immunostained against GFP. Scalebar: 5 µm **(B)** Total number of filopodia per muscle quantification in WT (n = 19), and cdc42^{V12} OE (n = 19). Unpaired t-test (****: $p<0.0001$). **(C)** M12 filopodia heatmap at 13:30 h AEL. The ruler on the left shows the height of muscle in percentage (%) from anterior to posterior, as in Fig. 5.1. Asterisks (*) in cdc42^{V12} heatmap denote bins with significant differences in filopodia counts. Legend: Maximum color value denotes an average of 6.11 filopodia while the minimum denotes 0.42 filopodia. **(D)** Axon terminal phenotypes in cdc42^{V12} OE. Left panel – WT; middle – stalling phenotype on cdc42^{V12} muscle; right – overshooting phenotype on cdc42^{V12} muscle. Scalebars: 5 µm. **(E)** Total number of MN filopodia reaching to M12 in WT (n = 18) and cdc42^{V12} OE (n = 18). Unpaired t-test (**: p = 0.0061) **(F)** MN filopodia activity in relation to the muscle height normalized to WT mean in 8 bins for WT (n = 18) and cdc42^{V12} OE (n = 18). Mann-Whitney test (**: p = 0.0071). **(G)** Larval M12 NMJ. Muscle outlined in each panel. Synapses are marked with anti-Dlg (gray). Scalebar: 20 µm. **(H)** Quantification of Dlg-positive boutons in WT (n = 22) and cdc42^{V12} (n = 15) at M12 NMJ. Unpaired t-test (****: p < 0.0001).

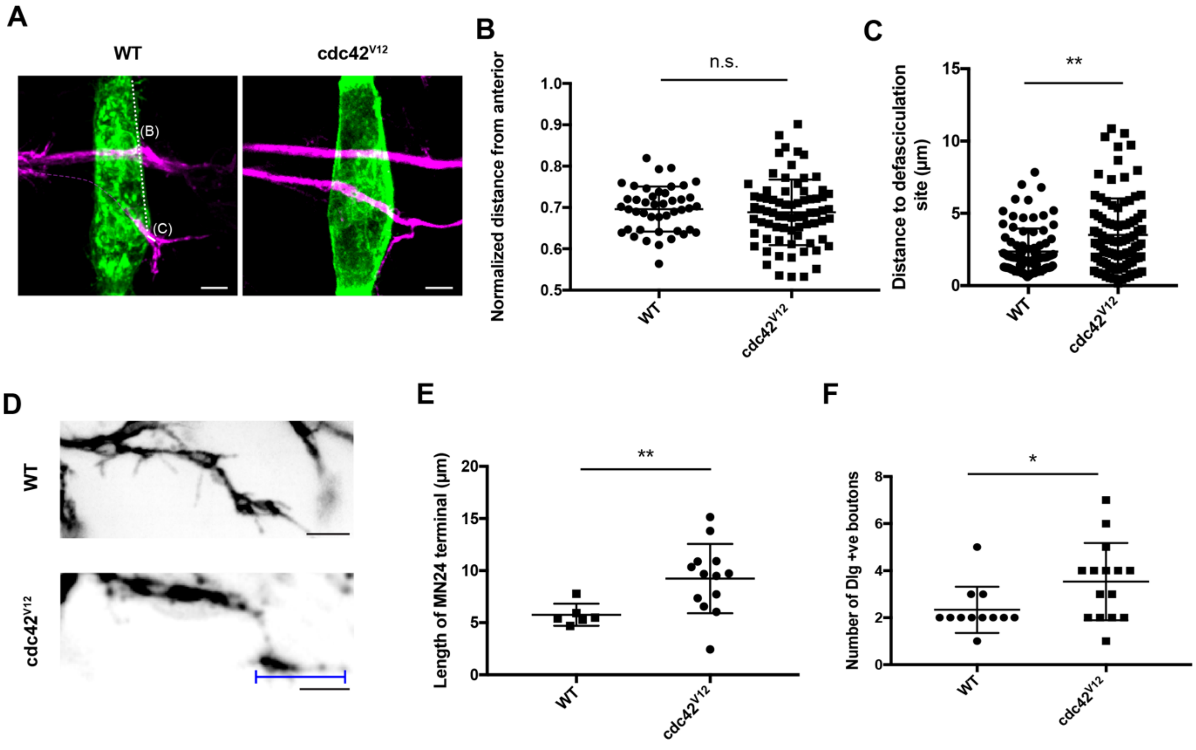

Figure 5.7 Non-synaptic effects of cdc42^{V12} OE.

(A) M12 (anti-GFP; green) z-projection shows the positioning of the SNa axon labeled with anti-HRP (magenta) in WT and cdc42^{V12} OE embryos. [Dotted line (B): the measured SNa exit site from the distal side of M12. Solid line (C): the measured distance of MN22-24 defasciculation from MN5/8.] Scalebars: 5 µm. **(B)** Quantification of SNa exit from the distal side of M12 normalized to the height of the muscle. WT (n = 44); cdc42^{V12} OE (n = 73). Unpaired t-test with Welch's correction (p = 0.5327). n.s. = not significant. **(C)** Quantification of the distance of MN22-24 defasciculation from MN5/8 measured from the distal edge of M12 in µm. WT (n = 86); cdc42^{V12} OE (n = 92). Mann-Whitney test (**: p = 0.0013). **(D)** MN24 targeting in WT and cdc42^{V12} OE in embryo. The blue line demonstrates the axon terminal that was measured for quantification in (E). Scalebars: 5 µm. **(E)** Quantification of length of embryonic MN24 terminal in µm. WT (n = 6); cdc42^{V12} OE (n = 13). Unpaired t-test with Welch's correction (*: p = 0.0036).

(F) Quantification of Dlg-positive boutons in WT (n = 12) and cdc42^{V12} OE (n = 15) at M24 NMJ. Mann-Whitney test (*: p = 0.0336).

5.6 TABLE

Supplementary Table 5.1 Average filopodia number in M12 between 13:00-15:00 h AEL (n= 9)

Bin (%)	Proximal edge	Distal edge
0.0-12.5	2.7	1.3
12.5-25.0	2.8	1.2
25.0-37.5	3.1	1.0
37.5-50.0	2.9	0.5
50.0-62.5	1.3	0.8
62.5-75.0	0.6	1.4
75.0-87.5	1.3	2.3
87.5-100	0.8	1.2

5.7 SUPPLEMENTARY FIGURE

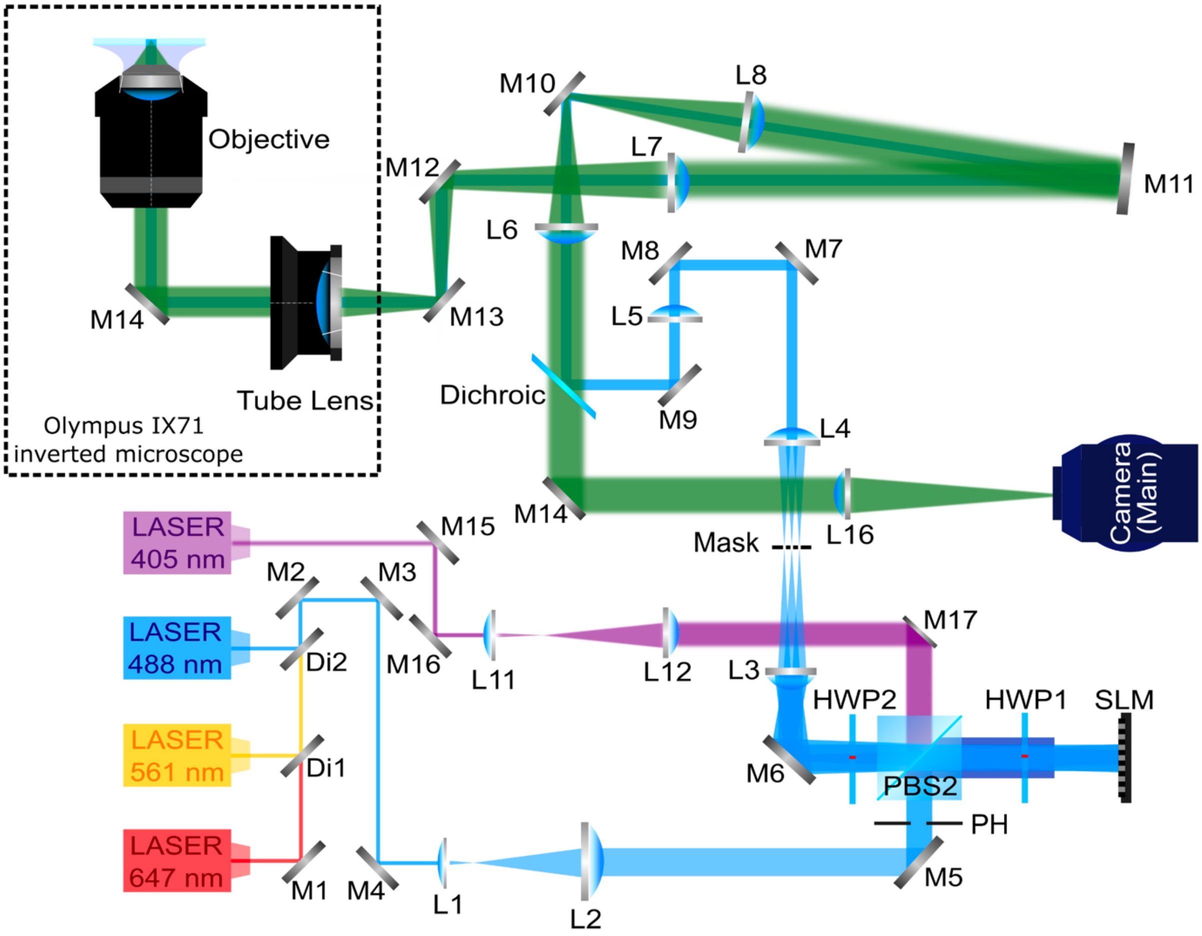

Supplementary Figure 5.1 Experimental setup of multicolor-SIM.

HWP: half-wave plate. PBS: polarized beam splitter. PH: pinhole. M1-M4: flat mirror. L1-L11: lens. f1 = 50 mm, f2 = 400 mm, f3 = 400 mm, f4 = 125 mm, f5 = 125 mm, f6=100 mm, f7=250 mm, f8=250 mm, f9=300 mm, f10=50 mm, f11=200 mm. The blue represents the illumination path (488nm/561nm/647nm), and the green path is the detection path.

5.8 METHODS

Fly stocks

Fly stocks were maintained at 25ºC for experiments. Stocks used: Tey^{5053A}-Gal4 (M12 driver; BDSC: 2702), Gycbeta100B-Gal4 (M12 driver with activity in other muscles; BDSC: 48480), bi-LexA (neuron driver; BDSC: 52430), used to drive UAS-Fascin::GFP (gifted by Tina Tootle, U Iowa), UAS-Rac^{V12}::GFP, UAS-Rac^{N17}::GFP, UAS-Cdc42^{V12}::GFP, UAS-CD4::tdGFP, UAS-CD4::tdTomato, LexAop2-CD4::tdGFP expressions. Embryos with FP expression were selected for immunostaining experiments.

Embryo and larval preparation

Embryos were staged overnight to stage 16 (13:00 h AEL), based on gut morphology, and aged further 30-60 minutes at 25ºC for 13:30-14:00 h AEL. The younger stage 14-15 embryos were collected based on gut morphology at 22-23ºC, to slow development overnight. The embryos were filleted into PBS solution on a glass slide and directly imaged for live movies or fixed with EM grade 4% paraformaldehyde (PFA) for 5 minutes as previously described for immunostaining preparation (Inal et al., 2021).

Embryos for late-stage characterization between 17:00-19:00 h AEL were raised at 25ºC and selected based on gut morphology. Since embryos at this stage develop cuticles and do not adhere to glass slides, we used a quick UV-cured glue (Bondic ®, Amazon) on a plastic slide, which allowed controlled spread of the glue. Briefly, embryos were aligned on double-sided tape in a dissection pool, and prior to adding PBS for dissection, the glue was spread as a thin layer to hold the embryos. Then PBS was added, and 1-2 embryos were brought out of their vitelline membranes and embedded in the glue. Using UV light, the glue was cured for 30-60 seconds. With a dissection needle a small incision was created on the dorsal face of the embryo at its center. With small strokes, additional small cuts were introduced in the anterior direction, and the same was repeated for the posterior direction. The body wall was brought to the glue on each side and the internal organs such as trachea and guts were carefully removed prior to fixation with 4% PFA for 5 minutes.

Larva were collected 2 days following 1st instar hatching then they were immobilized on ice for 20 minutes to allow for pinning. Using standard dissection procedures, larvae were dissected in cold PBS and fixed with 4% PFA for 5-15 minutes.

Immunostaining

Standard immunolabeling procedures was used, as described in **Inal et al., 2021**. Briefly, following fixation, the sample was permeabilized with 0.1% Triton-X100 in PBS (TBS) for 3x5 minutes and blocked with 0.1% TBS + 0.06% bovine serum albumin (BSA) (TBSB) for 1 hour at RT. The primary antibodies were incubated overnight at 4º C and secondary antibodies were incubated at room temperature (RT) for 2 hours. For dual-color labeling with anti-HRP, immediately following fixation, samples were incubated with anti-HRP for 2 hours at RT and post-fixed with 4% PFA before continuing with the immunostaining steps. For GluRIIA immunostaining, the samples were fixed using Bouin's at RT for 20 minutes and thoroughly washed with PBS before proceeding to immunostaining step. Antibodies used: monoclonal mouse anti-Dlg (1:50; DSHB:4F3), rabbit anti-GFP (1:200), monoclonal mouse anti-GluRIIA (1:20; DSHB:8B4D2), anti-HRP Cy3 and anti-HRP Cy5 (1:100), goat anti-rabbit IgG AF 647, CF 555, CF 568 (1:200).

Muscle heatmaps

Images were first annotated with the multi-point tool in Fiji. Each point was added to the base of an identifiable thin protrusion from the edge of the muscle. Images with the overlays were then loaded into Adobe Photoshop and an 8 row by 2 column grid was overlaid parallel to the edges of the muscle and the grid was stretched to fit the muscle, standardizing the bin locations in relation to the muscle size. Number of points were counted in each bin and recorded for each image.

The muscles were traced from a representative confocal image in Adobe Illustrator. Next, the sides that were quantified were split into equal sizes and made into individual line objects. Using a custom Python script, “magma” LUT was split into 16 discrete colors and the measurements were binned into each of the respective color map. Using a custom macro in Adobe Illustrator, the colors were applied to each line object for the muscle.

Confocal microscopy

Confocal microscopy images of fixed filleted embryos were captured using an inverted fluorescence microscope (Ti-E, Nikon) with either 40× 0.80 NA water immersion objective or 100× 1.45 NA oil immersion objective (Nikon). The microscope was attached to the Dragonfly Spinning disk confocal unit (CR-DFLY-501, Andor). Three excitation lasers (40 mW 488 nm, 50 mW 561 nm, and 110 mW 642 nm lasers) were coupled to a multimode fiber passing through the Andor Borealis unit. A dichroic mirror (Dragonfly laser dichroic for 405-488-561-640) and three bandpass filters (525/50 nm, 600/50 nm, and 725/40 nm bandpass emission wheel filters) were placed in the imaging path. Images were recorded with an electron-multiplying charge-coupled device camera (iXon, Andor). For live imaging movies were acquired with 100× 1.45 NA oil immersion objective (Nikon). The z-stacks were limited to a maximum 20 planes to minimize phototoxicity during 2-color acquisition. For imaging NMJ, the embryos were filleted normally in a glass slide and mounted with cold PBS. The non-NMJ sample was dissected and imaged in an open-top No. 1.5 glass-bottom dish in PBS (Delta TTM Culture Dish, Bioptechs).

2-color SIM imaging

2-color SIM images of fixed filleted embryos were captured using a custom-built system attached to Olympus IX71 inverted microscope with a Prior Proscan XY Stage with a 60× 1.50 NA oil immersion TIRF objective (Olympus) (**Fig. S5.1**). The system is equipped with four excitation lasers: 405-nm, 488-nm, 561-nm, and 647-nm lasers (OBIS, Coherent). The illumination lasers are reflected by a polarizing beam splitter (PBS) (10FC16PB.3, Newport) to the sample without reflecting from the Spatial light modulator (SLM, Forth Dimension QXGA-3DM) that displays binary grating patterns. A dichroic mirror (Di01-R405/488/532/635-25x36, Semrock), a quad-band bandpass filter, (FF01-446/523/600/677-25, Semrock BrightLine) and a notch filter (NF03-405/488/561/635E-25, Semrock StopLine® quad-notch filter) were placed before the camera. Images were recorded with an sCMOS camera (Sona 4BV6U, Andor). The total magnification of the system is 180x with a final effective pixel size of 36.1 nm.

The data for 2 color-SIM was acquired sequentially by imaging each channel (561 and 647) with patterned illumination. For 2D-linear SIM, 3 equally distributed phases (0º, 120º, 240º) with 3 imaging angles (0º, 60º, 120º) are acquired for covering the isotropic space, requiring a total of 9 raw image frames for one channel to reconstruct a single color 2D SIM image. Multiple planes were acquired at 0.2-0.3 µm step size in each channel. The reconstruction of SIM is done with an open-source ImageJ plugin *fairSIM* (Müller et al., 2016).

Length and width measurements

The lengths of filopodia were measured from the tip to the edge of the muscle, using the polyline tool with Fiji. The widths of the filopodia were measured with a custom Javascript macro in Fiji. Measurements were taken at 70 nm (~2 pixels) increments perpendicular to the filopodia growth for the entire length and averaged. The widths were calculated by generating an intensity plot and finding its full width at half maximum (FWHM) after fitting into a Gaussian distribution. The measurements that were due to crossing of filopodia which would result in >300 nm as width calculation were removed as well as those <70 nm, due to potential imaging artifacts (Picas et al., 2024). Single line (10-pixel average) measurements in the center of the filopodia, using manual measuring approach also led to similar findings about the widths.

Quantification

Interactions: A spatial overlap between two filopodia of at least the average calculated widths for filopodia (124.7-124.98 nm; see text) was used to determine if there were any interactions. Only one interaction per filopodia was considered. If there were multiple sites of interactions between the same pair of filopodia, this was not measured.

SNa exit site: The position of the exit site from the anterior (A) was normalized to the given muscle's height (h): A / (A+H). The reported values are between 0-1, with 0 representing the exit site at the muscle insertion site at the anterior region and 1 representing the exit site at the posterior insertion site.

MN24 terminal length: The length was measured after the dip of the axon from M23 to M24, up to the distalmost region of the muscle where HRP signal was detected.

Synapses: The number of HRP/Dlg-positive boutons were scored as individual synapses on the edge of M24 or M12 where synapses normally form.

Statistical analysis

Prism 7.0a was used for statistical analysis and graphs (GraphPad, Inc). Shapiro-Wilk test was applied to each sample to test for normality. If both samples passed the normality test, an unpaired t-test was used; otherwise, Mann-Whitney test was used. Welch's correction was applied upon F-test results for those datasets that has different variation. All values are reported as mean±SEM.

5.9 REFERENCES

Broadie, K., & Bate, M. (1993). Innervation directs receptor synthesis and localization in Drosophila embryo synaptogenesis. *Nature*, *361*(6410), 350–353. https://doi.org/10.1038/361350a0

Chiba, A. (1999). Early Development of the Drosophila Neuromuscular Junction: A Model for Studying Neuronal Networks in Development. *International Review of Neurobiology*, *43*, 1–24. https://doi.org/10.1016/S0074-7742(08)60538-3

Fiala, J. C., Feinberg, M., Popov, V., & Harris, K. M. (1998). Synaptogenesis Via Dendritic Filopodia in Developing Hippocampal Area CA1. *The Journal of Neuroscience*, *18*(21), 8900–8911. https://doi.org/10.1523/JNEUROSCI.18-21-08900.1998

Halpern, M., Chiba, A., Johansen, J., & Keshishian, H. (1991). Growth cone behavior underlying the development of stereotypic synaptic connections in Drosophila embryos. *The Journal of Neuroscience*, *11*(10), 3227–3238. https://doi.org/10.1523/JNEUROSCI.11-10-03227.1991

Hoang, B., & Chiba, A. (2001). Single-Cell Analysis of Drosophila Larval Neuromuscular Synapses. *Developmental Biology*, *229*(1), 55–70. https://doi.org/10.1006/dbio.2000.9983

Inal, M. A., Bui, K. C., Marar, A., Li, S., Kner, P., & Kamiyama, D. (2021). Imaging of In Vitro and In Vivo Neurons in *Drosophila* Using Stochastic Optical Reconstruction Microscopy. *Current Protocols*, *1*(7), e203. https://doi.org/10.1002/cpz1.203

Kaufmann, N., Wills, Z. P., & Van Vactor, D. (1998). Drosophila Rac1 controls motor axon guidance. *Development*, *125*(3), 453–461. https://doi.org/10.1242/dev.125.3.453

Kohsaka, H., & Nose, A. (2009). Target recognition at the tips of postsynaptic filopodia: Accumulation and function of Capricious. *Development*, *136*(7), 1127–1135. https://doi.org/10.1242/dev.027920

Krueger, N. X., Van Vactor, D., Wan, H. I., Gelbart, W. M., Goodman, C. S., & Saito, H. (1996). The Transmembrane Tyrosine Phosphatase DLAR Controls Motor Axon Guidance in Drosophila. *Cell*, *84*(4), 611–622. https://doi.org/10.1016/S0092-8674(00)81036-3

Marrus, S. B., Portman, S. L., Allen, M. J., Moffat, K. G., & DiAntonio, A. (2004). Differential Localization of Glutamate Receptor Subunits at the *Drosophila* Neuromuscular Junction. *The Journal of Neuroscience*, *24*(6), 1406–1415. https://doi.org/10.1523/JNEUROSCI.1575-03.2004

Misgeld, T., Burgess, R. W., Lewis, R. M., Cunningham, J. M., Lichtman, J. W., & Sanes, J. R. (2002). Roles of Neurotransmitter in Synapse Formation. *Neuron*, *36*(4), 635–648. https://doi.org/10.1016/S0896-6273(02)01020-6

Müller, M., Mönkemöller, V., Hennig, S., Hübner, W., & Huser, T. (2016). Open-source image reconstruction of super-resolution structured illumination microscopy data in ImageJ. *Nature Communications*, *7*(1), 10980. https://doi.org/10.1038/ncomms10980

Picas, L., André-Arpin, C., Comunale, F., Bousquet, H., Tsai, F.-C., Rico, F., Maiuri, P., Pernier, J., Bodin, S., Nicot, A.-S., Laporte, J., Bassereau, P., Goud, B., Gauthier-Rouvière, C., & Miserey, S. (2024). BIN1 regulates actin-membrane interactions during IRSp53-dependent filopodia formation. *Communications Biology*, *7*(1), 549. https://doi.org/10.1038/s42003-024-06168-8

Ritzenthaler, S., Suzuki, E., & Chiba, A. (2000). Postsynaptic filopodia in muscle cells interact with innervating motoneuron axons. *Nature Neuroscience*, *3*, 1012–1017. https://doi.org/10.1038/79833

The MICrONS Consortium, Bae, J. A., Baptiste, M., Baptiste, M. R., Bishop, C. A., Bodor, A. L., Brittain, D., Brooks, V., Buchanan, J., Bumbarger, D. J., Castro, M. A., Celii, B., Cobos, E., Collman, F., Da Costa, N. M., Danskin, B., Dorkenwald, S., Elabbady, L., Fahey, P. G., … Zhang, C. (2025). Functional connectomics spanning multiple areas of mouse visual cortex. *Nature*, *640*(8058), 435–447. https://doi.org/10.1038/s41586-025-08790-w

Uhm, C.-S., Neuhuber, B., Lowe, B., Crocker, V., & Daniels, M. P. (2001). Synapse-Forming Axons and Recombinant Agrin Induce Microprocess Formation on Myotubes. *The Journal of Neuroscience*, *21*(24), 9678–9689. https://doi.org/10.1523/JNEUROSCI.21-24-09678.2001

CHAPTER 6

CONCLUSION AND FUTURE DIRECTIONS

6.1 SUMMARY OF DISSERTATION

Protocols for visualization of neural circuit development

In Chapter 2 of this work, we have described a protocol for retrograde single-cell labeling of motor neurons, which can also be applicable to individual muscles via lipophilic dyes (**Figure 2.3A**). First, we demonstrated by applying the dye at the neuromuscular junctions, the dye travels to the soma, achieving dense membrane labeling in neuronal processes (e.g. dendrites) (**Figure 2.3** and **2.4**). Second, we utilized two color labeling approach to drop the dyes into aCC (anterior corner cell) and RP3 (raw prawn) terminals, to study interactions or tiling of different dendritic arbors (**Figure 2.3C**). Lastly, taking advantage of high labeling densities in the dendritic membranes, we demonstrated a phenotypic analysis approach to study development of postsynaptic structures in the CNS by looking at mutants, such as *dscam1*$^{-/-}$ (**Figure 2.4).** This technique allows us to measure many morphological parameters such as neurite total length and number, and neurite branch pattern and shape.

In Chapter 3 of this work, we developed protocols for *in vivo* imaging of motor neurons and *in vitro* imaging of cultured primary neurons with STORM which uses photo-switching properties of organic dyes to localize single molecules for super-resolution reconstruction. This technique can reach lateral resolutions of 20 nm and axial resolutions up to 50 nm. Thus, the fine structures like filopodia which are very small (<200 nm in width) are optimal for anatomical studies using this approach. We have demonstrated that with our approach, we can visualize the cytoskeletal architecture of the neuron using tubulin-specific antibodies (**Figure 3.7A**) as well as the neurites extending from primary cultured neurons using a variety of neuronal membrane labeling approaches (genetic and immunofluorescence) (**Figure 3.7B-D**). Next, we applied the labeling and imaging approach for visualizing presynaptic filopodia at the RP5 (or MN12) terminal (**Figure 3.8A**). Since biological structures typically occupy a 3-dimensional space at the cell-level, we also applied 3D STORM to investigate the aCC/pCC motor neurons extending from the CNS (**Figure 3.8B**). For furthering our understanding of synaptogenesis, we proposed to study the neuromuscular junction development. In *Drosophila* NMJ, partner recognition and contact happen through tight filopodia interactions that are unresolved due to their fine structures. Finally, we proposed the use of multicolor STORM (using compatible dyes) to visualize the details of filopodia interactions (**Figure 3.5**).

Binary expression systems for visualization of NMJs

In Chapter 4, we curated a set of muscle-specific *Gal4* drivers and orthologous motor neuron-specific *LexA* drivers for studying NMJ development and used live-visualization to uncover different interaction types in different muscles. In the past, studies of NMJ development in embryonic stages have been carried out in muscle 6 (M6) due to easy accessibility for dye labeling and electrophysiology and in muscle 12 (M12) due to a readily available *Gal4* driver which provides single muscle resolution accessibility for imaging. Thus, we expanded the available muscles for studying NMJ development by reporting new *Gal4* drivers. First, we characterized 6 lines that allow visualization of ventral, ventral + dorsal, or lateral (external) musculature in the spatial groups (**Figure 4.1** and **4.2A-D**). We also identified a driver which has broad activity in spatial groups with subsets of muscle activity (**Figure 4.2E**). Second, we characterized 3 drivers that have stochastic expression patterns (**Figure 4.3** and **Supplementary Figure 4.2A-B**). With the new set of *Gal4* drivers (**Supplementary Table 4.1**), all 30 muscles' NMJs can be visualized at single cell resolution (**Figure 4.3**). Third, we identified 3 motor neuron *LexA* drivers which have activity early onset or late onset (**Figure 4.4**) to combine with the *Gal4*s to study NMJ interactions. Lastly, we used a *Gal4-LexA* pair to study the NMJ interactions and dynamics of membrane protrusions in muscles 12 (VL1) and 14.1 (VO2) before and during contraction events (**Figures 4.5** and **4.6**). Membrane protrusions forming sheet-like structure in the M12 have been demonstrated before (Ritzenthaler et al., 2000). Our study uncovered that it first develops as two small sheets prior to contraction (**Figure 4.5A'**), and the gap between the two sheets fill resulting in a single sheet-like structure the motor neuron associates with (**Figure 4.6A'**). Interestingly, we also found that the muscle protrusions are not synchronized in their appearance suggesting different cellular mechanisms for NMJ formation. When the sheet-like structure begins to develop in M12, M14.1 is in a clustering phase of its filopodia (which is an earlier event that M12 also participates in). In later development, we made another contrast between M12 and M14.1. While a single sheet is observable at M12 during contractile phase of the muscle, there are ridges found on the edge of M14.1 (**Figure 4.6A'** versus **4.6A''**). Altogether using binary expression systems, we proposed dynamics of membrane protrusions of different muscles are different, challenging the notion of perfect temporal synchronization of interactions at the NMJ for synaptogenesis.

Compartmentalization of filopodia activity and their roles in circuit development

In Chapter 5, we revealed that muscle filopodia have multiple functions in distinct locations on the muscle. Previous studies have shown that filopodia on the muscle cluster at the synaptic site interacting with the presynaptic motor neuron contributing to target recognition.

Given filopodia activity is found throughout the surface of the muscle from early on, other filopodia that extend opposite of the synaptic site may also have hotspots of activity, contributing to axon guidance, pathfinding and/or synaptogenesis. Thus, we asked whether there are other hotspots of filopodia activity and if so, are these activities essential for proper neuromuscular circuit formation? First, we characterized the filopodia activity on the M12 surface during the time in which neuromuscular contacts are forming and found that there are two sites of increased filopodia activity which corresponded to interaction sites with motor neurons (**Figure 5.1-2**). By evaluating the sequence of interactions, we found that the novel hotspot, which we call the non-NMJ filopodia, participates in motor neuron interactions before NMJ filopodia do (**Figure 5.4**). Interestingly, we found filopodia interactions at the non-NMJ site do not result in synaptogenesis (**Figure 5.3**), suggesting that the interactions have another function. We reasoned that if the protrusions are structurally distinct, different types of protrusions –like intercellular bridges, or cytonemes– could be contributing to the different outcomes for filopodia interactions. For this, we characterized their lengths and widths using structural illumination microscopy and found that morphologically they had no differences (**Figure 5.5C-D**). However, we found different levels of interactions, which suggests a difference at the level of signaling may determine their role during synaptogenesis (**Figure 5.5E**).

To gain more insights into the roles of filopodia during circuit formation, we knocked down filopodia activity in M12 (**Figure 5.6A-C**) and we investigated sites of interaction between M12 and the motor neurons. At the synaptic site, we found that MN12 steering and targeting was affected, resulting in smaller synapses (**5.6D-H**). Interestingly, at the non-synaptic site, the loss of filopodia activity resulted in delayed defasciculation of SNa while also affecting targeting at muscle 24 and synaptogenesis (**Figure 5.7**). Altogether, we propose that (1) the number of interactions over a specific threshold dictates the decision to become a synaptic site and (2) filopodia activity in muscles coordinate axon targeting, axon guidance, timing of defasciculation and synapse formation, supporting the notion filopodia have multiple functions **(Supplementary Figure 6.1)**.

6.2 FUTURE DIRECTIONS

Dye labeling technique

While our demonstration of the dye labeling technique was restricted to motor neuron morphologies with lipophilic dyes, this technique can be utilized for visualizing muscles at the NMJ. Filopodia on the muscle are extend as long as 40 μm (Ritzenthaler et al., 2000). Thus, it is conceivable that while interacting with motor neurons is a method of cellular communication they participate in, it is equally likely they communicate with other muscles through their filopodia. For instance, during development of syncytium, occasionally muscles are coupled to nearby muscles (Bate, 1990). In decoupling, some studies suggest membrane protrusions are found at the sites of decoupling (Carayon et al., 2020). Using multicolor dye labeling approach, we can precisely visualize filopodial communication between muscles as the motor circuit develops.

Actin-based membrane protrusions come in different flavors. Some can be specialized with distinct functions and morphologies. For instance, specialized structures known as tunneling nanotubes, or intercellular bridges, connect the cells to each other for direct exchange of materials including RNA, protein and organelles (Cordero Cervantes & Zurzolo, 2021). Muscle cells in *Drosophila* contain large numbers of filopodia throughout embryogenesis, yet whether any of these filopodia structures are more specialized like tunneling nanotubes remains unclear. One circumstantial piece of evidence at the molecular level is that Cdc42 activity inhibits formation of tunneling nanotubes while promoting the formation of filopodia (Delage et al., 2016). If muscle protrusions are primarily consistent of tunneling nanotubes, then our observations with Cdc42^{V12} may be a consequence of losing tunneling nanotube functions. However, since molecular mechanisms of membrane protrusions largely overlap (Belian et al., 2023), additional studies are required. A direct assessment as to whether muscles have tunneling nanotubes during the filopodial phases, would be to inject the muscles with cytoplasmic dyes, to trace possible connections that form directly between neuron-muscle contacts.

2-color STORM imaging of in vivo and in vitro neurons

We have proposed the use of dual-color STORM to investigate the cellular morphologies of the filopodia interaction sites at the NMJ. Subsequently, we have conducted some preliminary experiments and optimized an approach to visualizing the NMJ morphologies using STORM (**Supplementary Figure 6.2**). Interestingly, we observe unique structures in subsets of filopodia that may differentiate them into two distinct populations (see discussion below on Morphological characteristics of filopodia). Since we identified an independent filopodia site that does not lead to synaptogenesis, studying the morphology of these filopodia at super-resolution using 2-color STORM in a broader time frame of its activity (from ~12:00-14:00 h AEL) may provide a better understanding of the morphological dynamics underlying its cellular mechanisms involved in guiding the SNa axon.

Additionally, how the cytoskeletal changes guide filopodia dynamics in neuromuscular synaptogenesis remains unclear, partially due to lack of reliable *in vivo* tools to visualize actin filaments or microtubules without the background signals from other cells (as in *in vivo* immunofluorescence), or without affecting the dynamics of endogenous proteins (as in overexpressing cytoskeleton associated proteins). An *in vitro* alternative such as neuron-muscle cocultures in conjuction with immunofluorescence can be a solution to address dynamic organization of cytoskeleton underlying filopodial interaction during guidance and target recognition will be important for addressing bidirectional communication in relation to cytoskeletal remodeling. For such experiment 3-color STORM or multicolor DNA-PAINT (another modality of single molecule localization microscopy) approach will be beneficial to for visualizing opposing membranes as well as the cytoskeleton of each cell at super-resolution (Acosta et al., 2025).

Hotspots of filopodia activity

We identified distinct hot spots of filopodia activity in M12. Using live imaging, we also detected that muscle 14.1 also has at least one hotspot of filopodia activity at the motor neuron interaction site; however, with a different appearance compared to M12 at the time of observation. The differences in the morphological structures between 12 and 14.1 may result from the differences in their innervation patterns (14.1 receives two innervations while 12 receives three) resulting in differences in timing of innervation. Additional areas of interest would be to reveal timing of filopodia activity based on the spatial positioning of muscles. For instance, muscle 14.1 is external to M12, thus their activity may be differentially regulated by where they are placed on the body wall. Furthermore, in line with this idea, the sizes and orientations of muscles may contribute to the differences in filopodia based activity. This aspect has been demonstrated to contribute to timing in muscle fusion (Bate, 1990; Beckett & Baylies, 2007), therefore it is conceivable that morphological properties of the muscle also contribute to development of synapse. To address these questions, filopodia activity maps can be generated using the muscle-specific *Gal4* set to image individual muscles.

At subcellular level, muscles can be highly compartmentalized with distinct combinations of proteins in each domain. To understand the molecular machinery involved in distinct compartmentalization and role division of filopodia, testing for a diffusion barrier would be essential (Rolls et al., 2007). If the proteins are regulated in their specific compartments with a barrier, then spatial proteomics or transcriptomics would be an important step to identify candidate proteins involved in compartmentalized roles of muscles.

Functions of sheet-like structures on the muscle

Through live imaging, we observed that a sheet-like structure develops and remains at the neuromuscular junction after muscle contractions have begun. The roles of these membrane sheets remain unknown. However, one possibility could be that they act as a reservoir of synaptic proteins by a simple diffusion mechanism (Thalmeier et al., 2016), which are then enriched at the contact site when the sheet is retracted in later stages. Similar observations have been made in the presynaptic axon terminal: the planar regions of growth cone structures swell during NMJ development and contribute to the formation of presynaptic sites by production and transportation of synaptic components (Yoshihara et al., 1997). Since synaptic proteins such as Fas2 have been demonstrably enriched in the sheet-like structure in the muscle (Kohsaka et al., 2007), it is likely the formation of the sheet may result in efficient diffusion of proteins to establish the synaptic site shortly after synaptic interaction begins. Importantly, a genetic or pharmacological tool will be necessary to manipulate this sheet formation to assess the localization of synaptic proteins.

Morphological characteristics of filopodia

We found there to be no difference between the filopodia widths or lengths during early contact formation at the NMJ (13:30 h AEL). However, these groups of filopodia may be representing a naïve population of filopodia that extend independent of neuron activity. To illustrate, there are two different phases of filopodia activity: the first one, the “initial phase”, lasts from 13:00-15:00 h AEL and emerge independently of the motor neuron, and the second one, the “neuron-dependent phase,” lasts from 15-16 h AEL resulting in production of new and/or stabilization of existing filopodia (Ritzenthaler et al., 2000). It is possible the filopodia that emerge during “neuron-dependent phase” may carry the information necessary for synaptogenesis at the interaction site, thus as a distinct group of filopodia, they may have different morphological characteristics. The previous studies have not specifically focused on compartment specific filopodia activity, therefore, it is essential to test whether filopodia activity on the SNa interacting site is also independent of neural signaling, by using *prospero* mutant flies in which muscle development is normal and axon outgrowth is severely delayed. Subsequently, using super-resolution microscopy, filopodia in the neuron-dependent phase should be evaluated for their morphology. Our preliminary experiments using 2-color STORM imaging suggests that there may be two distinct groups of filopodia at the M12 NMJ based on morphology (**Supplementary Figure 6.2**). Here, we observed fusiform morphology on filopodia in contact with the motor neuron with diameters of 0.3-0.7 μm. These may represent early structures of synapses as those found in rat hippocampal neurons where filopodia (0.1-1 μm in diameter) with fusiform structures contain post-synaptic densities (Fiala et al., 1998). Further studies investigating localization of post-synaptic proteins or glutamate receptors in the filopodia may shed a light into where synaptic structures are found during early synaptic activities.

Filopodial interactions for synaptogenesis

We proposed that by overcoming a threshold of filopodia interactions, the non-synaptic sites may be able to form ectopic synapses. Studies in understanding mechanisms of connectivity in target selection have demonstrated ectopic synaptic sites on M12-SNa interaction site. For instance, when muscle 5 is absent in Ubx mutants, when Fas2 (Neural Cell Adhesion Molecule ortholog) is overexpressed in muscles, and when Connectin, another cell adhesion molecule specific to SNa and its target muscles, is ectopically expressed in M12, ectopic synapses on SNa interaction site of M12 have been observed (Cash et al., 1992; Lin & Goodman, 1994; Nose et al., 1997). Each case supporting a model of increased adhesion between the two contacts, the relevance of filopodia interaction have not been investigated in these contexts. Therefore, the number of interactions in these conditions can be assessed for testing whether muscles in these conditions form increased filopodia interactions.

Cdc42 limitations and alternative tool for filopodia manipulation

We investigated the effects of filopodia loss using Cdc42^{V12} overexpression in muscles. While the filopodia activity is certainly diminished from the muscle, Cdc42 is a key regulator of many cell processes, one of which affects development of muscle itself (Luo et al., 1994). In our experiment of single muscle targeting, we did not observe deformations of the muscle structure. However, it is possible that other aspects of cell signaling dependent on Cdc42 activity may be affected in these embryos. For instance, Cdc42 activity is involved in docking vesicles to the membrane for exocytosis (Etienne-Manneville, 2004). Therefore, we cannot eliminate the possibility of Cdc42 mediated vesicle secretion resulting in non-filopodia related phenotypes for guidance and targeting. Thus, alternative means for targeting filopodia activity will be necessary by directly and locally inducing actin polymerization or depolymerization. One approach for knocking down filopodia activity could be through a probe called DeAct, which consists of the domain of gelsolin that sequesters actin monomers, inducing depolymerization of actin filaments in the cell (Harterink et al., 2017). Such probe can be applied transiently through UAS/Gal4 system in conjunction with Gal80 (for repressing Gal4 activity), to spatiotemporally control its expression in the muscle during axon guidance/targeting. Since muscle structure highly depends on actin cytoskeleton, improving the subcellular localization of this tool into muscle filopodia would be essential. This could be achieved by combining DeAct with a filopodia specific protein such as Fascin, to localize it at sites of filopodia formation, preventing local actin assembly, and filopodia formation and promote disassembly of filopodia in the developing embryos. As a complementary experiment, approaches for inducing filopodia formation will also be needed to gain a more complete understanding of filopodia's role in neuromuscular circuit development.

6.3 SUPPLEMENTARY FIGURES

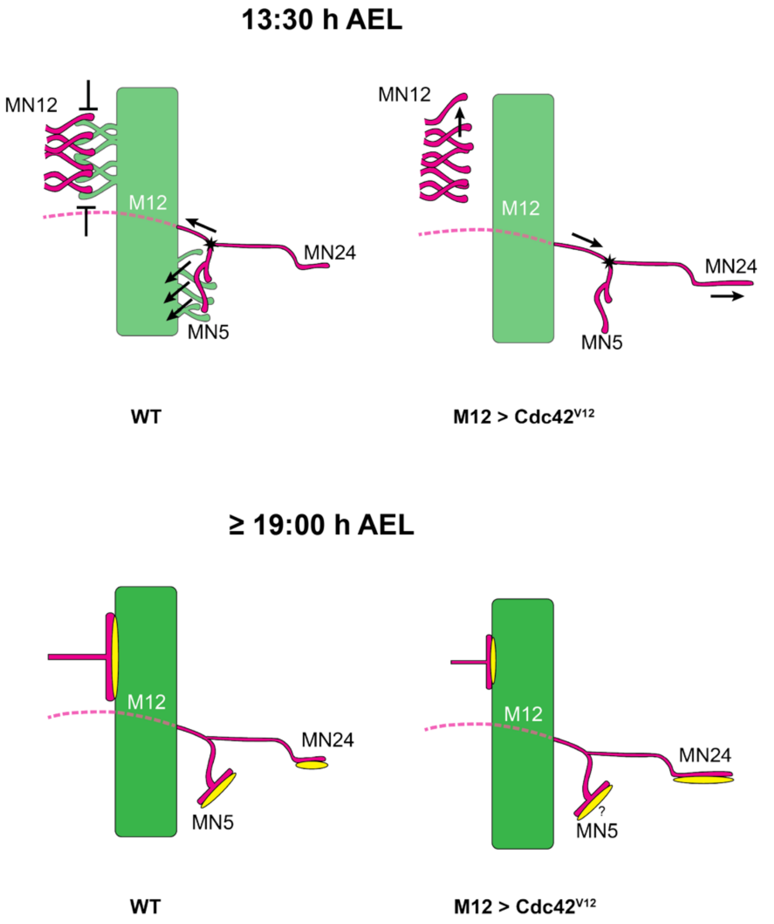

Supplementary Figure 6.1 Working model of muscle filopodia function in neuromuscular junction development.

(Top panel) In WT embryos at 13:30 h AEL, the anterior M12 filopodia site makes more interactions with MN12 than the posterior filopodia site makes with MN5. The M12 filopodia at the anterior site restricts the domain of MN12 interaction (T-bars). The posterior filopodia interactions refine (arrows) the positioning of the defasciculation choice point of SNa between MN5 and MN24 (star) placing it close to the edge of M12. In filopodia knockdown embryos (M12 > Cdc42^{V12}), at the anterior site, the MN12 interaction domain is disrupted, with MN12 increasing filopodia activity and increasing the filopodia that reach the anterior-most domain of the muscle.

At the posterior site, the defasciculation choice point is pushed/placed further from the edge of M12. Additionally, the MN24 axon overshoots its typical innervation site. **(Bottom panel)** In WT embryos after 19:00 h AEL and 2nd instar larva, a synapse (yellow oval) forms at the anterior interaction site with MN12 interaction, whereas the interaction of MN5 with M12 in the posterior site is pruned, and an appropriate synapse is made with M5, as MN24 innervates its partner muscle 24 making a proper synapse. When filopodia activity is knocked down (M12 > Cdc42^{V12}), MN12 makes a smaller synapse, whereas the overshot MN24 makes a larger synapse with its partner muscle. (The consequences on the MN5 innervation remains to be characterized.)

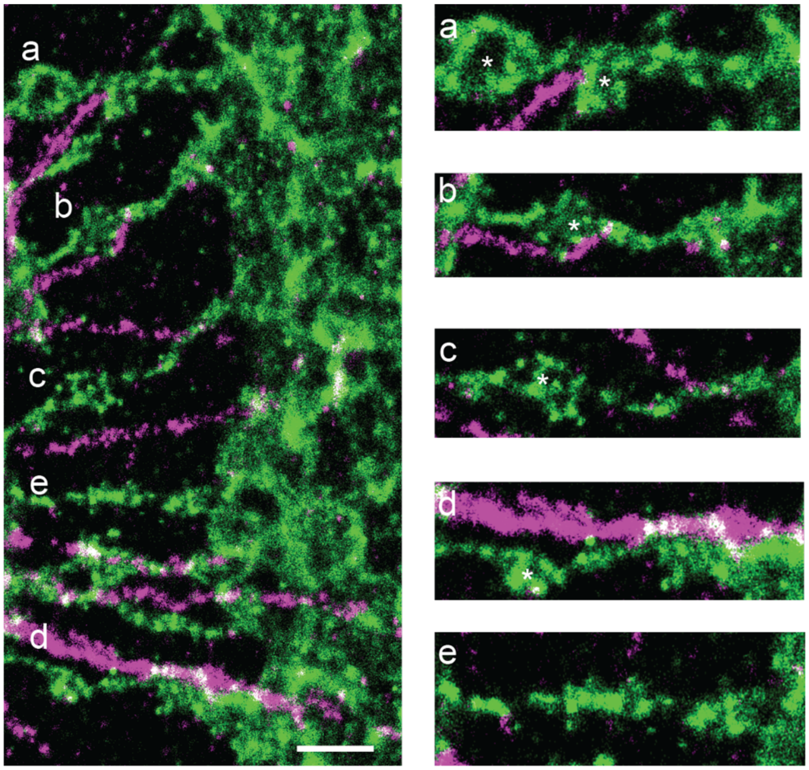

Supplementary Figure 6.2 2-color STORM image of M12 NMJ

M12 membrane is labeled with anti-GFP CF647 (green) and motor neuron membrane is labeled with anti-HRP CF568 (magenta). Filopodia interactions between neuron and muscle demonstrating fusiform structure marked with asterisk in the single-filopodia ROIs (a-e). **(a-d)** contain the fusiform structure nearby the interaction site with the motor neuron filopodia. (a) contains two distinct structures, one of which appears to come from another filopodia that intersects it. **(e)** does not have motor neuron filopodia interacting with it and lacks the fusiform structure. Scalebar: 1 μm

6.4 REFERENCES

Acosta, N., Gong, R., Su, Y., Frederick, J., Medina, K. I., Li, W. S., Mohammadian, K., Almassalha, L., Wang, G., & Backman, V. (2025). Three-color single-molecule localization microscopy in chromatin. *Light: Science & Applications*, *14*(1), 123. https://doi.org/10.1038/s41377-025-01786-1

Arzan Zarin, A., & Labrador, J.-P. (2019). Motor axon guidance in Drosophila. *Seminars in Cell & Developmental Biology*, *85*, 36–47. https://doi.org/10.1016/j.semcdb.2017.11.013

Belian, S., Korenkova, O., & Zurzolo, C. (2023). Actin-based protrusions at a glance. *Journal of Cell Science*, *136*(22), jcs261156. https://doi.org/10.1242/jcs.261156

Carayon, A., Bataillé, L., Lebreton, G., Dubois, L., Pelletier, A., Carrier, Y., Wystrach, A., Vincent, A., & Frendo, J.-L. (2020). Intrinsic control of muscle attachment sites matching. *eLife*, *9*, e57547. https://doi.org/10.7554/eLife.57547

Cash, S., Chiba, A., & Keshishian, H. (1992). Alternate neuromuscular target selection following the loss of single muscle fibers in Drosophila. *The Journal of Neuroscience*, *12*(6), 2051–2064. https://doi.org/10.1523/JNEUROSCI.12-06-02051.1992

Cordero Cervantes, D., & Zurzolo, C. (2021). Peering into tunneling nanotubes—The path forward. *The EMBO Journal*, *40*(8), e105789. https://doi.org/10.15252/embj.2020105789

Delage, E., Cervantes, D. C., Pénard, E., Schmitt, C., Syan, S., Disanza, A., Scita, G., & Zurzolo, C. (2016). Differential identity of Filopodia and Tunneling Nanotubes revealed by the opposite functions of actin regulatory complexes. *Scientific Reports*, *6*(1), 39632. https://doi.org/10.1038/srep39632

Etienne-Manneville, S. (2004). Cdc42—The centre of polarity. *Journal of Cell Science*, *117*(8), 1291–1300. https://doi.org/10.1242/jcs.01115

Harterink, M., Da Silva, M. E., Will, L., Turan, J., Ibrahim, A., Lang, A. E., Van Battum, E. Y., Pasterkamp, R. J., Kapitein, L. C., Kudryashov, D., Barres, B. A., Hoogenraad, C. C., & Zuchero, J. B. (2017). DeActs: Genetically encoded tools for perturbing the actin cytoskeleton in single cells. *Nature Methods*, *14*(5), 479–482. https://doi.org/10.1038/nmeth.4257

Jeong, S. (2021). Molecular Mechanisms Underlying Motor Axon Guidance in Drosophila. *Molecules and Cells*, *44*(8), 549–556. https://doi.org/10.14348/molcells.2021.0129

Jiang, N., Kim, H.-J., Chozinski, T. J., Azpurua, J. E., Eaton, B. A., Vaughan, J. C., & Parrish, J. Z. (2018). Superresolution imaging of *Drosophila* tissues using expansion microscopy. *Molecular Biology of the Cell*, *29*(12), 1413–1421. https://doi.org/10.1091/mbc.E17-10-0583

Kohsaka, H., & Nose, A. (2009). Target recognition at the tips of postsynaptic filopodia: Accumulation and function of Capricious. *Development*, *136*(7), 1127–1135. https://doi.org/10.1242/dev.027920

Lin, D. M., & Goodman, C. S. (1994). Ectopic and increased expression of fasciclin II alters motoneuron growth cone guidance. *Neuron*, *13*(3), 507–523. https://doi.org/10.1016/0896-6273(94)90022-1

Luo, L., Liao, Y. J., Jan, L. Y., & Jan, Y. N. (1994). Distinct morphogenetic functions of similar small GTPases: Drosophila Drac1 is involved in axonal outgrowth and myoblast fusion. *Genes & Development*, *8*(15), 1787–1802. https://doi.org/10.1101/gad.8.15.1787

Madhavan, R., Zhao, X. T., Reynolds, A. B., & Peng, H. B. (2006). Involvement of p120 catenin in myopodial assembly and nerve–muscle synapse formation. *Journal of Neurobiology*, *66*(13), 1511–1527. https://doi.org/10.1002/neu.20320

Nose, A. (2012). Generation of neuromuscular specificity in Drosophila: Novel mechanisms revealed by new technologies. *Frontiers in Molecular Neuroscience*, *5*. https://doi.org/10.3389/fnmol.2012.00062

Nose, A., Umeda, T., & Takeichi, M. (1997). Neuromuscular target recognition by a homophilic interaction of connectin cell adhesion molecules in Drosophila. *Development (Cambridge, England)*, *124*(8), 1433–1441. https://doi.org/10.1242/dev.124.8.1433

Ritzenthaler, S., Suzuki, E., & Chiba, A. (2000). Postsynaptic filopodia in muscle cells interact with innervating motoneuron axons. *Nature Neuroscience*, *3*(10), 1012–1017. https://doi.org/10.1038/79833

Rolls, M. M., Satoh, D., Clyne, P. J., Henner, A. L., Uemura, T., & Doe, C. Q. (2007). Polarity and intracellular compartmentalization of Drosophila neurons. *Neural Development*, *2*(1), 7. https://doi.org/10.1186/1749-8104-2-7

Shim, S.-H., Xia, C., Zhong, G., Babcock, H. P., Vaughan, J. C., Huang, B., Wang, X., Xu, C., Bi, G.-Q., & Zhuang, X. (2012). Super-resolution fluorescence imaging of organelles in live cells with photoswitchable membrane probes. *Proceedings of the National Academy of Sciences*, *109*(35), 13978–13983. https://doi.org/10.1073/pnas.1201882109

Suzuki, E., Rose, D., & Chiba, A. (2000). The ultrastructural interactions of identified pre- and postsynaptic cells during synaptic target recognition inDrosophila embryos. *Journal of Neurobiology*, *42*(4), 448–459. https://doi.org/10.1002/(SICI)1097-4695(200003)42:4<448::AID-NEU6>3.0.CO;2-H

Thalmeier, D., Halatek, J., & Frey, E. (2016). Geometry-induced protein pattern formation. *Proceedings of the National Academy of Sciences*, *113*(3), 548–553. https://doi.org/10.1073/pnas.1515191113